Experimental and *ab-initio* studies of solute-defect interactions in Fe and FeCr alloy

By
M. VAIRAVEL
PHYS 02 2013 04 003

Indira Gandhi Centre for Atomic Research, Kalpakkam

A thesis submitted to the

Board of Studies in Physical Sciences

In partial fulfillment of requirements

for the Degree of

DOCTOR OF PHILOSOPHY

of

HOMI BHABHA NATIONAL INSTITUTE

July, 2018

Homi Bhabha National Institute[1]

Recommendations of the Viva Voce Committee

As members of the Viva Voce Committee, we certify that we have read the dissertation prepared by M. Vairavel entitled "**Experimental and *ab-initio* studies of solute-defect interactions in Fe and FeCr alloy**" and recommend that it may be accepted as fulfilling the thesis requirement for the award of Degree of Doctor of Philosophy.

Chairman - Dr. B. K. Panigrahi **Date:** 11/1/2019

Guide / Convener - Dr. B. Sundaravel B. Sundaravel **Date:** 11/01/2019

Examiner – Dr. S.V.S. Nageswara Rao S.V.S. Nageswarao **Date:** 11/01/2019.

Member 1- Dr. R. Rajaraman **Date:** 11/01/19

Member 2- Dr. Arup Dasgupta **Date:** 11.01.19

Final approval and acceptance of this thesis is contingent upon the candidate's submission of the final copies of the thesis to HBNI.

I hereby certify that I have read this thesis prepared under my direction and recommend that it may be accepted as fulfilling the thesis requirement.

Date: 11/01/2019

Place: Kalpakkam

B. Sundaravel

Guide

STATEMENT BY AUTHOR

This dissertation has been submitted in partial fulfillment of requirements for an advanced degree at Homi Bhabha National Institute (HBNI) and is deposited in the Library to be made available to borrowers under rules of the HBNI.

Brief quotations from this dissertation are allowable without special permission, provided that accurate acknowledgement of source is made. Requests for permission for extended quotation from or reproduction of this manuscript in whole or in part may be granted by the Competent Authority of HBNI when in his or her judgment the proposed use of the material is in the interests of scholarship. In all other instances, however, permission must be obtained from the author.

M. Vairavel

DECLARATION

I, hereby declare that the investigation presented in the thesis has been carried out by me. The work is original and has not been submitted earlier as a whole or in part for a degree / diploma at this or any other Institution / University.

M. Vairavel

List of Publications arising from the thesis

Journal

1. “Lattice location of O^{18} in ion implanted Fe crystals by Rutherford backscattering spectrometry, channeling and nuclear reaction analysis’, **Vairavel Mathayan**, Sundaravel Balakrishnan, Binaykumar Panigrahi, Nucl. Instr. Meth. B, 2016, 383, 47-51.

2. “Studies of O^{18} impurity trapping at interstitial dislocation loops in ion implanted Fe (110) by ion channeling and ab initio calculations”, **Vairavel Mathayan**, Saravanan Kothalamuthu, Jaiganesh Gnanasekaran, Sundaravel Balakrishnan, Binaykumar Panigrahi, Nucl. Instr. Meth. B, 2018, 414, 141–145.

3. “Defect structure of oxygen-vacancy clusters in O^{18} and self ion implanted Fe(100) crystal by ion channeling and ab-initio study’, **Vairavel Mathayan**, Saravanan Kothalamuthu, Jaiganesh Gnanasekaran, Lakshmanan Chelladurai, Rajaraman Ramalingam, Sundaravel Balakrishnan, Binaykumar Panigrahi, Amarendra Gangavarapu, Acta Mater., 2018, 143, 198-204.

4. “Studies of Cr and O interactions with dislocation loops in Fe and FeCr alloy by ion channeling and *ab-initio* calculations’, **Vairavel Mathayan**, Saravanan Kothalamuthu, Jaiganesh Gnanasekaran, Lakshmanan Chelladurai, Rajaraman Ramalingam, Sundaravel Balakrishnan, Binaykumar Panigrahi, Amarendra Gangavarapu. (Submitted)

5. “Ab-initio studies of Cr and Mn interactions with di and tri-interstitial defects in bcc Fe”, **Vairavel Mathayan**, Jaiganesh Gnanasekaran, Sundaravel Balakrishnan, Binaykumar Panigrahi. (Submitted)

Conference proceedings

1. Lattice Location of Cr in Cr^+ Ion Implanted BCC Fe(100) by Particle Induced X-ray Emission and Channeling, **M. Vairavel**, K. Saravanan, B. Sundaravel, *AIP Conference proceedings 1942 (2018) 080003*.

Conferences

1. Lattice location of O^{18} in Fe(100) crystal by Rutherford Backscattering Spectrometry, Channeling and Nuclear Reaction Analysis. **M. Vairavel**, B. Sundaravel and B. K. Panigrahi. *International conference on Swift Heavy Ions in Materials Engineering and Characterization held at NIPGR/IUAC, New Delhi, India. October 14-17, 2014*.

2. Lattice Location of Cr in Cr^+ Ion Implanted BCC Fe(100) by Particle Induced X-ray Emission and Channeling, **M. Vairavel**, K. Saravanan, B. Sundaravel, *62nd DAE Solid State Physics Symposium (DAE SSPS-2017) held at Bhabha Atomic Research Centre, Mumbai, India. December 26-30 2017*.

3. Lattice location of O^{18} in O^{18} ion implanted bcc FeCr(100) by ion channeling, **M. Vairavel**, K. Saravanan and B. Sundaravel, *1st Research scholars meet on materials science and engineering on nuclear materials (RSM-MSENM) held at Indira Gandhi Centre for Atomic Research, Kalpakkam, India. May 7-9 2018.*

4. Oxygen interactions with vacancy defects in FeCr alloy by ion channeling and ab-initio study, **Vairavel Mathayan**, Jaiganesh Gnanasekaran, Sundaravel Balakrishnan, Binay Kumar Panigrahi, *Internation Symposium on Solid State Chemistry of Transition Metal Oxides, November 30-decenber 01, 2018 held at Jawaharlal Nehru Centre for Advanced Scientific Research, Bangalore, India.*

5. Experimental and *Ab-initio* Studies of Solute-defect Interactions in Fe and FeCr Alloy, **M. Vairavel**, *63rd DAE Solid State Physics Symposium, December 18-22, 2018, held at Guru Jambheshwar University of Science and Technology, Hisar, Haryana, India.*

M. Vairavel

I dedicate this thesis to my family.

Mother M. Mariyammal, Father I. Mathayan,
Brother M. Dhanapal and M. Valarmathy.

ACKNOWLEDGEMENTS

It is a pleasure to express my sincere gratitude to my PhD guide Dr. B. Sundaravel for his guidance and encouragement.

I would like to extend my sincere thanks to the doctoral committee members Prof. B.K. Panigrahi, Dr. R. Rajaraman and Dr. Arup Dasgupta for their comments and suggestions. I would like to thank Prof. N. V. Chandra Shekar, Dean and Prof. B. V. R. Tata, former Dean, Physical Sciences for their support.

I make a special thanks to Dr. G. Jaiganesh, Dr. Sharat Chandra, Dr. P. Anees, Dr. Manan Dholakia, Mr. P. Jagadeesan, for fruitful discussions on DFT and other simulations.

I thank Dr. K. Saravanan, Dr. S. Amirthapandian, Mr. P. Magudapathy, Dr. Christopher David, Dr. Sachin Kumar Srivastava, Anbu anna, Nataraj, operators (Saravanan, Anand, Ashok) and all the members of accelerator lab for their support in experiments and teaching.

I like to thank Dr. G. Amarendra, Mr. C. Laksmanan, Mr. K.G. Ragavendra, Ms. S. Kalavathi, Dr. Shilpam Sharma, T. Sathyanarayana Annam, and Dr. Edward Prabu for their discussions on experimental techniques.

My sincere thanks to Prof. Smulders, University of Groningen, The Netherlands and Prof. Ulrich Wahl, Instituto Tecnológico e Nuclear, Portugal for their discussions on FLUX ion channeling simulations.

My special thanks to all the members of the Materials Science Group, especially, Mr. Kanmani, Dr. S. Sivakumar, Dr. Awadhesh Mani, Dr. Sandip K. Dhara and Dr. Raghavan, Dr. D. Sornadurai, for their suggestions and encouragement during my stay at IGCAR.

I thank my entire seniors-cum friends. Srinivasan, Karthickeyan, Mahendran, Devidas, Thangam, Raghavendra, Benadict, Sanjay, Balakrishnan, Naveen, Bharath, Santhosh, Abuthahir, Vinod for their encouragement all these years.

I extend my thanks to all my batchmates-cum-friends. Lakshmanan, Radhikesh, Irshad, Nilakantha Meher, Padmalochan Panda, Zaibudeen, Santhosh, Manoj and Madhushmita for their friendship and help.

Acknowledgment would be incomplete without thanking my juniors-cum-friends. Dhilipan, Akshaya Devi, Rajitha, Jegathamani, Jegnaseni Pradhan, Balasaritha, Sinduja, Sivakumar, Raghavendran, Saikumaraan, Thirukumaran, Balasundaram, Balasubramanian, Velraj. Special thanks to all my well wishers and friends in the JRF enclave.

I would like to acknowledge the Department of Atomic Energy for the research fellowship. I extend my gratitude to our director Dr. A. K. Bhadhuri, Dr. M. Saibaba and Dr. Lakshmi Narasimman for their support. I would also like to thank the office staff of MSG, especially Ms. Vidhya and Ms. Kavya for their assistance.

I also like to remember my uncle Mathayan and family members (Sinnathaayee, Palanigounder, Iyyannagounder, Kulanthaipaiyan, Thangammal, Nagammal) for their love, care and support.

Abstract of Ph.D Thesis

The reduced activation ferritic/martensitic steels are proposed structural materials for future nuclear reactors due to their better void swelling resistance over austenitic steels. For these materials, bcc Fe and FeCr alloy are used as model systems in computer simulation as well as ion irradiation experiments. Solute-defect interactions play a crucial role in deciding materials properties. In this regard, present thesis addresses the O interactions with defects in Fe and the influence of Cr on O interaction with defects in FeCr alloy. A combined analysis of ion channeling and positron annihilation experiments along with DFT calculations makes this study possible with complete understanding. Oxygen isotope (O^{18}) ion is implanted around a depth of 280 nm in Fe and FeCr single crystals. The Lattice location of O^{18} is measured using the out-coming α-particle from $O^{18}(p,\alpha)N^{15}$ nuclear reaction and channeling analysis. The dislocation loop density and vacancy concentration are also studied by ion channeling and slow positron Doppler broadening spectroscopy. In O^{18} ion implanted Fe crystal, the O^{18} is found at tetrahedral interstitial site. Similar lattice location of O, comparable to experiment is obtained for O interaction with interstitial dislocation loops by DFT calculations, which implies that O is trapped in interstitial dislocation loops. In another Fe crystal where excess vacancy defects are introduced at O^{18} depth by self-ion implantation, O^{18} is found to be displaced 1.1 Å along <111> from octahedral interstitial site. Upon increasing vacancy concentration by further self-ion implantation, O^{18} shifts to another site which is displaced 0.6 Å along <100> from octahedral interstitial site. DFT calculation predicts similar displacement of O along <111> for ½ <111> vacancy dislocation loops and along <100> for <100> dislocation loops from octahedral interstitial site. Combined analysis show that the O is initially trapped at ½ <111> vacancy dislocation loops and the ½ <111> loops transform to <100> vacancy loops during further self ion implantation. In O^{18} ion implanted Fe15at%Cr single crystal alloy, O^{18} is found to be trapped in vacancy dislocation loops which is in contrast to Fe where O^{18} is trapped in interstitial dislocation loops at the same experimental condition. The Cr segregation is found to suppress the O interaction with interstitial dislocation loop and promote the O interaction with vacancy dislocation loops. These results show that lattice position of impurity depends on its interaction with type of defects as well as their concentration. This thesis gives strong evidence of competing interactions of solutes with defects and its effect on the microstructure.

Table of Contents

List of Figures

List of tables

Chapter 1

Introduction

The structural materials in nuclear reactor are exposed to extreme conditions, high temperature and high radiation of neutron flux, which deforms the structural materials and affects material performance. The vacancy and interstitial defects are produced during irradiation of neutrons in structural materials. These defects migrate at high temperature and form defect clusters (dislocation loops and voids) and result in swelling of structural materials (see Fig. 1.1). Ferritic steel is one of the proposed structural materials for future nuclear reactors owing to the better void swelling resistance. The body centered cubic iron (bcc Fe) and iron-chromium alloys (bcc FeCr) are model systems for ferritic steel. To better understand the defect evolution and effect of solute on the radiation induced microstructure of ferritic steels, solute-defect interactions in bcc Fe and FeCr system have been studied by using experiment as well as theoretical calculations. This is a current topic of interest for many research groups worldwide [1-10].

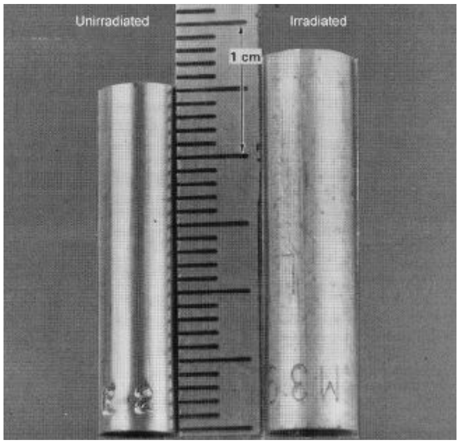

Figure 1.1 Photograph of 20% cold-worked 316 stainless steel rods before (left) and after (right) irradiation at 533°C to a fluence of 1.5×10^{23} neutrons m^{-2} in the EBR-11 reactor [9].

Generally light elements (H, C, N, O and He) occupy interstitial sites and heavy elements (Mn, Cr, Cu etc.) occupy substitutional sites in bcc Fe. The interactions of different solutes present in the structural materials are driving the vacancy and interstitial cluster evolution during irradiation. The presence of C in bcc Fe reduces the mobility of vacancies by forming the V_n-C_m clusters which also reduces the formation of large size V_n-He_m clusters [11]. The formation of Al_mV_n clusters (with m, n ~ 0-4) is predicted in bcc Fe which have strong influence on mechanical properties [12]. The C, He, O and N solutes form clusters with vacancies and other substitutional solutes in bcc Fe and bcc Fe-X (X=Cr, Mn, Cu, Ni) alloys [13]. Among these solutes, oxygen (O) plays a crucial role on the radiation induced microstructure in iron based structural materials [10, 14]. In this regard, understanding the interaction of O with radiation induced defects is important to improve radiation tolerance of iron based structural materials. In this thesis, the interaction of oxygen with interstitial and vacancy defects in bcc Fe and FeCr crystal is studied in detailed manner by experiment as well as density functional theory (DFT) calculations. In this chapter a brief literature review is given on radiation induced defects in Fe and its interactions with solute/impurity atoms.

1.1. Radiation induced defects in iron

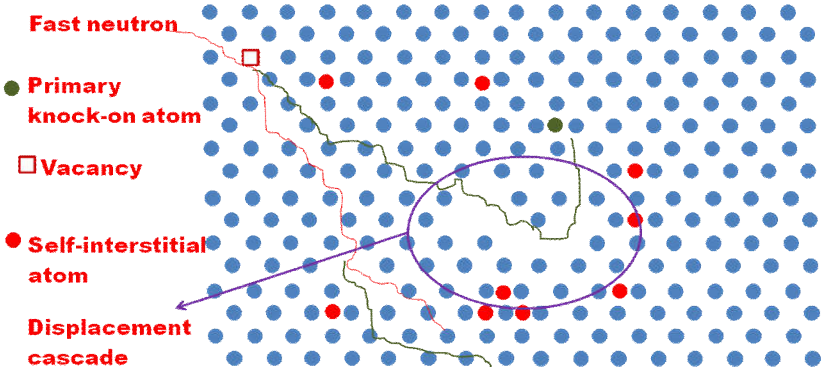

Figure 1.2 Displacement cascade produced by fast neutrons in crystalline materials.

The consequences of radiation in structural materials include change in shape and volume, increased hardness and embrittlement. A firm understanding of radiation effect in materials is essential to design a new radiation resistant materials and for safe operation of existing components. The form of radiation could be neutron, electron, ions and gamma rays. The schematic of damage produced during neutron irradiation is shown in Fig. 1.2 and the time scale for the radiation effects are shown in Table 1.1. When a high energy neutron enters into material, it displaces an atom from its equilibrium lattice position and the displaced atom is called as primary knock-on atom (PKA). If PKA has sufficient energy, it displaces the other lattice atoms (secondary knock-on atoms). In this way high energy neutrons produce displacement cascade where self interstitial atom (SIA) and vacancy (V) defects are present [15]. The PKA stops as an interstitial in the material. This is the primary damage process. The surviving vacancy and SIA defects during primary radiation damage migrate by thermal energy and subsequent effect of these are radiation damage effects which include defect clustering, defect dissociation, impurity defect interactions etc.

Table 1.1 Time-scale for the production of defects in irradiated metals [15].

Time (s)	Event	Results
10^{-18}	Energy transfer from the incident particle	Creation of a PKA
10^{-13}	Displacement of lattice atoms by PKA	Displacement cascade
10^{-11}	Energy dissipation, spontaneous recombination and clustering	Stable Frenkel pairs (SIA and V) and defect clusters
$>10^{-8}$	Defect reactions by thermal migration	SIA and vacancy recombination, clustering, trapping, defect emission

The measure of primary radiation damage is generally described by displacement per atom (dpa) which is defined as,

$$dpa = \frac{N_d}{N_m} \tag{1.1}$$

N_d - Number of displaced atoms in a volume, N_m - Number of lattice atoms in the same volume. The dpa can also be calculated as [15],

$$dpa = \sigma_s \left(\frac{\gamma E_i}{4E_d} \right) \Phi \tag{1.2}$$

where $\gamma = \dfrac{4M_1M_2}{(M_1+M_2)^2}$, E_i-energy of incident particle, E_d-displacement energy of atom in the material, Φ-particle fluence and σ_s-scattering cross section.

Defects produced by ion irradiation in Fe have been studied by many authors [16-20]. Formation of vacancy and interstitial dislocation loops are observed (Fig. 1.3 (a) [16-18]) in irradiated iron (~1 dpa) by transmission electron microscopy (TEM) analysis. In case of super saturation of vacancies, void formation is observed as shown in Fig. 1.3 (b) [19,20].

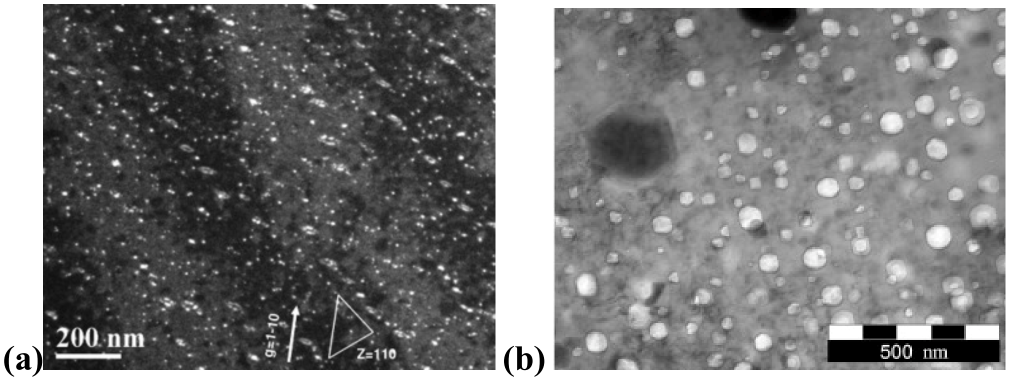

Figure 1.3 (a) Microstructure of ultra-high purity iron irradiated with Fe^+ ions to the dose of 1 dpa at 673 K [18]. (b) A bright field TEM micrograph of an electron-transparent region from an EK-164 cladding specimen irradiated to 87 dpa at a time-averaged temperature of 490 °C [20].

1.2. Structure of radiation induced defects in iron

The formation of interstitial and vacancy clusters are observed as the radiation damage effects in materials. However, characterizing the structure of defects is also important for understanding microstructural evolution of materials under such radiation. DFT calculations, molecular static (MS) and molecular dynamic (MD) simulations have been used to study atomistic structure of small interstitial and vacancy defect clusters in iron. Schematic of various SIA clusters is shown in Fig. 1.4. By considering the structure of SIA defect in bcc Fe, the <110> dumbbell defect is reported to be most stable mono interstitial by DFT calculations [21-24]. In <110> dumbbell configuration, a lattice point is shared by two Fe atoms displaced along <110> direction.

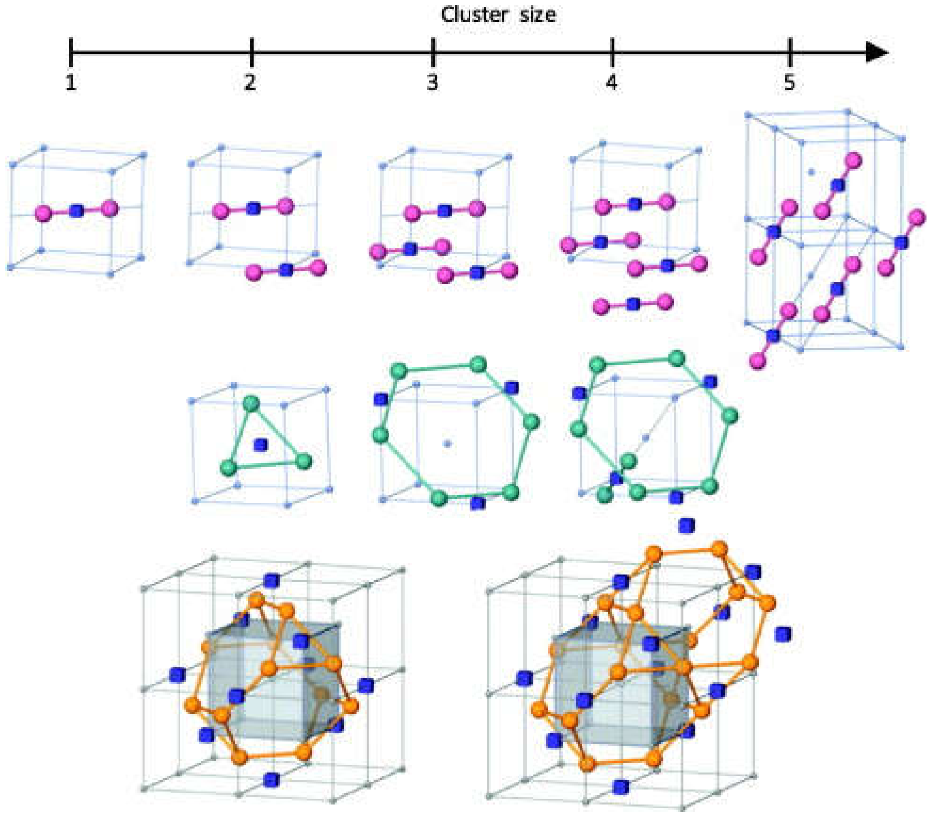

Figure 1.4 Schematic representation of the various families of SIA clusters in bcc iron. Upper panel: parallel dumbbells aligned either in the <110> direction (up to 4 SIAs) or in the <111> direction (5 SIAs or more). Middle panel: ring-like structures (triangle or hexagons). Lower panel: C15-type clusters. The vacancies are represented by dark-blue cubes and the SIA by colored spheres [23].

There are many defect structures proposed for small SIA clusters, (i) parallel dumbbell configurations, which are bundles of <110> dumbbells up to 4 SIA. Above 5 SIA cluster, the <111> parallel dumbbells are found to be stable [21], (ii) planar defect structures, where interstitial atoms are arranged in a triangle/hexagonal fashion in {111} plane [22,23], and (iii) C15 Laves phase structures. These Laves phase structures are $MgCu_2$ (spacegroup-*Fd-3m*) type where interstitial atom occupies Cu sites and half of the Mg sites occupied by vacancies while remaining occupied by Fe atoms [24] (shown in Fig. 1.4). Among them, the parallel dumbbell defect structures are highly mobile. The planar defect structure is found to be unfaulted to <110> parallel configuration during migration [24]. However, DFT calculations predict that the di- and tri-interstitials with planar defect structures are more stable than that of other defect structures and they are regarded as the building blocks for large size clusters [22,23].

In case of small vacancy clusters, various possible structures are proposed as shown in Fig. 1.5. Structures shown in Fig. 1.5 (b), 1.5 (e) and 1.5 (f) are reported to be most stable structures for di-, tri-, tetra-vacancy clusters respectively from DFT calculations [25].

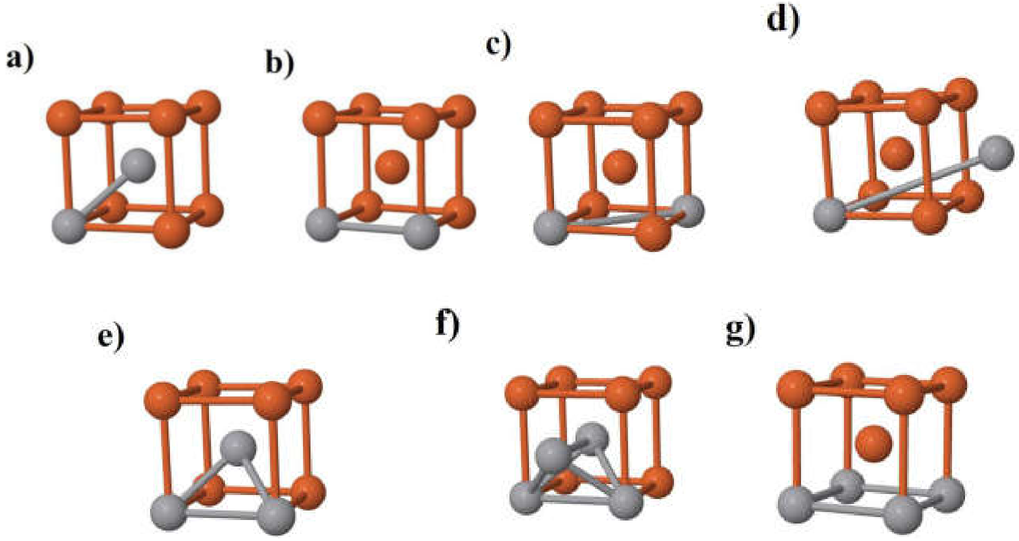

Figure 1.5 Configurations containing two (1NN (1^{st} nearest neighbor) (a), 2NN (b), 3NN (c) and 4NN (b)), three (e) and four ((f) and (g)) vacancies in bcc Fe investigated by *ab initio* calculations. Fe atoms are shown as light brown spheres and vacancies as grey spheres [25].

By considering the defect structure of interstitial/vacancy dislocation loops, Burgers vector *b* = ½ <111> and <100> loops are observed with interstitial/vacancy type. The schematics of vacancy and interstitial type dislocation loops are shown in Fig. 1.6. The schematics of ½ <111> interstitial type dislocation loops are shown in Fig. 1.7. For interstitial type dislocation loops extra layers of atoms are added without disturbing the staking sequence. For ½ <111> interstitial dislocation loop, three layers of atoms within certain radius are added along <111> direction, hence {111} stacking sequence in bcc Fe is 'ABC' along the

⟨111⟩ direction. For the case of <100> loop, two layers of atoms are added hence, the {100} staking along <100> direction is 'AB'. Similarly plane of atoms are removed for the case of vacancy type dislocation loops [26,27]. Depending on implantation dose and annealing conditions, the change in type, size, density and ratio of ½ <111> to <100> structure of loops are reported by TEM analysis. Masters *et al*. reported observation of both ½ <111> and <100> interstitial dislocation loops [28] and English *et al*. [29] reported the formation of vacancy type dislocation loops in heavy ion irradiated iron.

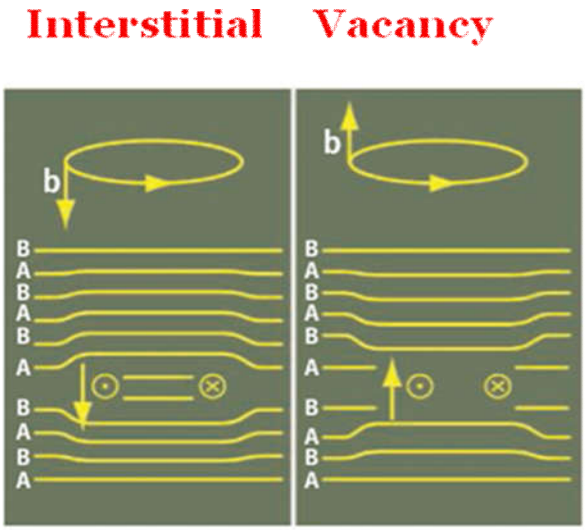

Figure 1.6 Schematics of <100> vacancy (right) and interstitial (left) dislocation loops in iron [26].

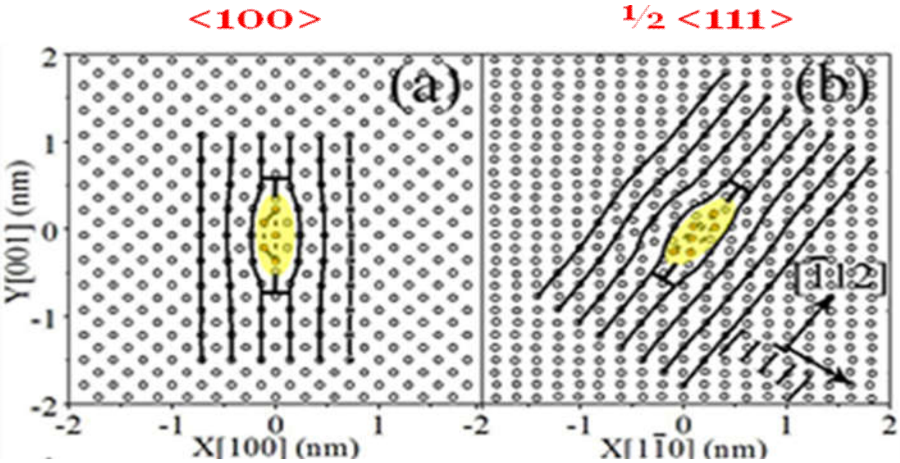

Figure 1.7 Structure of <100> (a) and ½ <111> (b) interstitial type dislocation loops in iron [27].

1.3. Kinetics of radiation induced defects in bcc iron

The defect clusters (voids or dislocation loops) are observed due to irradiation in iron. However, the defect properties like migration and clustering should be clearly understood for materials design. Defect kinetics refers the study of motion of defects and its causes. Defect kinetic studies are reported by resistivity recovery experiments in irradiated iron. In resistivity recovery experiments the irradiated sample recovers its defect-free resistivity as it is annealed with raise in temperature [30]. During isochronal annealing of electron irradiated iron various migration/dissociation mechanisms come into play in the order of increasing activation energies. From resultant resistivity recovery measurements, kinetics of the vacancy and interstitial defect could be studied. Takaki *et al.*, have reported the resistivity recovery experiments in high-purity electron-irradiated iron with irradiation doses in the range ~2×10^{-6} to ~200×10^{-6} dpa [31].

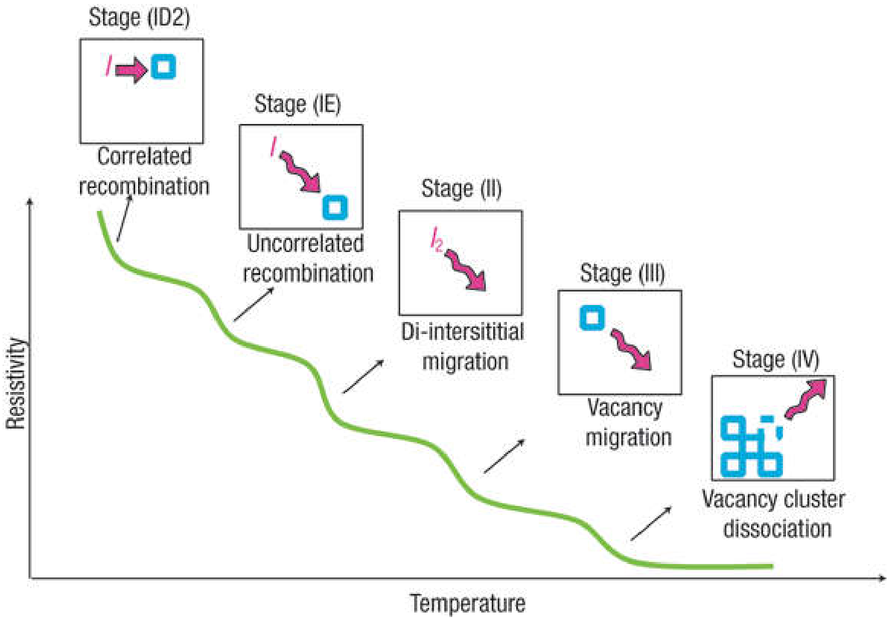

Figure 1.8 Schematic representations of the different recovery stages as a function of increasing temperature and associated mechanisms as proposed in electron-irradiated iron [30,31]. The labels I, I_2 and squares represent mono- and di-interstitials and vacancies respectively.

The derivative of the resistivity with respect to temperature shows peaks and they are referred as recovery stages. From the change-of-slope technique the effective activation energy for the recovery mechanism observed could be deduced.

Schematic of resistivity recovery stages after electron irradiation in iron is shown in Fig. 1.8, according to Takaki *et al*. [31] and the following interpretation was proposed.

- The first stages, between 23 K and 101 K, are due to the recombination of close *I–V* bound pairs with specific geometries.
- Stage (ID2), observed at 107.5 K, is related to the recombination of correlated defects (unbound *I–V* pairs belonging to the same Frenkel pair) by free migration of the interstitial.
- Stage (IE) (in the range 123–144 K for the irradiation doses considered) is attributed to the recombination of I and V belonging to different Frenkel pairs, as a result of I migration with migration energy $E_m(I) = 0.27 \pm 0.04$ eV.
- Stage (II) (164–185 K) is proposed to result from I_2 (di-interstitial) migration, with $E_m(I_2) = 0.42 \pm 0.03$ eV.
- Stage (III) (220–278 K) is suggested to result from V migration, with $E_m(V) = 0.55 \pm 0.03$ eV.
- An extra stage (520–550 K) observed at high doses and often named stage (IV), is attributed to the dissociation of defect clusters formed at stage (III).

The kinetics of large size vacancy and interstitial clusters has been studied by experiments as well as simulations. Especially the formation mechanism of <100> dislocation loops, which is not observed in other bcc metals, has been investigated by experiments as well as computer simulations. From the work of Yao *et al*. [32] a transition from ½ <111> interstitial dislocation loops to <100> is reported when heating from 300 °C to 500 °C in the microstructure of heavy-ion irradiated Fe. There are TEM observations that the dislocation loop evolve from interstitial type to vacancy type during annealing in iron [33]. There are experimental observations, which show increase in dislocation size by coalescence of small loops with same [34] and different Burgers vector [35]. Marian *et al*. [36] have reported the mechanism of <100> dislocation loops formation in iron by reactions between dislocation loops with Burgers vectors b = ½ <111> according to ½ <111> + ½ <111> = <100> by MD simulations (shown in Fig. 1.9.).

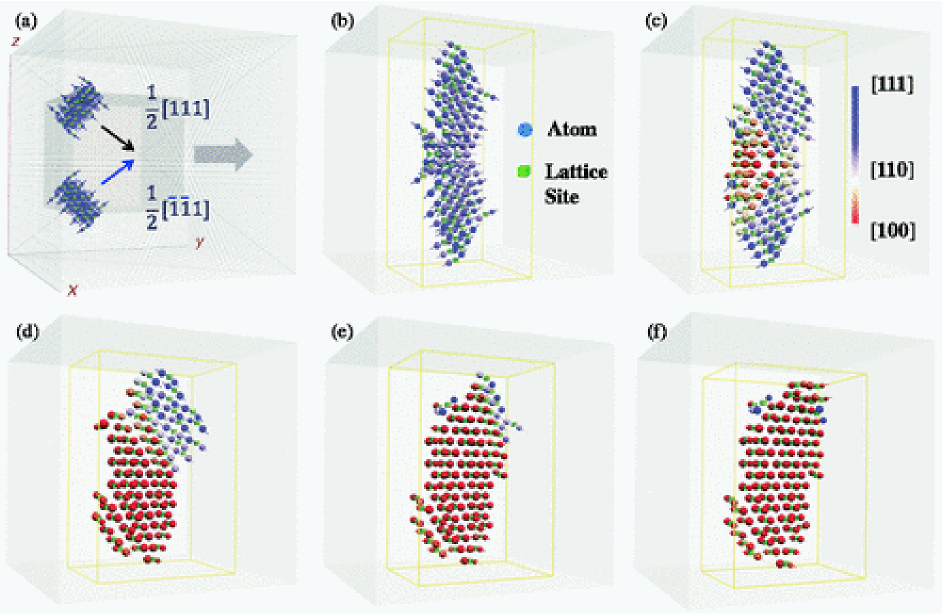

Figure 1.9 Snapshots at different times during the transformation process using Wigner-Seitz analysis. Spheres are atoms and boxes are vacant lattice sites. The lines indicate the vector between each atom and the closest lattice site. The colors indicate the orientation of individual interstitial from blue (<111>) to red (<100>). (a) Initial configuration. (b) Formation of a sessile junction. (c) Configuration after ~0.2 microseconds. (d) Partial [100] orientation. (e) Propagation of [100] orientation. (f) Complete [100] loop formed [36].

1.4. Solute interactions with radiation induced defects in iron

The vacancies and interstitials are produced in primary radiation damage. The defect kinetics, defect structure and microstructure are drastically changes depending on solutes present in the iron. To understand the effect of solutes on kinetics and structure of defects, the solute-defect interactions have been studied by experiments as well as computational tools. DFT and MD simulations have been used to study the solute interactions with radiation induced defects in iron. The interstitial solutes show strong attractive interactions with vacancy and vacancy clusters. The strength of the binding energy with the point defects increases according to the following order: H, C, N, He [37]. The interaction of substitutional solute atoms with point defects (vacancy and self-interstitial atom) in the Fe matrix has both elastic and chemical origins. For large size solutes, elastic effects are predominant, whereas for solute atoms with different electronic structures (which have very different number of *d* electrons) the chemical effects appear to be more important. For similar size solutes and matrices (e.g. *3d* elements in the bcc Fe matrix) chemical interactions also seem to come into play strongly. It is shown that magnetic interactions play an important role for the properties of the center series *3d* elements, especially for the antiferromagnetically coupling between V, Cr, and Mn impurities in Fe. For the *4d*, *5d*, and remaining *3d* transition metals the interaction with point defects is mainly governed by the solute size factor. The solute-solute interaction is mostly repulsive with a few exceptions. The solute interaction with vacancies (in most cases) is strong binding. The interactions of Cr and Mn solute with interstitials are attractive with strong binding [38].

The trapping of interstitial solutes by defects have been reported by MD simulations in iron. Anento *et al*. reported that the vacancy-carbon complex act as trap for self interstitial clusters in irradiated microstructure in iron [39]. Helium could be trapped at dislocation loops and He-dislocation loop defect cluster is formed in irradiated iron [40]. Terentyev *et al.* reported the effect of chromium on iron hardening *via* segregation on dislocation loops by atomic scale modeling. Results reveal that Cr atoms segregate at loop tensile strain region [41].

The solute-defect interactions have been investigated by using various experimental techniques also. The interactions of O and Y solute with vacancy defects in bcc Fe and

FeCr system are studied by He *et.al.* using positron annihilation spectroscopy (PAS) and secondary ion mass spectrometry (SIMS) techniques [42]. They also studied the V_n-Y_n-O_n cluster formation during ion implantation and post implantation annealing. Idczak *et al.*, have studied the interaction of Os, Re, Mo, Cr solute interactions with vacancies in iron by using Mössbauer and PAS techniques [43]. In agreement with theoretical findings attractive interaction was found except Cr. Hu *et al.*, have studied the He-V interactions by using thermal helium desorption spectroscopy and PAS in He^+ ion implanted Fe single crystals [44].

Defect-trapping of solutes in irradiated iron also studied by ion channeling and resistivity recovery experiments. Benkaddour *et al*. [45], have studied the Cr trapping at interstitial defects and Apostolopoulos *et al*. [46], have observed SIA defect trapping by C in electron irradiated FeCr and FeCrC alloys using resistivity recovery experiments. Kijek *et al*. [47], have observed 0.03 nm displacement of Mo solutes from their lattice site in He^+ ion irradiated FeMo alloy, due to interaction of V and SIA defects, from ion channeling experiments. Nuclear reaction analysis (NRA)/channeling technique has been used to study Deuterium trapping at defects in iron by Myers *et al*. [48]. TEM results show that He atoms reduce mobility of dislocation loops and act as nucleation sites for void formation [49]. Arakawa *et al*., have observed the one dimensional discrete motion of ½ <111> interstitial dislocation loops due to trapping by C, N, O impurities in electron irradiated iron foils by using *in-situ* high voltage TEM [50].

1.5. Outline of the thesis

From the literature survey of solute-defect interactions in iron, it is clear that the interactions of small interstitial and vacancy clusters with interstitial and substitutional solutes have been widely reported by DFT calculations and solute interactions with dislocation loops and voids are widely studied by MD simulations. TEM is widely used to study dislocation loop defects in irradiated iron. The effect of solute (C, H, He, Cr etc) concentration, irradiation dose and temperature on the radiation induced microstructure in model Fe and FeCr has been reported. However still some of questions remain unclear, which require detailed investigations for better understanding.

- What is the defect structure of solute-defect clusters formed in iron under radiation damage?
- How does solute-defect cluster evolve during radiation damage?
- How does the defect concentration affect solute-defect structure?
- What is the lattice location of solute in solute-defect cluster formed?

The aim of this thesis is, to find the defect structure of O-, Cr-defect clusters formed in ion implanted Fe and FeCr crystals which provide further understanding of solute interactions with radiation induced defects in iron based structural materials. First, solutes (O and Cr) and defects are introduced in Fe and FeCr crystals by ion implantation and post implantation annealing is performed to form solute-defect clusters. The displacement of solutes from its equilibrium site is measured by ion beam analysis based lattice location measurements. This displacement is used as key parameter to find the defect structure.

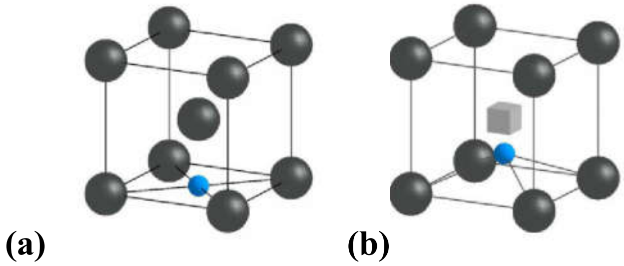

Figure 1.10 (a) Oxygen at octahedral interstitial site and (b) O-V complex (O displaced towards vacancy) in bcc Fe. Small sphere, square represent O, V respectively.

For example DFT predicts that the octahedral interstitial site is the equilibrium position for O in Fe. Due to the attractive interaction of O with a mono vacancy it forms O-V defect complex where O displaced 0.02 nm towards vacancy centre as shown in Fig. 1.10 [51]. Similarly, the binding energy and lattice location of O and Cr in various O-V, O-SIA, Cr-SIA and Cr-V defect clusters are studied by using DFT calculations, to find the defect cluster which is responsible for the solute trapping. Slow positron Doppler broadening spectroscopy (SPDBS) is used to study vacancy defects and ion beam dechanneling measurement is used to study type of defects.

This first chapter on introduction is followed by chapter 2. The chapter 2 consists of experimental (ion implantation, ion beam analysis, ion channeling and positron annihilation spectroscopy) and computational tools (DFT) used for studying defect interactions and defect structure in ion implanted Fe and FeCr.

Chapter 3 comprises the studies of O interactions with self interstitial defects in iron. The O^{18} ions are implanted in bcc Fe(110) single crystal and annealed at 400 °C. Lattice location of O^{18} is studied by ion channeling technique. Self ions are implanted over the O^{18} implanted profile and annealed. Lattice location is measured again to study effect of self ion implantation. The range of defects and type of defect formed at O^{18} depth is also verified by ion channeling technique. Positron annihilation spectroscopy technique is used to study vacancy defects. Further, the O interactions with self interstitial defects are studied by using DFT calculations and compared with experiments.

Chapter 4 deals with O interactions with vacancy defects in iron. The O^{18} ions are implanted in Fe(100) and self ions are intentionally implanted at twice the depth of O^{18} concentration profile so that more vacancies (due to $R_p/2$ effect) will be present at O^{18} depth profile. The ion implanted Fe(100) is annealed at 400 °C. The lattice location of O^{18} is measured by ion channeling technique. With the aim of increasing vacancy concentration at O^{18} depth self ions are implanted and annealed again. The lattice location of O^{18} is measured again. The depth and type of defects are studied by ion channeling and SPDBS techniques. Oxygen interactions with various vacancy clusters are studied by using the DFT calculations. The DFT predicted lattice location of O^{18} within various O^{18}-V clusters is compared with experiments and the defect structure is identified.

In chapter 5, O and Cr interactions with defects in iron are studied. The Cr ions are implanted in bcc Fe(100) and annealed at 400 °C. Lattice location of Cr is identified. The O^{18} ions are implanted over Cr depth profile and annealed to study Cr and O interactions with interstitial defects in Fe. The lattice location of Cr as well as O^{18} is measured. The type and depth of defect is studied by ion channeling and SPDBS measurements. The O and Cr interactions with interstitial defects are studied by DFT calculations. The DFT predicted lattice location of Cr and O are compared with experiment and the results are discussed in the context of effect of low Cr concentration on O-defect cluster formed.

In chapter 6, the interaction of O with defects in iron-chromium alloy is studied. The O^{18} ions are implanted in Fe15%Cr(100) single crystal alloy and annealed at 400 °C. The lattice location of O^{18} is measured. The excess vacancy defects are introduced over O^{18} depth profile by self ion implantation and annealing. The type and depth of defects (ion channeling) and vacancy defects (positron annihilation spectroscopy technique) are studied. The O and Cr interactions with vacancy defects are studied by DFT calculations and lattice locations of O^{18} in various configurations are compared with experiment. The resultant defect structure is identified and results are discussed in the context of effect high Cr concentration on O-defect clusters formed in FeCr alloy.

In chapter 7, all experimental and DFT results are summarized and the scope for future works are given.

Chapter 2

Experimental and computational methods

In this thesis the ion implantation, ion beam analysis and slow positron Doppler broadening spectroscopy (SPDBS) experimental techniques are used. To interpret the experimental results simulations of ion implantation, ion beam analysis and SPDBS are carried out by SRIM, FLUX7 program and VEPFIT code respectively. In addition, DFT studies are performed using Vienna Ab-initio Simulation Package (VASP) code. In this chapter, the principle, instrument and experimental details of ion implantation, ion beam analysis and SPDBS experiments are given. Theoretical background and details of ion channeling simulations and DFT calculations are described.

2.1. Ion implantation

Before discussing ion implantation and ion beam analysis, it is good to mention the interactions of energetic ions with crystalline solid. A schematic of ion-solid interaction is shown in Fig. 2.1.

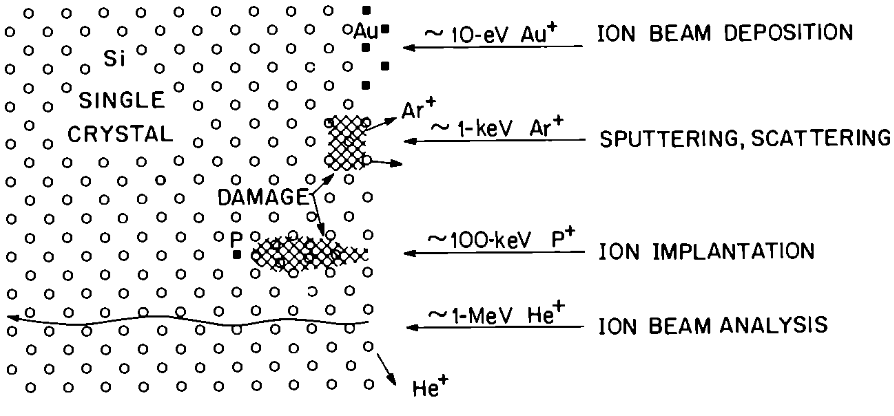

Figure 2.1 Schematic illustration of ion beam interactions with a crystalline solid [52].

Ion-solid interactions are mainly depending on energy and mass of incident ions. Low energy ion (10-100 eV) comes to rest at surface of solids and forms epitaxial layers. Heavy ions (with 1 keV) sputter the solid surface due to large energy transfer to target. At higher energies (100-300 keV), ion comes to rest around 100 nm depth in a disordered lattice created by its passage. The 1 MeV light ions are used for ion beam analysis of solid state materials [52].

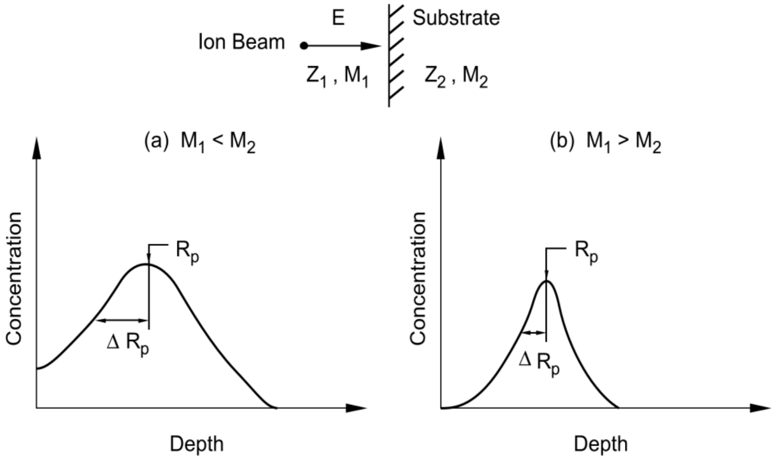

Figure 2.2 The depth distribution of implanted atoms in an amorphous target for the cases in which the ion mass is (a) less than the mass of the substrate atoms or (b) greater than the mass of the substrate atoms. The mean depth, R_p, depends on ion mass, M_1, and incident energy, E, whereas the relative width, $\Delta R_p/R_p$, of the distribution depends primarily on the ratio between ion mass and the mass of the substrate ion, M_2. (Adopted from [53])

In ion implantation process, high energy ions (hundreds of keV to few MeV energy) are bombarded into a solid using an ion accelerator which results in the introduction of desired atoms into the surface layer of a solid substrate. Ion implantation is a non-equilibrium process which is alternative method to equilibrium process of introducing dopant atoms into the lattice. Ion implantation also induces radiation damage in the solids as the case of neutrons (neutron damage is described in section.1.1 of chapter.1.). Range distribution of implanted ions in substrate is approximately Gaussian in shape and they are characterized by projected range, R_p, and a straggling, ΔR_p, about this mean value, which is pictured in

Fig. 2.2. For simulation of ion and damage profiles of ion implanted Fe the Stopping and Range of Ions in Matter (SRIM) software is used [54].

2.2. Accelerator used for ion implantation and ion beam analysis

In present work, 1.7 MV Tandetron accelerator (HVEE, The Netherlands) at Materials Science Group, Indira Gandhi Centre for Atomic Research, Kalpakkam, is used for ion implantation and ion beam analysis. Ions of energy ranging from 200 keV to 15 MeV could be obtained from this accelerator which depends on the terminal voltage (V) and charge state (q) of the ions. The photograph and parts of the accelerator are shown in the Fig. 2.3. First, negative ions of desired atomic species are produced by ion source of the accelerator. The 1.7 MV Tandetron accelerator has a high brightness duoplasmatron ion source which is used for the production of H^+ or He^+ ions and a sputter ion source SNICS (Source of Negative Ions by Cesium Sputtering) for producing negative ions from solid targets. The positive ion produced by duoplasmatron ion source is converted to negative ions by passing through a charge exchange canal which is filled with lithium vapor. The singly charged negative ions produced in the ion source are focused by electrostatic einzel lens into the axis of a high resolution mass analyzing magnet. The magnet is used for selection of required ions from the ion source and injected into the accelerating tube. The mass resolution (M/ΔM) of the magnet is 190.

The Cockroft – Walton type capacitive coupled parallel-fed solid state power supply is used for the generation of high voltage to the terminal (voltage from 100 kV to 1.7 MV with a voltage stability of ±100 V). The ions entering into the accelerating tube will gradually gain energy due to the applied voltage in the power supply at the middle of the accelerating column. The stripper canal present at the centre of the accelerating tube converts the negative ions into positive ions with different charge states of the ions. The conversion of ions is taken place by interacting with the inert gas filled in this canal. A turbo molecular pump powered by a motor generator at the canal has been installed for the recirculation of the stripper gas. The voltage (V) is set at

$$V = \frac{(E - E_p)}{1 + q} \tag{2.1}$$

where E is the required energy, E_p is pre-injection energy of the ion, q is the charge state of the ion after post acceleration. The accelerating tube and power supply are maintained with a base pressure of 1×10^{-7} mbar. The entire accelerating structure consisting of the accelerating tube, the high voltage terminal and the power supply is enclosed in a pressure vessel filled with SF_6 gas at 6 kg/cm^2 for achieving high voltage insulation.

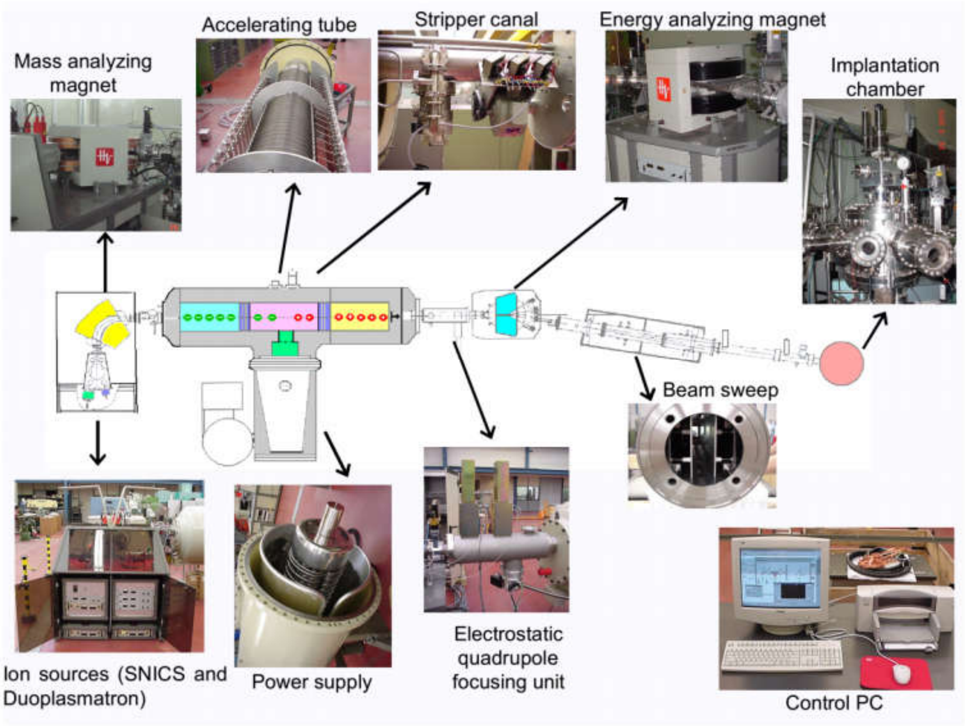

Figure 2.3 Photograph of the 1.7 MV Tandetron accelerator at IGCAR Kalpakkam and its various components.

The ions emerging on the high energy side of the machine are focused by electrostatic quadrupole lens into the axis of the energy analysing magnet. The high energy analysing magnet selects the ion beam according to the energy of the ions and switches the beam to the experimental ports located at ±10° and ±30° angular positions. An implantation beam line with the beam sweep system, neutral trap, beam profile monitor and retractable slits for beam collimation has been installed at the +10° port of the switching magnet. All the controls of the accelerator are done from the PC connected to a Programmable Logic Controller which in turn is connected to accelerator components through optical cables. The number of implanted ions is given by the product of the ion flux (ion/cm^2.s) and the implantation time, *t*. The flux of charged particles can be measured by a current integrator, which is connected to the sample. The number of implanted ions can be calculated using the following equation,

$$N = \frac{Q}{qA} \tag{2.2}$$

where Q is the collected charge (measured by the current integrator), q – is the charge state of the ion and A – is the cross sectional area of ion beam.

2.3. Ion beam Analysis

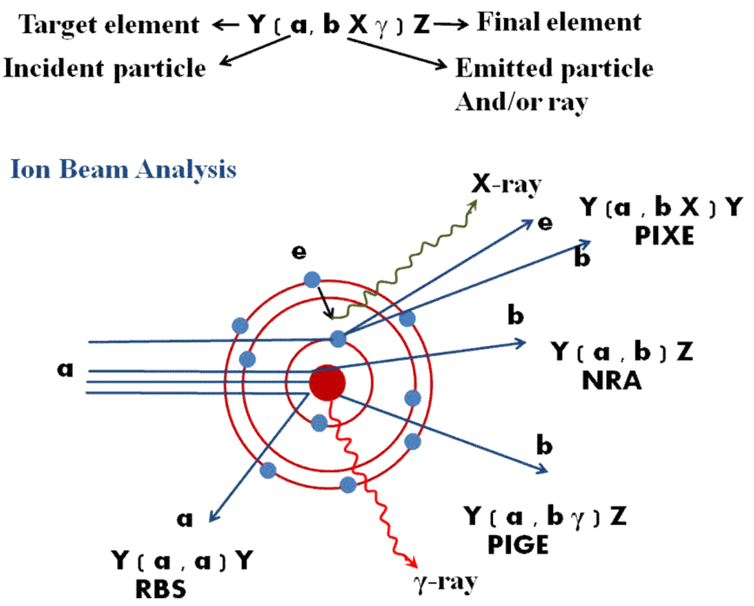

Figure 2.4 Schematic of ion-atom interactions and correspond ion beam analysis techniques [55,56].

Ion Beam Analysis (IBA) techniques are based on the ion-atom interactions. When a high energy charged particle strikes a target material, it interacts with the electrons and nuclei of the target atoms, slows down at some depth of the material. This ion-atom interaction can lead to the emission of particles or radiation whose energy is characteristic of the elements which constitute the target. By detecting and analyzing this emitting particle/radiation, the materials properties are studied by various ion beam analysis methods. The basic process of ion-atom interaction is described in Fig. 2.4.

PIXE: When an ion interacts with an atom, it ionizes by knocking out a electron from inner shell. These inner shell vacancies are filled by outer shell electrons with emission of characteristic X-rays of elements. This is the principle of particle induced X-ray emission (PIXE) technique where characteristic X-rays from the atomic fluorescence (Y (a,a'X) Y) is detected and analyzed to study concentration of elements present in a target material. At good experimental conditions a detection limit of ~1 parts per million (ppm) for thin foils and ~10 ppm for thick samples can be achieved. Sensitivity for detecting light element is lowere in PIXE.

PIGE: In particle induced gamma-ray emission (PIGE) technique, characteristic gamma-ray coming from nuclear reaction (Y (a,bγ) Z) is detected. PIGE is particularly useful for detecting light elements such as F or Na which are inaccessible by PIXE.

NRA: Ion beams can also induce a particular nuclear reaction of an isotope present in a solid material. By detecting the particles emitted from the nuclear reaction (Y (a,b) Z), depth profiling of particular isotope could be done. This nuclear reaction analysis technique is useful for profiling light elements in materials consisting of heavy elements.

RBS: In Rutherford backscattering spectrometry (RBS), high energy ions scattered from the target material, based on nuclear scattering (Y (a,a) Y), are detected. From the electronic energy loss and nuclear scattering theories, the depth profile and concentration profile of elements are quantified. This method is mainly useful in thin film analysis.

Elastic Recoil Detection Analysis (ERDA) and Non-Rutherford backscattering spectrometry (NRBS) have also been used to some extent for the detection of light elements (C, N, O) in heavy matrixes. The applications and other useful parameters of ion beam based analytical techniques are given in Table 2.1.

Table 2.1 Methods and applications of ion beam analysis [57].

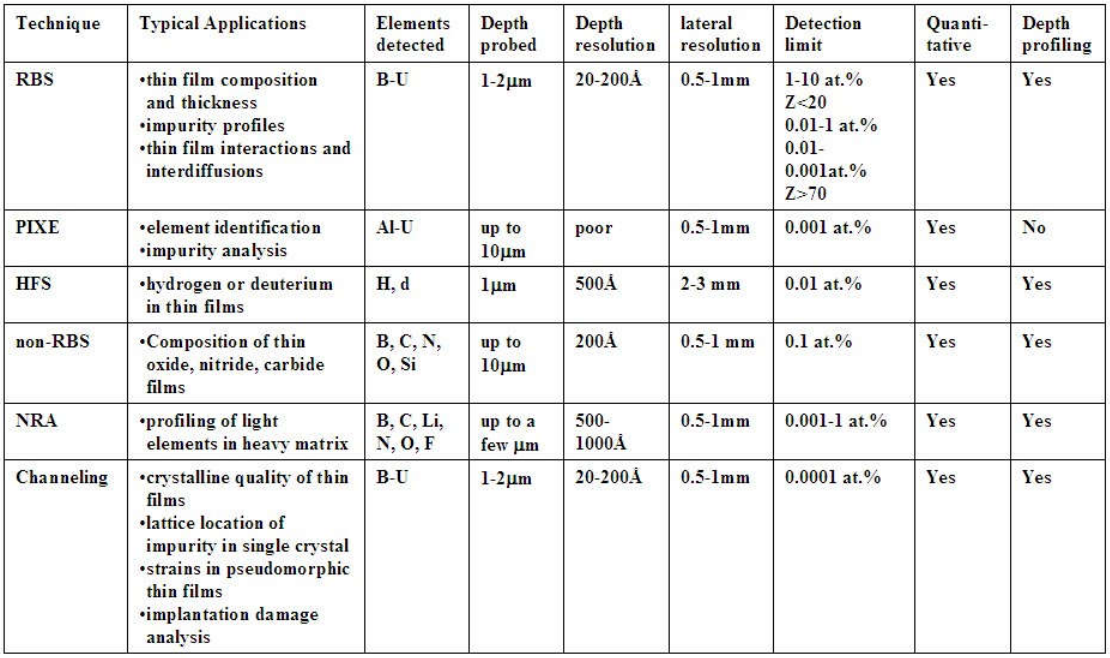

Technique	Typical Applications	Elements detected	Depth probed	Depth resolution	lateral resolution	Detection limit	Quanti-tative	Depth profiling
RBS	•thin film composition and thickness •impurity profiles •thin film interactions and interdiffusions	B-U	1-2μm	20-200Å	0.5-1mm	1-10 at.% $Z<20$ 0.01-1 at.% 0.01-0.001at.% $Z>70$	Yes	Yes
PIXE	•element identification •impurity analysis	Al-U	up to 10μm	poor	0.5-1mm	0.001 at.%	Yes	No
HFS	•hydrogen or deuterium in thin films	H, d	1μm	500Å	2-3 mm	0.01 at.%	Yes	Yes
non-RBS	•Composition of thin oxide, nitride, carbide films	B, C, N, O, Si	up to 10μm	200Å	0.5-1 mm	0.1 at.%	Yes	Yes
NRA	•profiling of light elements in heavy matrix	B, C, Li, N, O, F	up to a few μm	500-1000Å	0.5-1mm	0.001-1 at.%	Yes	Yes
Channeling	•crystalline quality of thin films •lattice location of impurity in single crystal •strains in pseudomorphic thin films •implantation damage analysis	B-U	1-2μm	20-200Å	0.5-1mm	0.0001 at.%	Yes	Yes

2.4. Rutherford backscattering spectrometry- experimental details

RBS technique is widely used in ion beam analysis of thin films and bulk materials because of its non-destructive, rapid and capability for quantitative analysis without standards. It provides depth distribution of the impurities present in the near surface region (few μm) and thereby stoichiometry of composition in the sample. It also provides depth information of the defects present in the single crystal samples in channeling conditions. In RBS, MeV ion beam (He^+/H^+) is directed on to the sample and the energy and yield of the backscattered ions are detected. The detected energy and yield depend on the mass of the atoms in the sample and the depth distribution of the atoms in the sample. The material composition can be determined from simulation of RBS spectrum when it compared with experiments.

The schematic diagram of experimental set up of RBS is shown in Fig. 2.5. The incident probe is a mono-energetic light ion beam, typically MeV He^+/H^+ ions. The scattered He^+/H^+ particles from the target are detected and energy analyzed by a solid state particle detector positioned at a backscattered angle of 165 ° with respect to the incident ion beam. The Si surface barrier detector (with energy resolution of 20 keV) is used in our experiments. The detected particle energy and corresponding signal voltage are processed by preamplifier and spectroscopic amplifier. Finally a multi channel analyzer (MCA) is used to convert the amplified detector signals into RBS spectrum. The energy per channel number of MCA also can be measured for the particular voltage gain, which is used to convert the channel number into energy.

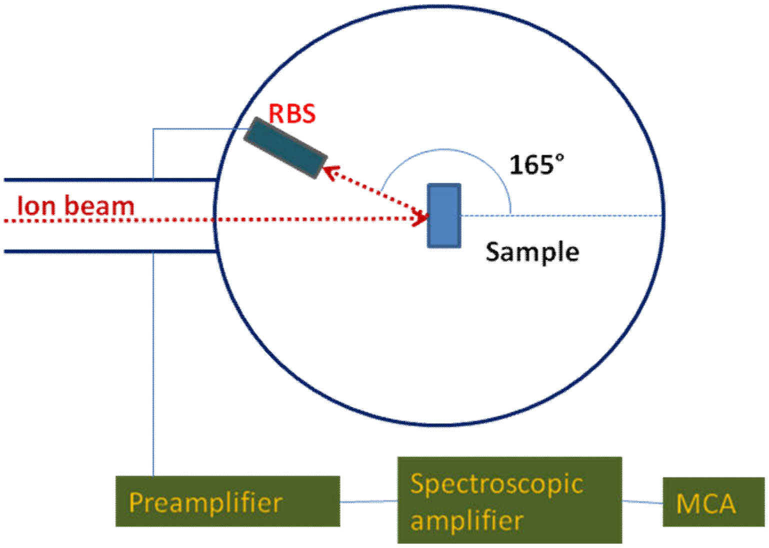

Figure 2.5 Schematic diagram of RBS experimental set up.

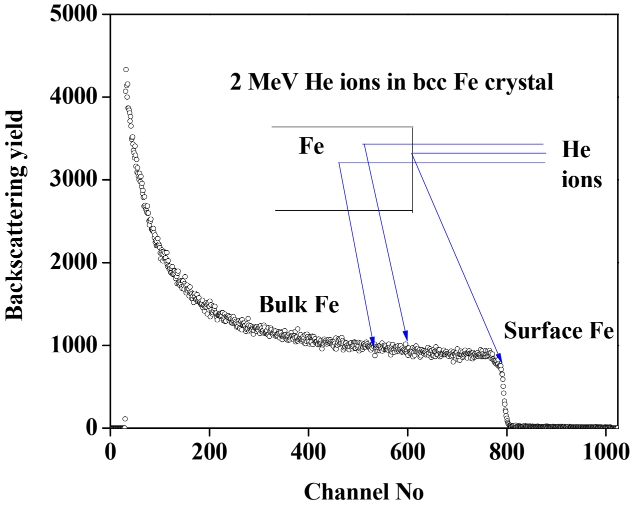

Figure 2.6 Typical RBS spectrum taken by 2 MeV He ions in bcc Fe.

Applying the principles of conservation of energy and momentum in the binary elastic collision model, the energy (E_s) of the scattered particle is,

$$E_s = \left[\frac{(M_t^2 - M_p^2 \sin^2\theta)^{1/2} + M_p \cos\theta}{M_p + M_t} \right]^2 E_{in} \tag{2.3}$$

where E_{in} is energy of the incident ion and the quantity in the bracket is called as kinematic factor (K factor) which depends on the target (M_t) and projectile (M_p) masses and the scattered angle (θ). Since the projectile mass and scattering angle are constant, the K factor highly depends on the masses present in the target. The backscattering yield is,

$$Y = Q \times \frac{d\sigma}{d\Omega} \times N \times t \times \Delta\Omega \tag{2.4}$$

where Q is the incident ion flux, $\frac{d\sigma}{d\Omega}$ is the differential scattering cross section, N is the atomic density of target, t is the thickness and $\Delta\Omega$ is the detector solid angle. The scattering cross section can be calculated using the Coulomb repulsion force between the projectile and target nuclei as long as the distance of closest approach is large compared to nuclear dimensions, but small compared to the Bohr radius a_0 = 0.53 Å. Under this assumption, the differential scattering cross section can be written as (in laboratory frame of reference),

$$\frac{d\sigma}{d\Omega}=\left(\frac{Z_pZ_te^2}{4E}\right)^2\left(\frac{4}{\sin^4\theta}\right)\frac{\left[[1-((M_p/M_t)\sin\theta)^2]^{1/2}+\cos\theta^2\right]^2}{[1-((M_p/M_t)\sin\theta)^2]^{1/2}} \tag{2.5}$$

where Z_p, Z_t are the atomic numbers of projectile and target atoms, θ is the scattering angle. Since the scattering cross section is proportional to square of the atomic number, RBS is highly sensitive to high Z elements in a low Z matrix.

A typical RBS spectrum obtained in Fe(110) crystal at random direction is shown in Fig. 2.6. The depth information of atoms in the host matrix can be estimated by using the energy loss of the projectile inside the matrix. The energy loss depends on the stopping power of the matrix. The stopping power *[S]* can be written as,

$$[S]=\frac{K}{\cos\theta_{in}}\left(\frac{dE}{dx}\right)_{in}+\frac{1}{\cos\theta_{out}}\left(\frac{dE}{dx}\right)_{out} \tag{2.6}$$

where θ_{in}, θ_{out} are the incident and scattering angle of the projectile, $\left(\frac{dE}{dx}\right)_{in}$ is energy loss of the incident projectile in the matrix and $\left(\frac{dE}{dx}\right)_{out}$ is the energy loss of the scattered projectile in the matrix. The depth (Δx) of the Fe / impurity in the matrix can be obtained from the following relation,

$$\Delta x=\frac{\Delta E}{[S]} \tag{2.7}$$

where ΔE is the energy width found from the RBS spectrum.

2.5. Nuclear reaction analysis – experimental details

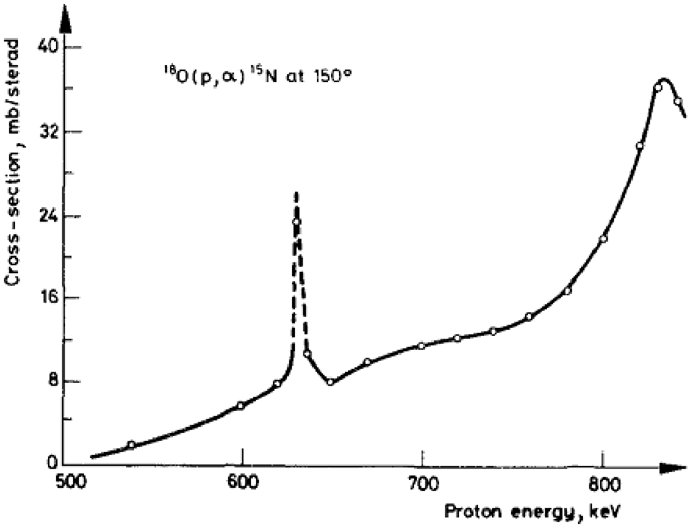

Figure 2.7 Cross section of $O^{18}(p,\alpha)N^{15}$ nuclear reaction adopted from reference [58].

Our experimental and theoretical studies focus on O interactions with defects in bcc Fe crystals. If we introduce O ions in to bcc Fe crystals, O signals will be overlapped with Fe signals in the RBS spectrum. Getting O signal is very difficult due to its low atomic number as well as low concentration giving raise to small backscattering yield. To overcome these difficulties the NRA technique is used to get O signal. The O^{18} isotope is introduced instead of O. The O^{18} signal is obtained by detecting the out coming α-particle yield from the well-known $O^{18}(p,\alpha)N^{15}$ nuclear reaction which has a broad resonance width at 820 keV (shown in Fig. 2.7) and Q-value of 3.981 MeV [50].

The schematic diagram of NRA experimental set up is shown in Fig. 2.8 which is similar to RBS set up. The same Si-surface barrier detector was used for NRA analysis also. However, RBS and NRA spectra are collected separately. During NRA a 12 μm thick Mylar window is inserted in front of the detector to suppress the backscattered protons, by turning a rotary drive without breaking the vacuum. During RBS the Mylar window is removed using same rotary drive. The thickness of the Mylar foil is chosen such that proton signal from Fe surface as well as NRA signal from O^{18} is well resolved in the MCA spectrum. Figure 2.9 shows the NRA spectrum from the nuclear reaction $O^{18}(p,\alpha)N^{15}$ reaction obtained with 850 keV protons when the Mylar foil is introduced before the detector. SRIM calculations show that 12 μm Mylar foil can stop protons of energy up to 700 keV and α-particles up to 2.75 MeV. But the backscattered protons are not completely stopped and the tailing signal below channel number 130 is coming from the high energy backscattered protons which are not absorbed completely. The alpha particle yield observed in the channel range 150–350 is clearly seen. Oxygen concentration depth profile is determined experimentally by taking the NRA data at various incident proton energies from 830 to 890 keV. The proton energy of 850 keV has shown the maximum α-yield and it is chosen for all NRA analysis.

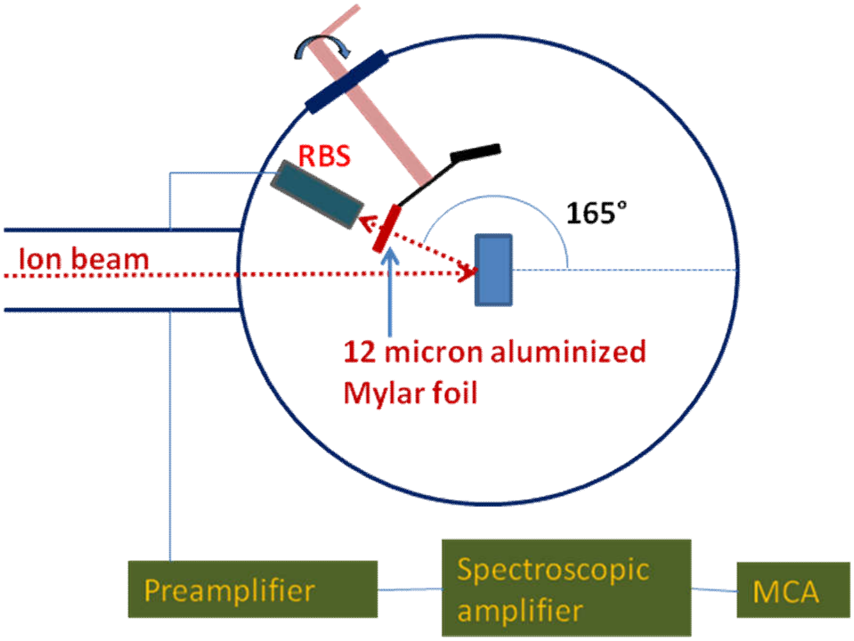

Figure 2.8 Schematic of NRA experimental set up.

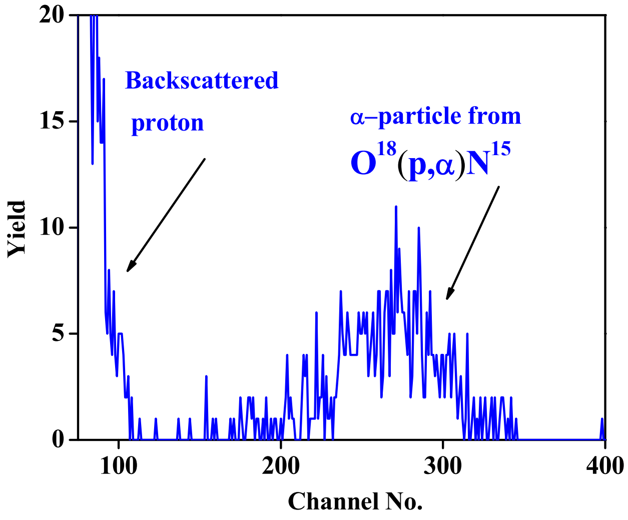

Figure 2.9 NRA spectrum obtained after introducing Mylar foil in front of detector.

2.6. Particle induced X-ray emission – experimental details

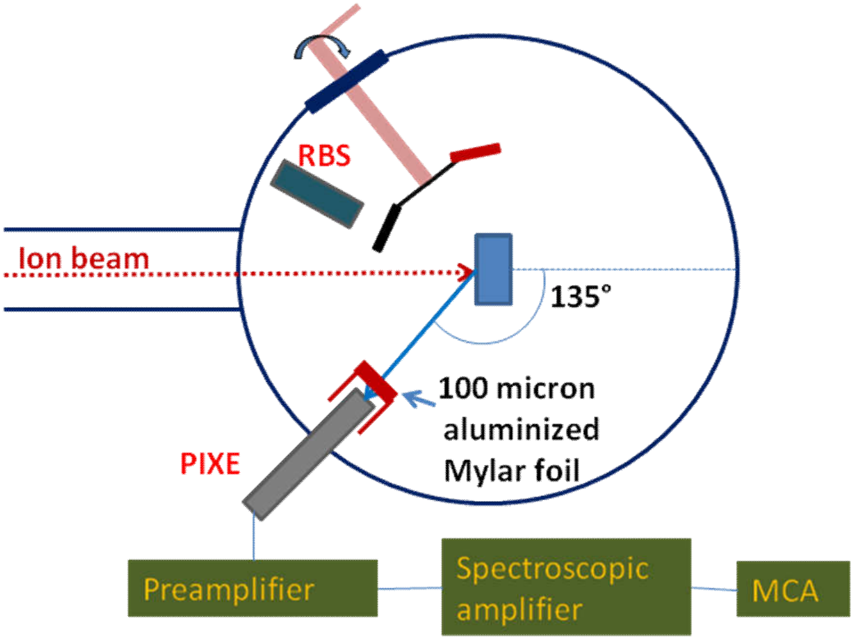

Figure 2.10 Schematic diagram of PIXE experimental set up.

Aim of this thesis is to study O and Cr interactions with defects in bcc Fe crystals. In RBS spectrum Cr signals cannot be identified from Fe signals since Fe and Cr have closer mass numbers. To overcome these difficulties, PIXE technique is used to identify Cr signals from Fe matrix signal. The schematic diagram of PIXE experimental set up is shown in Fig. 2.10.

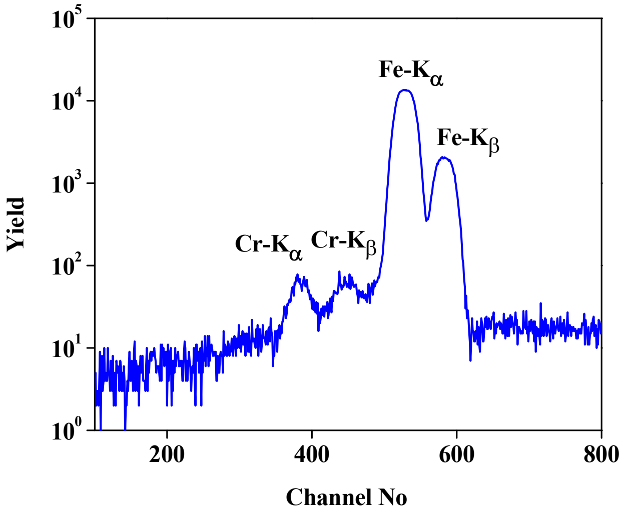

Figure 2.11 The PIXE spectrum taken in Cr implanted and annealed bcc Fe crystal.

The PIXE measurement is performed with 890 keV protons in Cr ion implanted Fe(100). The distance between the sample center and the beryllium (Be) window of Si(Li) detector is 10 cm and the angle between the detector head and the beam direction is 135°. A 100 μm Mylar absorber is kept in front of the detector to reduce the dominant low energy X-ray peaks and bremstrahlung. A typical PIXE spectrum obtained in Cr implanted bcc Fe is shown in Fig. 2.11. The Cr-K_α and Cr-K_β signals are clearly seen in addition to Fe signals.

2.7. Ion channeling

Ion atom interaction depends on the impact parameter of incident ion which is related to how much close an ion approaches nucleus (shown in Fig. 2.12). For small impact parameter, comparable to nuclear size, ion loses its large energy (~100 keV) by binary collision with nucleus and deflected at a large scattering angle. For smaller impact parameter, ion loses energy in the range of 1-100 eV due to interactions with inner electrons. For large impact parameters, ion losses its energy due to interactions with valence electrons.

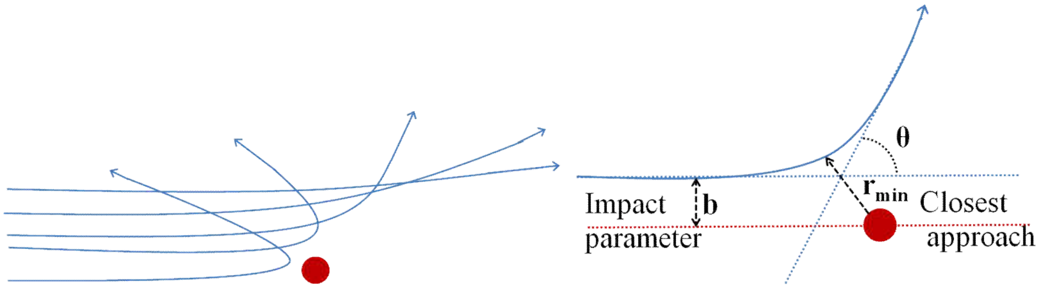

Figure 2.12 Ion deflections by an atom (b - Impact parameter, r_{min} – distance of closest approach, θ - scattering angle).

In a single crystalline material, atoms are arranged in a periodic manner. Correlated small scattering angle deflections of ions by a row of atoms in crystalline solid steer the ions away from the atomic row. This is the channeling of ions in crystalline solid as shown in Fig. 2.13. The ion follow wave like trajectories with few 10 nm of wavelength inside the crystal. The characteristics of ion channeling has been observed in many experiments for example (i) backscattering ion channeling [59] (ii) transmission ion channeling [60], (iii) emission channeling [59] etc. The backscattering ion channeling in combination with NRA and PIXE experiments are used in this thesis. The RBS yield of a crystalline matrix is considerably reduced due to channeling effect which can be seen in Fig. 2.14., where backscattering yield at <100> axis of bcc Fe single crystal is reduced compared to the random spectrum.

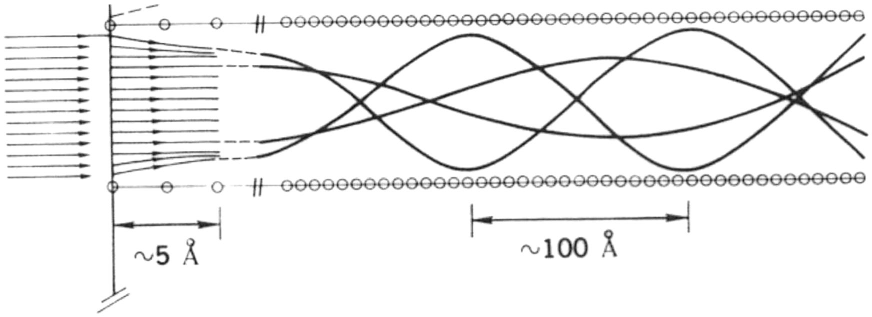

Figure 2.13 Trajectory of ions scattered at surface as well as inside crystal where channeling occurs [52].

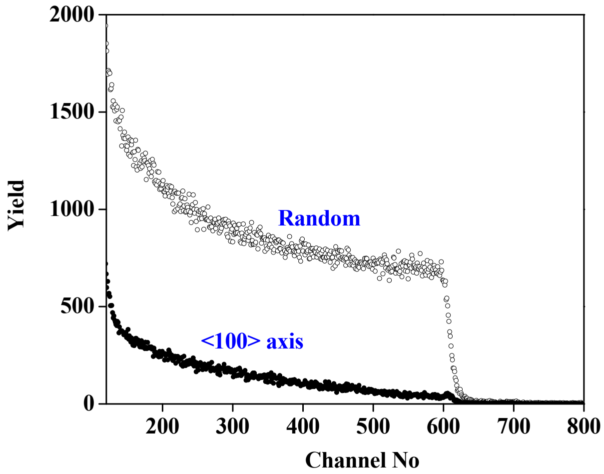

Figure 2.14 RBS spectra at random and <100> axial directions of the bcc Fe(100) crystal recorded with 2 MeV He^+ incident ions.

Another important experimental observation of channeling effect is the tilt angular scan where close encounter probability (small impact parameter) of ions are measured with small tilt angles around an axis/plane of a crystal. Schematic of a tilt angular scan is shown in Fig. 2.15. The parameters χ_{min} is given by yield at axial direction normalized to random level. The half angle of full width at half maximum of tilt angular scan (here onwards this will be called as width) $\Psi_{1/2}$ depends on the crystallography of material. The relation between the crystallographic parameters and tilt angular scan parameters are obtained in literature by numerically fitting the experimental data, which are presented in Eq. (2.8) and Eq. (2.9) [52].

$$\psi_{1/2} \propto \sqrt{\frac{Z_1\overline{Z}}{E\overline{d}}} \tag{2.8}$$

$$\chi_{\min} = Nd\pi(2u_1^2 + a^2) \tag{2.9}$$

where Z_1, E - atomic number, energy of ion, $\overline{Z}$, $\overline{d}$ - average atomic number and lattice spacing of crystal, N - atomic density of crystal, d - atomic spacing in the atomic row, u_1 - thermal vibration amplitude, a - Thomas Fermi screening radius (which will be discussed later).

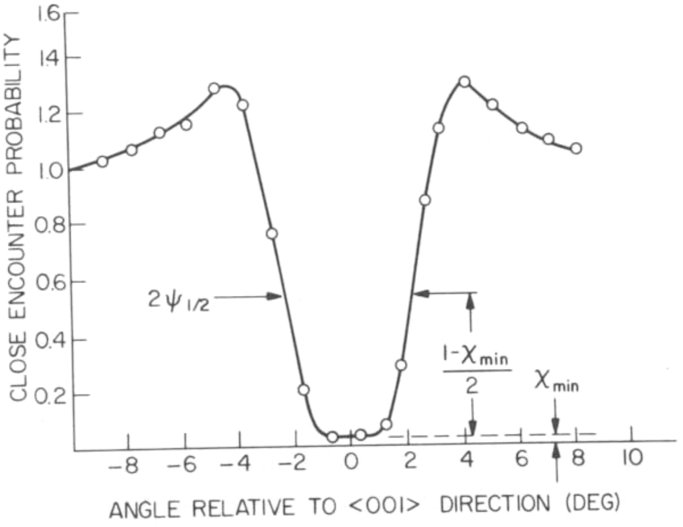

Figure 2.15 Schematic of a tilt angular scan.

2.8. Ion channeling – experimental set up

The ion channeling experimental set up is shown in Fig. 2.16. The ion beam, detector and a sample manipulator are the main parts of experiment. With the use of sample manipulator (five axes goniometer), crystallographic direction of the sample is aligned with beam direction and RBS, NRA and PIXE experiments are done in channeling directions.

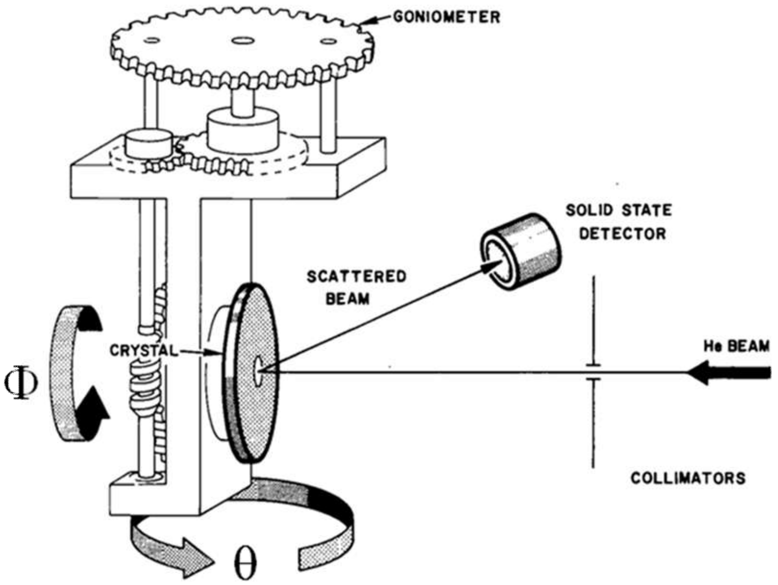

Figure 2.16 Ion channeling experimental set up.

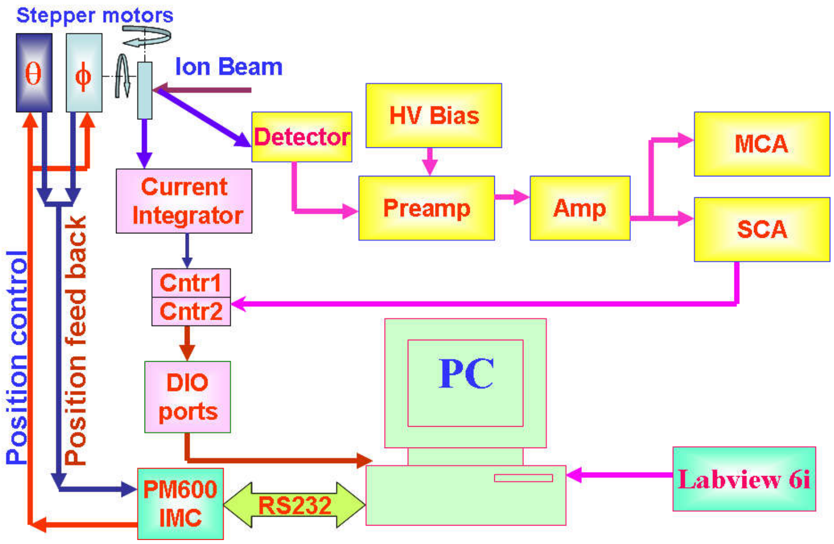

Figure 2.17 In–house developed virtual instrument based automation set up of RBS/channeling experiment [61].

Goniometer consists of *X*, *Y*, *Z* position adjustments which can be done manually and azhimuthal angle (*Φ*) and tilt angle (*θ*) are controlled by two computer controlled stepper motors. The *Φ* can be adjustable from 0-360° in steps of 0.001° and *θ* can be varied ±180° in steps of 0.01°. For determining the crystallographic direction, sample is tilted by 5° from the normal, backscattering yield of a small window in the high energy side of RBS spectrum using a single channel analyzer (SCA), is taken at various azimuthal angles from 0-360° in steps of 2° for a fixed incident flux using in-house developed virtual instrument based automation set up [61] (schematic diagram as shown in Fig. 2.17). A measured *Φ*-scan from the system is shown in Fig. 2.18 which used for manipulate the crystal orientations. Angular positions of the planar dips shown in Fig. 2.18 are plotted in a polar plot. The points in diagonally opposite direction corresponding to same planes are joined with straight line. The point of intersection of these lines corresponds to axial direction.

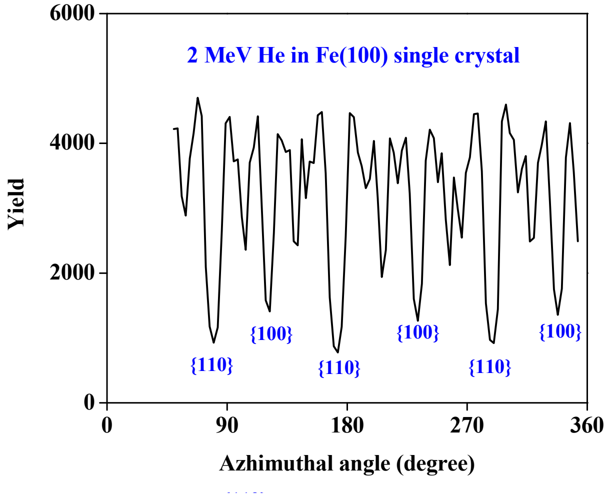

Figure 2.18 Azhimuthal angular (*Φ*) scan measured in bcc Fe(100) crystal.

2.9. Dechanneling by defects

Experimental observation of channeling effects in real crystals is different from ideal crystals due to presence of defects. A part of channeled ions is deflected from the channeling trajectory due to presence of defects as shown in Fig. 2.19. This dechanneling effect depends on type of defects and on energy of incident ions, whereas the direct scattering mechanism is energy independent. The dechanneling parameter (*DP*) due to defects can be measured by using RBS/channeling experiments. The experimentally measured dechanneling parameter is given by,

$$DP = -\ln\left[\frac{1-\chi_D}{1-\chi_V}\right] \tag{2.10}$$

where χ_V - χ_{min} of pristine, χ_D - χ_{min} of defective crystal. The type of defects at a particular depth can be determined by energy dependence of the dechanneling parameter (*DP*) [52]. The *DP* of point defects, stacking faults, dislocations show energy dependence of $E^{-0.5}$, E^{0}, $E^{0.5}$ respectively as shown in Fig. 2.20. Theoretically the *DP* is related to the defect density (n_D) and dechanneling factor of defect (σ_D) by,

$$\frac{d}{dz}(DP) = n_D\sigma_D \tag{2.11}$$

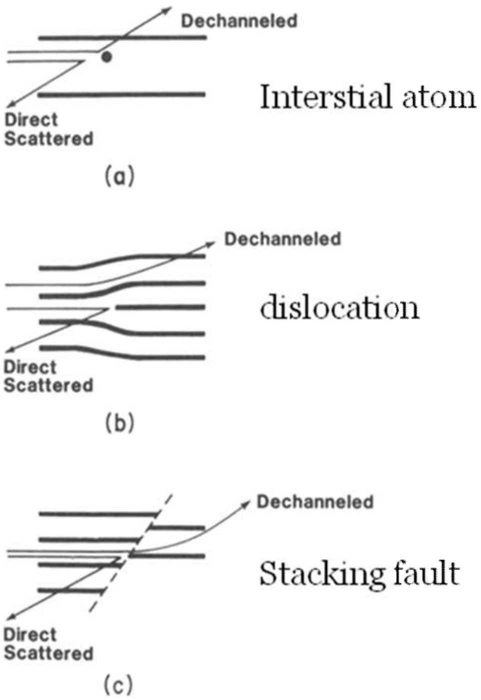

Figure 2.19 Pictorial representation of dechanneling by defects [52].

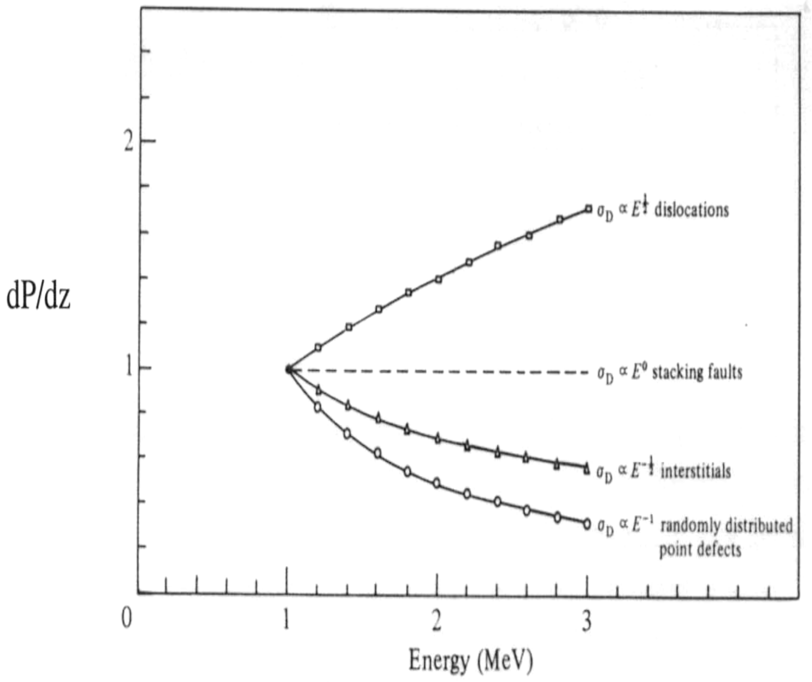

Figure 2.20 Energy dependence of dechanneling parameter for different type of defects [52].

Dislocation loops are also one of the observed defects in ion implanted iron. Theoretical framework reported by Kudo is extensively used for the analysis of dislocation loops [54]. Energy dependance of dechanneling behavior of dislocation loops is same as dislocation defects, when the σ_D (dechanneling factor) is less than the dislocation loop radius *R*. When the dechanneling width is comparable to loop radius *R* the dechanneling factor changes to energy independent. The energy at which the dechanneling factor changes from energy dependent to independent is called transition energy (E_s). The transition energy and dislocation loop radius is related by.

$$E_s = aR^2 \tag{2.12}$$

$$a = 0.8853 a_0 (Z_1^{1/2} + Z_2^{1/2})^{-2/3}$$

where a is Thomas Fermi screening radius (0.142Å for iron) which is derived from the Thomas Fermi screened coulomb potential of atomic string, a_0 - Bohr radius of 0.528 Å. The R is in units of Burgers vector and E_s in units of keV.

The dislocation loop density at depth z can be calculated by using the expression,

$$n_D(z) = \frac{1}{\sigma_D}\frac{d}{dz}(DP) = \frac{slope \times \sqrt{E}}{\sigma_D} \tag{2.13}$$

$$\sigma_D = K\frac{\sqrt{ab}}{\psi_1} \tag{2.14}$$

$$\psi_1 = \sqrt{\frac{2Z_1Z_2e^2}{Ed}} \tag{2.15}$$

where E is ion energy, σ_D is dechanneling factor, K is a constant = 0.471, a is Thomas Fermi screening radius (0.142Å for iron), b is Burgers vector, and the slope value is measured from $E^{1/2}$ vs $d/dz(DP)$ plot. The ψ_1 is the critical angle of channeling, d is atomic spacing of atomic rows, Z_1 and Z_2 are atomic numbers of ion and target respectively.

2.10. FLUX7 program

One of important applications of ion channeling is to find lattice location of impurities relative to host crystal from the shape of the tilt angular scans. For that, the tilt angular scans of host atom as well as impurity atom signals are measured. By simulating the tilt angular scan of impurity by placing at various sites of host crystal and comparing with experimental tilt angular scan, lattice location of impurities can be identified with a precision of 0.1 Å. For affirmative confirmation of lattice location we performed ion channeling experiments along two different axes/planes.

For simulations of random and aligned RBS spectrum and tilt angular scans of both host atom as well as impurities, Monte Carlo program FLUX7 is used. The FLUX7 program is developed and maintained by Prof. P.J.M Smulders and co-workers [63,64]. In this simulation, both binary collision model as well as multi string potential approximations are included to correctly predict the channeling experiments. The impact parameter dependent interactions, thermal vibration of the lattice, a disordered surface layer and angular spread of the incoming beam are also included. The program follows trajectories of fast ions on their path along an axial channeling or near axial channeling direction. The depth integrated particle flux as function of *x* and *y* direction is calculated during simulation. The flux distribution along channeling/near channeling directions are weighted with impurity profile and the close encounter scattering yields of impurity atoms are calculated to find lattice location of impurity. The close-encounter yield of lattice atom, average energy loss and average energy straggling are also can be extracted as a function of depth. To obtain tilt angular scans of host as well as impurity atoms, the simulation is repeated with various tilt angles along an axis with number of ion trajectories. The host tilt angular scan is obtained by extracting close encounter probability with each tilt angle. For impurity tilt angular scan the convolution of flux distribution with impurity position distribution is used with each tilt angle. The impurity distribution could be varied and corresponding tilt angular scan can be generated. By fitting the simulated tilt angular scans with experiment the lattice location of impurities can be found.

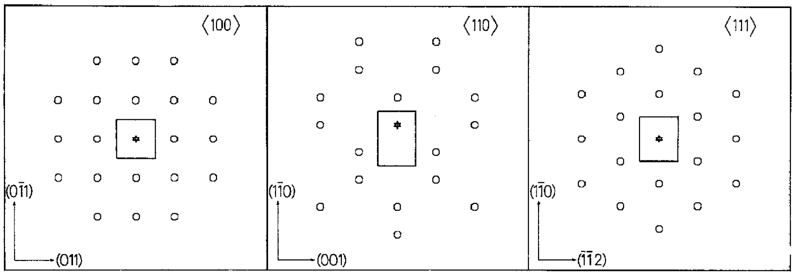

Figure 2.21 Projections of diamond lattice along <100>, <110> and <111> axis.

In FLUX7 program, the *x-y* plane perpendicular to an axis is divided into rectangular cells each containing one atom row. These unit cells can be repeated by translation or reflection to form real atomic projections in the plan. For example the projection of diamond lattice along <100>, <110> and <111> axis are shown in Fig. 2.21. The unit cell containing one atom is marked as a rectangle. In this program the atom in the unit cell will be treated by binary collision and the surrounding atomic strings are treated within multi string approximation. The force field derived from the surrounding strings is already stored in the program. The ion leaving the unit cell is put back to its equivalent position in the same unit cell to account the depth dependent channeling phenomenon. At each time the particle position and velocity are updated by taking the following factors into account:

a) A binary collision approximation is applied for the central atom and its atomic position is sampled from the thermal distribution.

b) The deflection of ions from the thermally modified continuum string potential is accounted for the surrounding atomic strings.

c) The energy loss and angular scattering due to interactions with electrons are updated at each layer.

The change in the transverse momentum in a binary collision with impact parameter *b* is given in the impulse approximation by,

$$\begin{aligned}\Delta p_{\perp}(b) &= \int_{0}^{\infty} F_{\perp}\, dt \\ &= \frac{1}{v}\int_{-\infty}^{+\infty} F_{\perp}\, dz \\ &= \frac{-1}{v}\frac{\partial}{\partial b}\int_{-\infty}^{\infty} V(\sqrt{z^2+b^2})\, dz \qquad (2.16)\end{aligned}$$

where v is velocity of ion. This approximation is valid if $E > Z_1\, Z_2$ 300 eV. The V(r) is screened coulomb potential which is expressed as,

$$V(r) = \frac{Z_1 Z_2 e^2}{r} \phi(r/a) \tag{2.17}$$

For the screening function $\phi(r/a)$, a variety of alternatives have been in use,

(a) The Moliere approximation to the Thomas-Fermi potential (TFM potential)

$$\phi(r/a) = \sum_i \alpha_i \exp(-\beta_i r/a) \tag{2.18}$$

with α_i = {0.1, 0.55, 0.3}, β_i = {6.0, 1.2, 0.3} and $a = 0.8853 a_0 (Z_1^{1/2} + Z_2^{1/2})^{-2/3}$ is Firsov's screening radius.

(b) The Lindhard screening function:

$$\phi(r/a) = 1 - \{1 + 3a^2/r^2\}^{-1/2} \tag{2.19}$$

with Bohr's screening radius $a = 0.8853 a_0 (Z_1^{2/3} + Z_2^{2/3})^{-1/2}$.

(c) The "universal potential" or "Ziegler, Biersack and Littmark – ZBL" which has same potential form as Moliere potential with 4 terms in summation:

α_i = {0.1818, 0.5099, 0.2802, 0.02817}, β_i = {3.2, 0.9423, 0.4029, 0.2106} and $a = 0.8853 a_0 / (Z_1^{0.23} + Z_2^{0.23})$.

(d) The potential derived from spherically symmetric atomic charge distribution $\rho_2(r)$, obtained from Hartee-Fock calculations. Considering the moving ion is a point charge the screening function is then,

$$\phi(r) = \frac{1}{Z_2} \left\{ \int_r^{r_{\max}} 4\pi r^2 \rho_2 dr - r \int_r^{r_{\max}} 4\pi r \rho_2 dr \right\} \tag{2.20}$$

Here ρ_2 is electrons per unit volume. The value of ρ_2 is assumed to be constant beyond half the distance between atoms and $r_{\max}$ is chosen such that the first integral is equal to Z_2 for $r = 0$. For charge distribution of moving ion is accounted with effective point charge Z_1.

In the continuum potential approximation, the potential of the individual atom is smeared out in direction parallel to the string. The atom vibration due to thermal energy is considered as Gaussian distribution around their equilibrium positions and the thermal vibration amplitude is derived from Debye model. Convolution of continuum string potential with this Gaussian distribution leads to thermally modified continuum string potential. The energy loss due to collisions of incident ion with nuclei of lattice atoms is treated by binary collision model. The energy loss due to inner electrons and valence electrons are separately accounted in the program. For the case of lattice atom yield calculations, the close encounter probability is calculated and updated in each depth interval. For the case of impurity yield, the weighted flux is calculated for the impurity depth profile and depending on the lattice location of impurities the yield is calculated. More details of FLUX7 can be found in reference [63,64].

2.11. Ion channeling – simulation details

The thermal vibrations from Debye model, crystallographic information (lattice constant of bcc Fe – 2.87Å) and ion beam details are the input parameters. In the present thesis, the ZBL potential is used for all ion channeling simulations. The lateral beam divergence of 0.01° is used for all simulations irrespective of ion species. The Debye temperature of 470 K is used for Fe, Cr host atoms and O^{18} solute which corresponds to thermal vibration amplitude of 0.08 Å, 0.09 Å and 0.1 Å respectively.

For Fe15%Cr alloy, 15% of Cr is substituted in bcc Fe lattice site (lattice constant of 2.86 Å). The depth range of host atoms and distribution of impurities are given as input in the simulations. For simulation of RBS spectrum at aligned and random directions, the experimental parameters (i) incident ion energy, (ii) scattering angle, (iii) incoming angle, (iv) out going angle, (v) detector resolution, (vi) energy per channel (keV/channel) and (vii) energy of 0^{th} channel obtained from energy calibration and (viii) last channel number obtained from experimental RBS spectrum are given as inputs. The various RBS spectra with different detector resolution are fitted with experiment and detector resolution was found to be 20 keV. From the FLUX7 simulated RBS spectrum, the channel number is converted to equivalent energy and depth which are used for measuring *DP* and range of defects in crystals.

The simulations of RBS, NRA and PIXE/channeling tilt angular curves are carried out with FLUX7 program. For simulations of NRA and PIXE tilt angular scans, the NRA cross section and PIXE cross sections are used respectively. The simulated tilt angular scans are fitted with experiment to quantitatively measure the lattice location and fraction of O^{18}/Cr. During the fitting of simulated scans with experiment, the calculated O^{18} yield is corrected for additional random fraction of incident beam [65], which is given by,

$$\chi^{corr}(\psi) = (1 - f_R)\chi^{calc}(\psi) + f_R \tag{2.21}$$

$$f_R = \frac{\chi_{Fe}^{\exp}(0) - \chi_{Fe}^{calc}(0)}{1 - \chi_{Fe}^{calc}(0)} \tag{2.22}$$

where $\chi^{corr}(\psi)$ is simulated O^{18}/Cr yield after random correction used for fitting experimental yield, $\chi^{calc}(\psi)$ is as calculated O^{18} yield, ψ -angle of incidence, f_R is the fraction of channeled beam that has become dechanneled due to host defects, $\chi_{Fe}^{\exp}(0)$, $\chi_{Fe}^{calc}(0)$ are experimental and theoretical $\chi_{\min}$ of Fe at aligned direction. All the simulations are performed for 50000 incident ions.

2.12. Slow Positron Doppler Broadening Spectroscopy

Slow positron Doppler broadening spectroscopy (SPDBS) is used to study vacancy defect in ion implanted Fe and FeCr crystals. The positron is the antiparticle of the electron. The source used in our experiment is the Na^{22} (10 μCi) radioactive nuclei which is enclosed between few μm thick Ni foil. The half life of source is 2.6 years and decays as given in Eq. (2.23).

$$ {}^{22}_{11}Na \rightarrow {}^{22}_{10}Ne + e^{+} + \gamma \tag{2.23}$$

Since the half life of e^{+} is short (3.7 ps) the emission of γ-ray (1274 keV) is considered as emission of positron due to its long half-life. When emitted positrons incident on a solid surface, most of the positrons will be implanted in to the sample and some of them will be backscattered. The implanted positrons will penetrate to solid and lose their energy until thermal equilibrium energy is reached. This is termed as thermalization process [66]. The penetration depth or implantation depth of positrons follows a probability distribution with a mean depth $\bar{z}$. The distribution of positrons or implantation profile $P(z,E_p)$ is well approximated by Makhov which is given in Eq. (2.24) [67]. A simple analytical expression for calculating mean implantation depth is also given in Eq. (2.25).

$$p(z,E) = \frac{mz^{m-1}}{z_0^{m}} \exp\left[-\left(\frac{z^{m}}{z_0}\right)\right] \tag{2.24}$$

$$z_0 = \frac{AE^{n}}{p\Gamma\left(1+\frac{1}{m}\right)}$$

$$\bar{z} = \frac{AE^{n}}{\rho}(nm) \tag{2.25}$$

widely used empirical values are m = 2, n = 1.6 and A = 4.0 μg.cm^{-2}keV^{-n}. A model representation of implanted depth profile in a material is shown in Fig. 2.22 and it shows that the mean implantation depth increases with increasing energy.

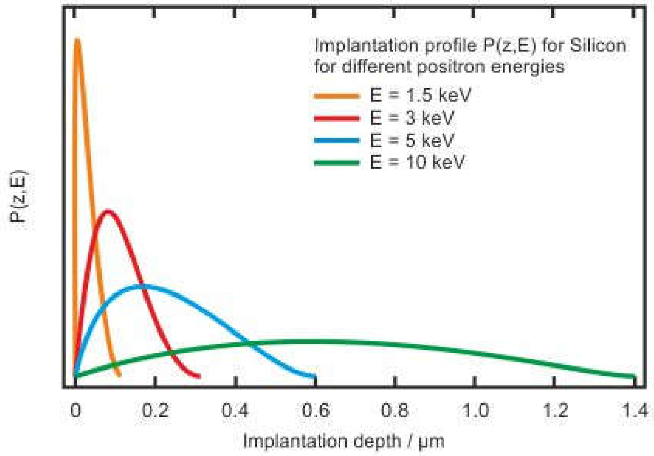

Figure 2.22 Positron implantation depth profile in a solid [68].

After thermalization, positrons start to diffuse randomly through the lattice. The positron diffusion can be approximated by a steady state one dimensional diffusion equation which is given as [67],

$$D_+ \frac{\partial^2 n}{\partial z^2} - \frac{D_+ e}{kT}\frac{\partial}{\partial z}\left(\varepsilon(z)n(z)\right) - \frac{n(z)}{\tau_1} + n_0(z) = 0 \qquad (2.26)$$

where $n(z)$ is the positron probability density, D_+ is the positron diffusion coefficient, T is the temperature, $\varepsilon(z)$ is the electric field, e is the positron charge and $n_0(z)$ is the positron stopping rate at depth z. The positron diffusion length L_+ is defined as,

$$L_+ = \sqrt{\tau_b D_+} \qquad (2.27)$$

where τ_b is life time of positron in the defect free bulk sample

The positron could be trapped in vacancy type of defects, thereby diffusion can be confined due to attractive potential caused by the missing positive charge of the atom core. The positron trapping rate k describes how fast positron is trapped to a defect d,

$$k = \mu_d C_d \qquad (2.28)$$

where μ_d is the trapping coefficient, C_d is concentration of defects

The thermalized positron annihilates with an electron with emission of dominantly two 511 keV γ-rays nearly in opposite directions. The Doppler effect is observed in the γ-rays due to the annihilating positron-electron pair acting as a moving source having momentum component in the direction of gamma rays [66]. The frequency of the photons is shifted due to Doppler effect. This causes a shift in the energy (or momentum) of the gamma rays described by $\Delta E = 1/2(p_z c)$ where p_z is the momentum parallel to the direction of annihilation gamma and c is speed of light. This Doppler broadening is the characteristic of the defect sites. In defect site, the fraction of valence electrons involved in the annihilation process increases compared with that of core electrons.

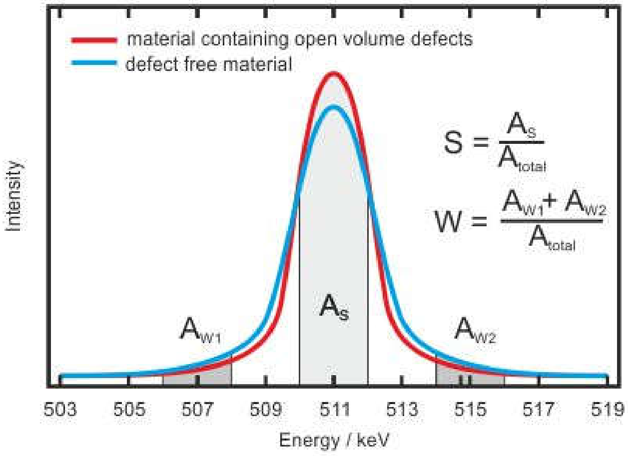

Figure 2.23 Schematic Doppler broadening spectra from a defect free crystal and in the presence of vacancies in the crystal [68].

The broadening in the annihilation peak is studied by line-shape parameters called S (shape or valence electron annihilation parameter) and W (wing or core-electron annihilation parameter) which are defined as [67],

$$S = \frac{A_S}{A_t} = \frac{\int^{511-E_S}_{511+E_S} N(E)dE}{\int N(E)dE} \tag{2.29}$$

$$W = \frac{A_w}{A_t} = \frac{\int_{511-E_{w1}}^{511-E_{w2}} N(E)dE + \int_{511+E_{w1}}^{511+E_{w2}} N(E)dE}{\int N(E)dE} \tag{2.30}$$

where E_s, E_{w1}, and E_{w2} represents shift in peak region typically ±1 keV, lower shift in wing region typically 2.5 keV and larger shift in wing region typically 5 keV respectively. *N(E)* represents the Doppler broadened spectrum and thus the denominator in each expression represents total counts in the spectrum. Fig. 2.23 shows a typical schematic diagram of Doppler broadening spectra. The *S* and *W* parameters are sensitive to the momentum distribution of valence and core electrons respectively at annihilation site. The *S* and *W* parameters are characteristic of open volume defects.

The experimental set up of SPDBS is shown in Fig. 2.24. First, 545 keV positrons are emitted from the ^{22}Na which cover penetration depth of few hundred micrometers. However in the present thesis, the low energy ion implantation technique is used to introduce defects which has range with one or two micrometer. To investigate defects in ion implanted crystals, Doppler broadening measurements have been carried out as a function of incident positron energy *E* from 0.5 keV to 22 keV. To achieve this requirements, the energy of emitted positron is moderated to low energy by using well annealed (2473 K to avoid trapping site and improve surface quality) W (100) single crystal of thickness < 1µm which is having efficiency in order of 10^{-5} (*i.e.* 1 in 10^5 positrons get moderated). The fraction of thermalized positron reaching surface of W(100) will be emitted with energy equal to the negative work function of W (2.8 eV) [69]. These low energy positrons are transported electrostatically into the transport region which also contains the velocity filter. The filter can be a magnetic bend or electric field – magnetic field transverse combination (*E*×*B* filter) which allows only positrons of specific energy to cross the filter [70]. The slow monoenergetic positrons are separated from un-moderated fast positrons by transport through 180° U-bend magnetic solenoid tube and slow positrons are allowed to reach the target. The filtered positrons are accelerated to the required energy by applying high voltage, varying from 0.5 keV to 22 keV to implant them to different depths. The gamma ray spectrum is recorded using high purity Germanium (HpGe) detector having energy resolution of 1.40 keV at 662 keV gamma line of Cs-137 [71]. The analysis of *S* and *W* parameter with function of controlled positron energy provides a powerful approach to interpret the depth profiling of vacancy defects in ion implanted crystals.

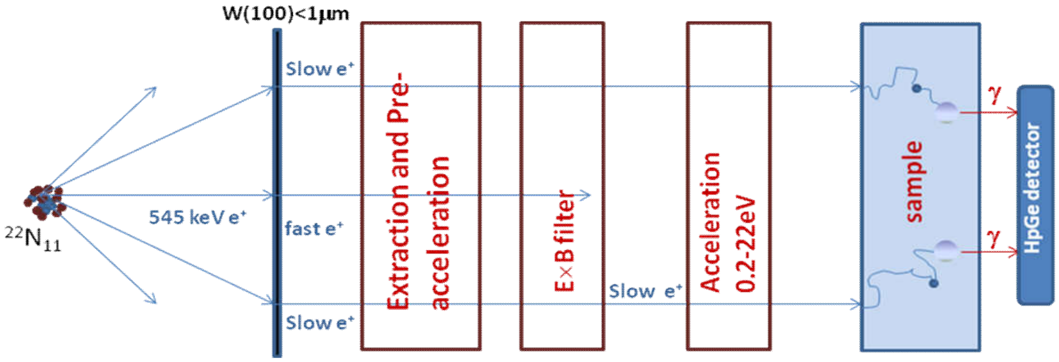

Figure 2.24 Experimental set up of slow positron Doppler broadening spectroscopy (SPDBS).

The experimentally observed *S* parameter at a positron energy *E* can be approximately written as,

$$S = f_b S_b + f_s S_s + f_d S_d \tag{2.31}$$

where f_s, f_b, f_d represents fraction of positron annihilating in surface, bulk, and defected layers respectively and S_s, S_b, S_d represents *S* parameter of surface, bulk, and defected layers respectively. Here, layer is referred to the depth from the surface. VEPFIT code [72] is used to fit the experimental *S* vs. *E* data which gives the fraction of positrons annihilating in various trapping centres as a function of depth in the sample. In VEPFIT code, the positron diffusion equation is taken into account with positron diffusion, trapping and annihilation in the sample. The diffusion length of positron is reduced due to trapping at defect sites. The *S* parameter is increased due to the presence of open volume defects. The *S(E)* is fitted by varying *S* parameter of sample and average diffusion length of positrons with different layers from surface by VEPFIT code. From the fitting, the *S* parameters and diffusion lengths of modeled layers are obtained. This diffusion lengths and *S* parameters are used to calculate the vacancy concentrations at each layer of sample.

2.13. Density functional theory – basics

Density functional theory is a quantum mechanical tool which is mainly used to investigate the electronic structure of many-body systems, in particular molecules and the condensed phases [73-75]. DFT is one of the most popular and versatile methods available in computational condensed matter physics and computational chemistry. Conventional methods in electronic band structure theory, in particular Hartree-Fock theory and its descendants, are mainly based on the complicated many-electron wave function. The prime objective of density functional theory is to replace the many-body electronic wave function with the electronic density as the basic quantity. The many-body wave function is dependent on $3N$ variables, three spatial variables for each of the N electrons. But, the density is only a function of three variables and is a simpler quantity to deal with both conceptually and practically.

Density functional theory has its conceptual roots in the Thomas-Fermi model and it was not put on a firm theoretical footing until the Hohenberg-Kohn (HK) theorems. The first theorem demonstrates the existence of a one-to-one mapping between the ground state electron density and the ground state wave function of a many-particle system. Further, the second HK theorem proves that the ground state density minimizes the total electronic energy of the system. The original HK theorems held only for the ground state in the absence of magnetic field, although they have since been generalized. The first Hohenberg-Kohn theorem is only an existence theorem, stating that the mapping exists, but does not provide any such exact mapping.

The most common implementation of density functional theory is through the Kohn-Sham (KS) method. Within the framework of Kohn-Sham DFT, the intractable many-body problem of interacting electrons in a static external potential is reduced to a tractable problem of non-interacting electrons moving in an effective potential. The effective potential includes the external potential and the effects of the Coulomb interactions between the electrons, *e.g.* the exchange and correlation interactions. Modeling the latter two interactions becomes the difficulty within KS DFT.

<u>The Thomas-Fermi model</u>: The predecessor to density functional theory [73-75] was the Thomas-Fermi model, developed by Thomas and Fermi in 1927. They calculated the energy of an atom by representing its kinetic energy as a functional of the electron density, combining this with the classical expressions for the nuclear-electron and electron-electron interactions. Although this was an important first step, the Thomas-Fermi equation's accuracy was limited because it did not attempt to represent the exchange energy of an atom predicted by Hartree-Fock theory. Later, exchange energy functional was added by Dirac in 1928. However, the Thomas-Fermi-Dirac theory remained rather inaccurate for most applications. The largest source of error was in the representation of the kinetic energy, followed by the errors in the exchange energy due to the complete neglecting of electron correlation.

<u>Derivation and formalism:</u> The ultimate goal of most approaches in solid state physics and quantum chemistry is the solution of the time-independent, non-relativistic Schrodinger equation,

$$H\psi_i\left(\vec{x}_1,\vec{x}_2,......\vec{x}_N;\vec{R}_1,\vec{R}_2,......\vec{R}_M\right)=E_i\psi_i\left(\vec{x}_1,\vec{x}_2,......\vec{x}_N;\vec{R}_1,\vec{R}_2,......\vec{R}_M\right) \qquad (2.32)$$

where H is the Hamiltonian for a system consisting of M nuclei and N electrons. So, the Hamiltonian can be written into five terms *i.e.*

$$H = -\sum_{e}\frac{\hbar^2}{2m_e}\Delta r_e - \sum_{i}\frac{\hbar^2}{2m_i}\Delta r_i + \frac{1}{2}\sum_{e\neq e'}\frac{e^2}{\left|r_e - r_e^{'}\right|} + \frac{e^2}{2}\sum_{i\neq i'}\frac{Z_i Z_i^{'}}{\left|r_i - r_i^{'}\right|} + \frac{e^2}{2}\sum_{e,i}\frac{Z_i}{\left|r_e - r_i\right|} \tag{2.33}$$

Here the first two terms describe the kinetic energy of the electrons and nuclei. The other three terms represent the repulsive potential due to the electron-electron and nucleus-nucleus interactions and attractive electrostatic interaction between the nuclei and the electrons. It is not possible to separate Hamiltonian into electron and ion problem. Nuclei move much slower than the electrons due to their masses and one can consider that electrons are moving in the field of fixed nuclei (Born-Oppenheimer approximation). So, the nuclear kinetic energy is zero and their potential energy is nearly a constant. Thus, the electronic Hamiltonian reduces to,

$$H = -\sum_{e}\frac{\hbar^2}{2m_e}\Delta r_e + \frac{1}{2}\sum_{e\neq e'}\frac{e^2}{\left|r_e - r_e^{'}\right|} + V_{ext} \tag{2.34}$$

According to Hohenberg-Kohn theorems [76], Hamiltonian of the system and universal function F_{HK} of energy can be determined from ground-state electron density. Using this Hamiltonian, one can determine everything of the system. Based on the universal function, the total energy of system of interacting electrons can be expressed for arbitrary external potential as follows:

$$E[n(r)] = T[n(r)] + V_{\text{int}}[n(r)] + \int dr V_{ext}(r) n(r) \tag{2.35}$$

$$E[n(r)] = F_{HK} + \int dr V_{ext}(r) n(r) \tag{2.36}$$

where $F_{HK} = T[n(r)] + V_{\text{int}}[n(r)]$

However, for multi electron problem, this functional is completely mysterious. To keep away from this ambiguity, one can use Kohn and Sham approach [77]. This approach defines fictitious non-interacting system with the same electron density as the true interacting system, but with different external potential. The orbitals of the non-interacting system are called Kohn-Sham orbitals [77] which must be orthonormal and lead to same electron density. Universal functional as a functional of single Slater determinant of Kohn-Sham orbitals are given below:

$$F_{HK}[n] = T[n] + V_{ee}[n] \tag{2.37}$$

$$F_{HK}[n] = T_s[n] + T_r[n] + V_{ee}[n] \tag{2.38}$$

Here T_s is the kinetic energy of the non-interacting system and T_r is the difference between kinetic energy of interacting and non-interacting system. Kinetic energy of non-interacting term T_s expressed in terms of Kohn-Sham orbitals as follows,

$$T_s[n] = T_s[\psi_i[n]] \tag{2.39}$$

$$T_s[n] = -\frac{1}{2}\sum_i \left\langle \psi_i \middle| \nabla^2 \middle| \psi_i \right\rangle \tag{2.40}$$

the potential part V_{ee} can be also separated into classical J and non-classical part V_{nc},

$$V_{ee}[n] = J[n] + V_{nc} \tag{2.41}$$

The classical Hartree energy $J[n]$ can be written through Kohn-Sham orbitals as follows:

$$J[\{\psi_i\}] = -\frac{e^2}{2}\int dr_1 \int dr_2 \frac{\psi_i^*(r_1)\psi_i^*(r_2)\psi_i(r_1)\psi_i(r_2)}{|r_1 - r_2|} \tag{2.42}$$

So the functional of energy is expressed as follows,

$$E[n] = T_s[n] + J[n] + T_r[n] + V_{nc} + \int dr V_{ext}(r) n(r) \tag{2.43}$$

The addition of term $T_r[n]$ and term V_{nc} is E_{xc} which called as exchange –correlation term. This term, E_{xc}, contains hidden many difficult and unpleasant things. Due to this reason, to get the solution of the above said Eq. (2.43) will be very tough, so it can only be approximated. The term E_{xc} is as follows,

$$E_{XC} = T_r[n] + V_{nc} \tag{2.44}$$

Using the variational principle, under the constraint of orthonormality of KS orbitals, the functional $E[n]$ is written as,

$$\frac{1}{\delta\psi_i}\delta\left[E[n] - \sum_{i,j} e_{i,j}\langle \psi_i \| \psi_i \rangle\right] = 0 \tag{2.45}$$

By solving Eq. (2.45),

$$\frac{\delta T_s}{\delta\psi}+\left[\frac{\delta J}{\delta n}+\frac{\delta E_{XC}}{\delta n}+\frac{\delta\int drV_{ext}(r)n(r)}{\delta n}\right]\frac{\delta n}{\delta\psi}=\frac{\delta\sum_{i,j}e_{i,j}\langle\psi_i\|\psi_i\rangle}{\delta\psi} \tag{2.46}$$

So instead of solving electron problem with Schrödinger Eq. (2.35), one can solve effective Kohn-Sham equations:

$$H_{KS}\psi_i(r_i)=\sum_{i,j}e_{i,j}\psi_i(r_i) \tag{2.47}$$

Here H_{KS} is,

$$H_{KS}=-\frac{1}{2}\nabla^2+V_s(r_i) \tag{2.48}$$

where,

$$V_s(r_i)=V_H(r_i)+V_{XC}(r_i)+V_{ext}(r_i) \tag{2.49}$$

Finally, electron density is simply expressed by,

$$n(r)=\sum_i\int_\sigma g_i|\psi_i(r_\sigma)|^2 \tag{2.50}$$

Here g_i is occupational numbers and integral over σ means sum over spin. Kohn-Shan self-consistent equations (Eq. (2.47)) are solved iteratively by following scheme (Fig. 2.25):

Initial guess is a random trial electron density,

(a) Solve the effective potential V_s, Eq. (2.49)

(b) Solve Kohn-Sham equation, Eq. (2.47)

(c) Calculate new electron density

(d) Repeat until electron density convergence

(e) Finally calculate the properties using optimized parameters

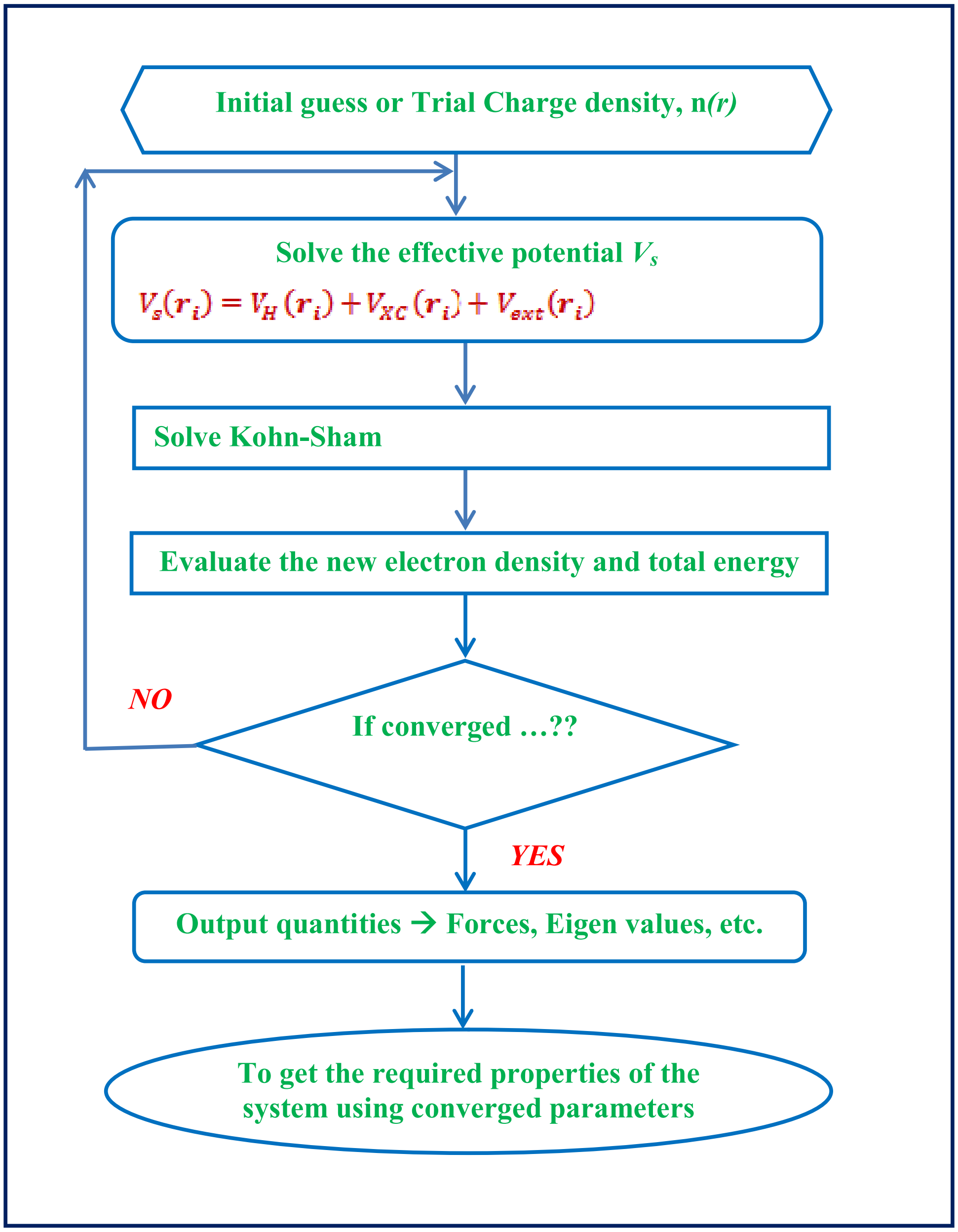

Figure 2.25 Flow chart of density functional theory calculations.

<u>Approximations:</u> The major problem with DFT is that the exact functional for exchange and correlation are not known except for the free electron gas. However, approximations exist, which permit the calculation of certain physical quantities quite accurately. The simplest approximation is the local-density approximation (LDA), which is based upon exact exchange energy for a uniform electron gas, which can be obtained from the Thomas-Fermi

model, and from fits to the correlation energy for a uniform electron gas. In physics, the most widely used approximation is the local-density approximation (LDA), where the functional depends only on the density at the coordinate and the functional is evaluated as,

$$E_{XC}[n]=\int \in_{XC}(n)n(r)d^3r \tag{2.51}$$

The local spin-density approximation (LSDA) is a straightforward generalization of the LDA to include electron spin:

$$E_{XC}[n_\uparrow,n_\downarrow]=\int \in_{XC}(n_\uparrow,n_\downarrow)d^3r \tag{2.52}$$

Highly accurate formulae for the exchange-correlation energy density $\in_{XC}(n_\uparrow, n_\downarrow)$ have been constructed from Quantum Monte Carlo simulations of a free-electron gas. Even though generalized gradient approximations (GGA) are still local, however it also takes into account the gradient of the density at the same coordinate:

$$E_{XC}[n_\uparrow,n_\downarrow]=\int \in_{XC}(n_\uparrow,n_\downarrow,\vec{\nabla}n_\uparrow,\vec{\nabla}n_\downarrow)d^3r \tag{2.53}$$

GGA gives very good results for molecular geometries and ground state energies compared to LDA. In the present work, to study the total ground state energy of Fe, the generalized gradient approximation (GGA) is chosen.

<u>PAW pseudo-potentials:</u> There are various types of pseudo-potentials (PPs) available such as norm-conserving PPs, ultrasoft PPs, and projector-augmented wave PPs. In the present work, the PAW potentials are used and these potentials are briefly mentioned below. PAW potential was first proposed by Bloch (1994), later it was adopted by Kresse and Joubert (1999). Aim of these pseudo-potentials is to predict the all electron potential with good accuracy in the valence electron contribution. The wave function of PAW potential is written in the following form,

$$\psi_{PAW}=\psi_{\text{int}er}+\psi_{pcore}+\psi_{net} \tag{2.54}$$

Here, the $\psi_{\text{int}er}$, the valence part is represented with the PW expansion, while the ψ_{pcore}, core part is projected on a radial grid at the atom center. After the additive augmentation of these two terms, the overlapping part ψ_{net} is trimmed off to make the final wave function ψ_{PAW} which is very close to the all electron wave function. Owing to the use of ψ_{pcore}, the core part is well reproduced, and many PWs become unnecessary. Thus, the PAW potential calculates results as accurate as the all electron full potential approach with much less computational effort. One of the main advantages is that this method returns the all electron charge density of valence orbitals which cannot be obtained by other standard potentials.

2.14. Density functional theory – computational details

For understanding the experimental results, DFT calculations are carried out for finding solute lattice locations in the presence of defect structures in bcc Fe matrix. To carry out the calculations in bcc Fe, the Vienna *ab-initio* simulation package (VASP) is used and it is a code that implements the DFT using pseudopotentials [76-78]. Projected augmented wave (PAW) approach [79] is used for all calculations. Spin-polarized approach and the generalized gradient approximation GGA-PBE are used to describe the exchange and correlation effects. The cutoff energy in the plane-wave basis set is 500 eV which is arrived after performing the required convergence tests. Following the Monkhorst-pack scheme [80], Brillouin zone integration is carried at 3×3×3 *k* point grids. A tolerance of 10^{-6} eV in the total energy is used for the self-consistency criteria. For all defect studies, constant volume (*CV*) (only ion positions are relaxed in a fixed equilibrium volume) calculations are performed with 128±defects atom cell. In some defect structures, zero pressure (*ZP*) (both ion positions and volume of cell is relaxed) calculations are also performed.

The incremental binding energy of defect complex is defined as [81],

$$E_b^{a,b} = E(defect-a) + E(defect-b) - E(defect-(a+b)) - E_{Fe} \tag{2.55}$$

Where $E(defect-a)$, $E(defect-b)$, $E(defect-(a+b))$ and E_{Fe} are energy of cell containing defect-a, defect-b, both defect-a and defect-b and defect free lattice respectively.

In all the discussions positive binding energy indicates energy lowering attraction of defects.

2.15. Conclusion

In this chapter, the experimental techniques based on ion beam analysis (RBS, NRA, PIXE and ion channeling), SPDBS and theoretical technique (DFT calculations) have been discussed. These techniques are used in this thesis to study solute-defect interactions. The experimental and DFT results are given in forth coming working chapters.

Chapter 3

Interaction of oxygen with interstitial defects in bcc Fe

The interaction of oxygen with vacancy defects is widely studied in the literature by simulations [51] as well as experiments [42]. But interaction of O with self interstitial defect in Fe is rarely reported in the literature. However both self interstitial and vacancy defects are formed in metals, during radiation damage produced by neutron or ion, can also interact with O. Olson *et al*. studied (by DFT calculations) the interaction of O with <110> dumbbell self interstitial defect by placing O at various octahedral sites, from short to long distance [82]. The authors found that the O interaction is repulsive with short distances and have small interactions (binding energy ~0.1 eV) at long distances. This suggests that O could interact with self interstitial defects also. In experiments, the observable effect of radiation damage is the formation of dislocation loops which can form either in cascade itself or during thermal migration. At present, the interactions of O with self interstitial clusters like interstitial dislocation loops are not understood well. Aim of this chapter is to understand the oxygen interaction with interstitial defects and defect structure of O-defect clusters formed in the presence of excess interstitial defects in bcc Fe. First, O^{18} ions are implanted into Fe(110) crystal. Lattice location of O^{18} is measured. Excess interstitial defects are introduced by self ion implantation at the implanted depth of O^{18}. The lattice site location of O^{18} is examined again. The O-SIA interactions and defect structure is studied by combining DFT, dechanneling measurements and SPDBS measurements.

3.1. Introduction of O^{18} and interstitial defects by ion implantation

First, a bcc Fe(110) crystal with a chemical purity of 99.98% is implanted with 300 keV O^{18} ions at a fluence of 5×10^{15} ions/cm^2 at room temperature followed by *in-situ* annealed in the vacuum of 2×10^{-7} mbar at 400 °C for 30 minutes. The annealing is restricted to 400 °C. Higher temperature annealing leads to loss of implanted O^{18} due to diffusion towards surface.

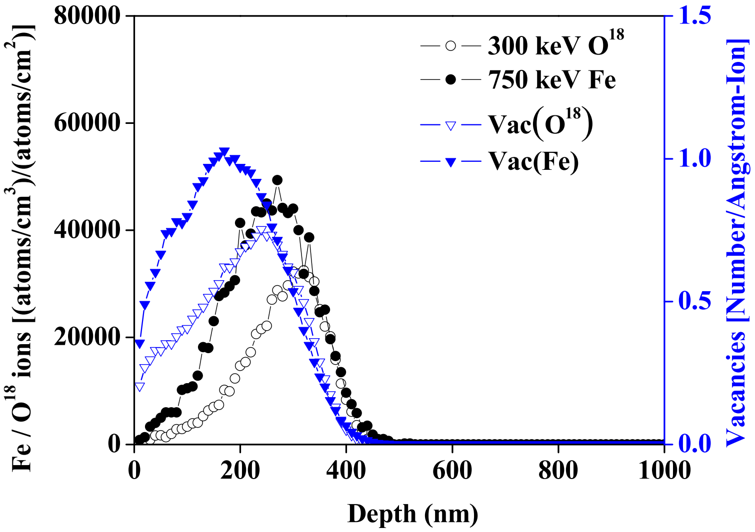

Figure 3.1 SRIM calculated range of ions and vacancies in Fe crystal produced by 750 keV Fe ions and 300 keV O^{18} ions.

The projected range and straggling of 300 keV O^{18} ions in Fe is 275 nm and 78 nm respectively, which are obtained from SRIM [54]. For the ion fluence of 5×10^{15} ions/cm^2, the O^{18} concentration is about 0.2% at peak position of O^{18} profile. The O^{18} ion implantation produces interstitial and vacancy defects also. The simulated ion and vacancy profiles (from SRIM) of 300 keV O^+ ions in Fe are shown in Fig. 3.1. The estimated peak damage from SRIM calculation is 3.5 dpa. Formation of dislocation loops is reported at this damage level in the literature [28,29]. It is also pointed that the dislocation loops could be formed during radiation damage cascade itself. The dislocation loop could be either vacancy or interstitial type. Both interstitial and vacancy type dislocation loops could coexist at same depth. The interstitial defects could be formed at higher depth than the vacancy defects. During O^{18} ion implantation, interstitial defect concentration will be high at O^{18} depth which makes more possibility of O^{18} to interact with self interstitial defects in this experiment. With the aim of introducing excess interstitials to overlap with oxygen depth profile, 750 keV Fe^+ ions with a projected range of 266 nm are introduced by subsequent implantation in Fe(110) with the ion fluence of 1×10^{16} ions/cm^2 and annealed *in-situ* at 400 °C for 30 minutes. Total damage produced by 300 keV O^{18} and 750 keV Fe at O^{18} depth is 10.5 dpa after self ion implantation. Here after the sample is denoted as *Fe1(O^{18})* and *Fe1(O^{18}+Fe@R_p)*. The O^{18} and Fe@R_p in the bracket represent O^{18} ion implantation and Fe^+ ion implantation at R_p of O^{18} respectively.

3.2. Range of defects by RBS/channeling

In presence of defects, the RBS spectrum taken in aligned direction should show increase in the backscattering yield at the depth where defects are present. To check the defect depth, RBS and channeling measurements are carried out in *Fe1(O^{18}+Fe@R_p)* sample. Figure 3.2 (a) shows the 2 MeV He^+ RBS spectra after depth conversion using the FLUX7 program from pristine Fe(110) and *Fe1(O^{18}+Fe@R_p)* along random and aligned directions. The random and channeling spectra for ideal Fe(110) crystal, simulated using FLUX7, are also shown in Fig. 3.2 (a). The value $\chi_{min} = Y_{aligned} / Y_{random}$ taken at near surface region of RBS scan is the measure of crystalline quality. For an ideal Fe crystal, it has to be 1.3% along <100> and 1.83% along <110>. The measured χ_{min} at 50 nm depth is 7% of the virgin sample; it increased to 11% after the implantation of O^{18} and Fe ions and post annealing, which indicates that defects are not annealed out completely. Similar RBS spectra taken with 3.5 MeV He^{2+} ions are also shown in Fig. 3.2 (b). A clear dechanneling step is seen from 200-500 nm depth due to the presence of defects.

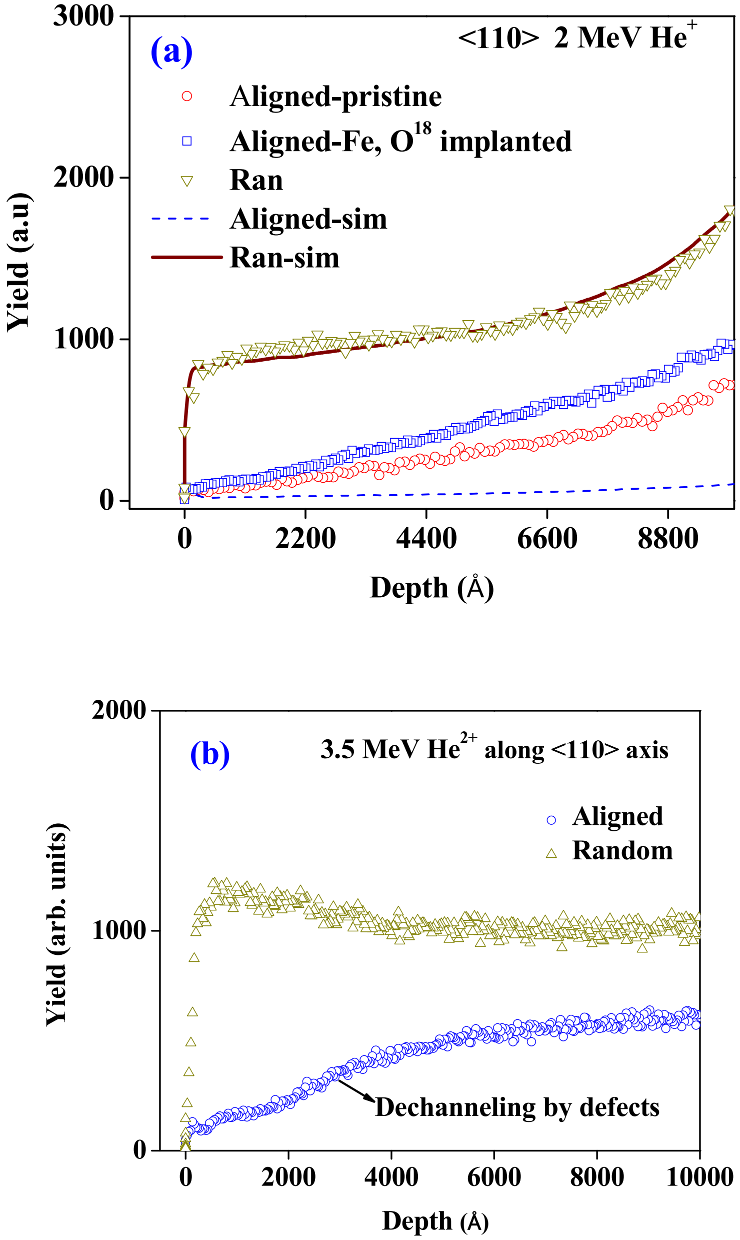

Figure 3.2 (a) RBS spectra taken with 2 MeV He^+ ions in pristine Fe(110) and *Fe1(O^{18}+Fe@R_p)* along random and <110> orientations, together with FLUX7-simulated random spectrum and <110> channeling spectrum for ideal Fe(110). (b) RBS spectra taken with 3.5 MeV He^{2+} ions along random and <110> axis.

3.3. Type of defects by energy dependant dechanneling measurement

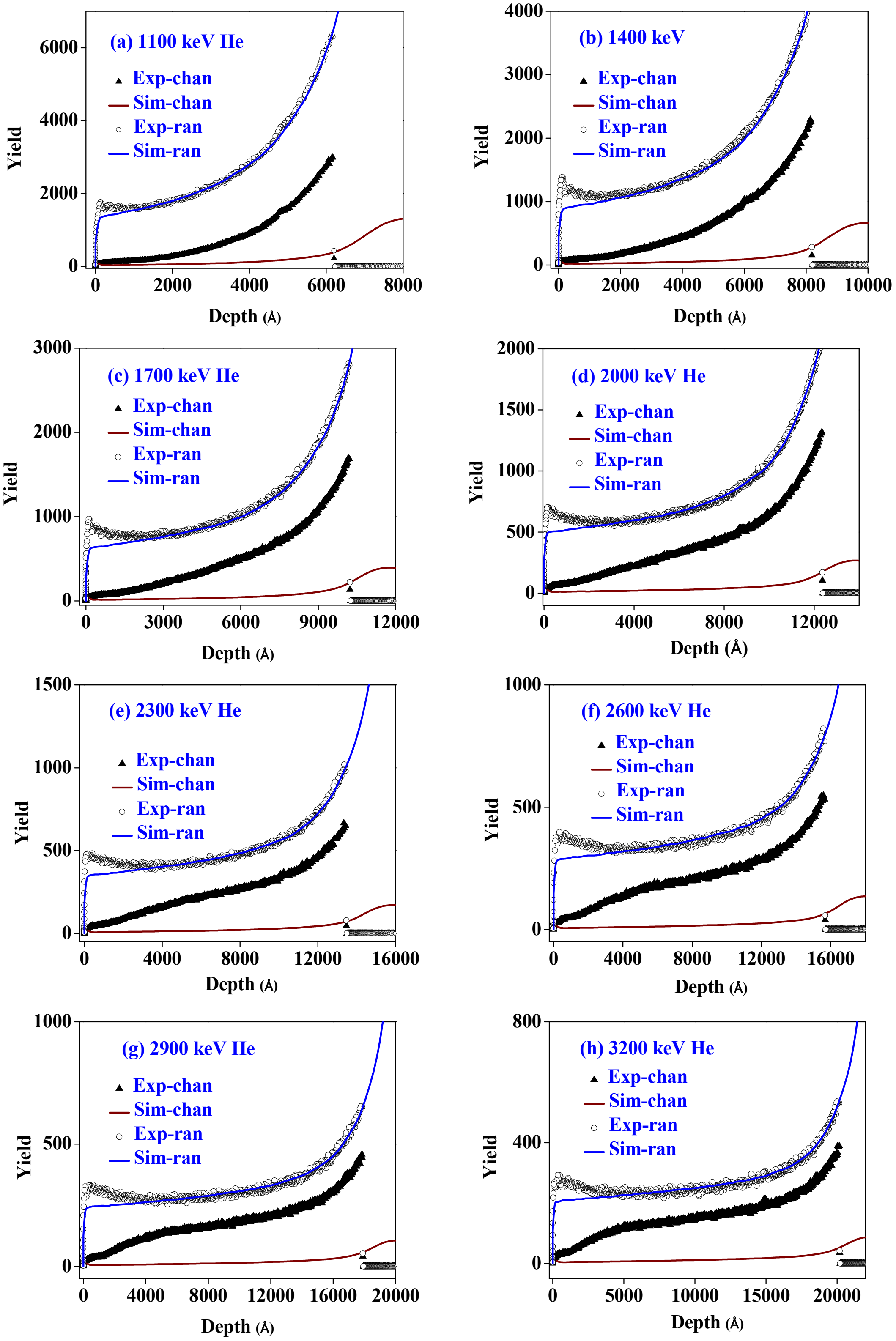

Figure 3.3 Experimental and simulated RBS spectra at <110> axial direction and random direction of $Fe1(O^{18}+Fe@R_p)$ taken with He$^+$/He^{++} ions with the energy ranging from (a) 1100 keV to (h) 3200 keV.

The energy dependence of dechanneling parameter is measured to investigate the type of defects formed at the O^{18} and self ion implanted depth. For this, RBS spectra are taken with He^{+}/He^{++} ions with the energy ranging from 1100 keV to 3500 keV along the normal axis (<110>). Random and aligned RBS spectra are simulated using FLUX7 program for all incident energies and are converted to corresponding spectra to yield *vs* depth, from which variation of χ_{min} with depth for pristine (χ_V) and ion implanted (χ_D) samples are obtained. The depth converted experimental and simulated RBS spectra at <110> axis aligned and random direction of Fe(110) crystal are shown in Fig. 3.3 for He^{+}/He^{++} ion energies from 1100 keV to 3200 keV in steps of 300 keV.

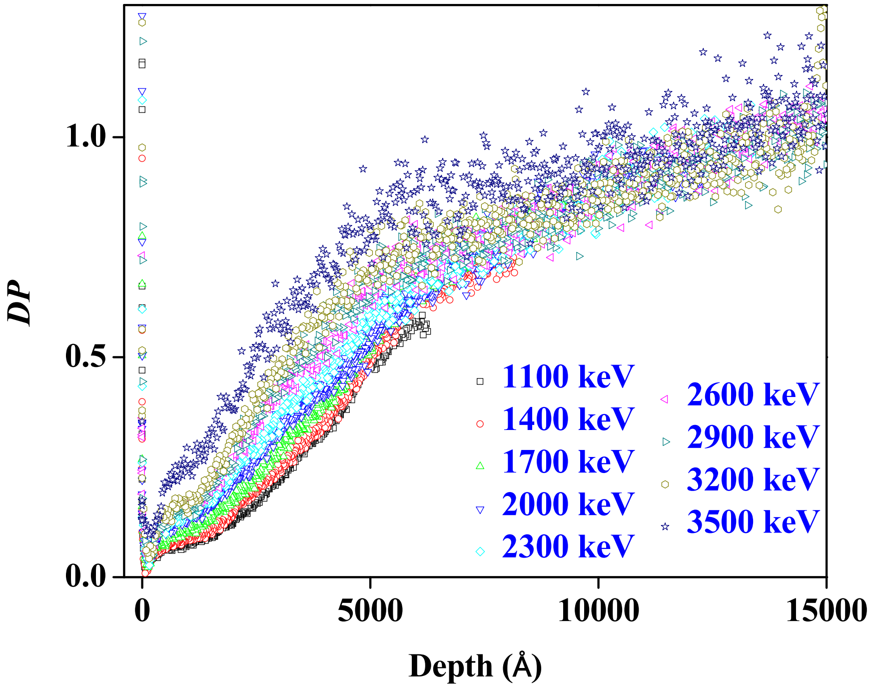

Figure 3.4 The depth resolved *DP* with different He^{+}/He^{++} ion energies from 1100 keV to 3500 keV in $Fe1(O^{18}+Fe@R_p)$ along normal axis.

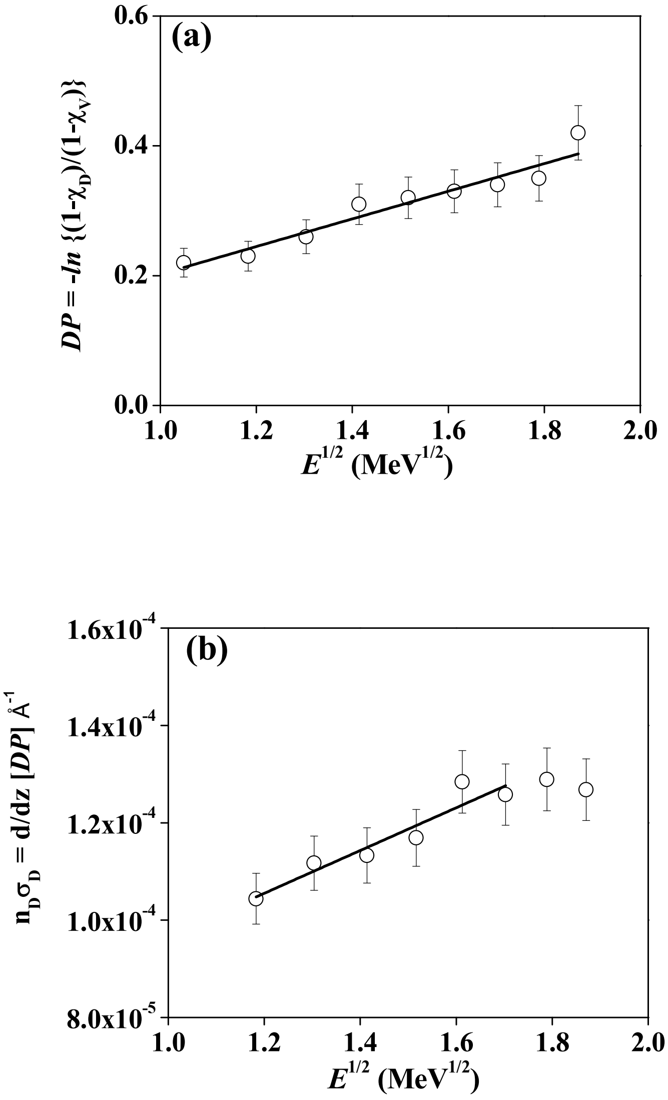

Figure 3.5 (a) Energy dependence of dechanneling parameter (*DP*) measured along normal axis around the depth of 250-300 nm. (b) Energy dependence of dechanneling parameter per unit length measured from 200 nm to 400 nm of *Fe1(*O^{18}*+Fe@*R_p*)*.

The type of defects at a particular depth can be determined by energy dependence of the dechanneling parameter (*DP*) which is given by Eq. (2.10) in section 2.9 of chapter 2. The calculated *DP* up to the probing depth of helium ions with various incident energies are shown in Fig. 3.4. The increase of dechanneling parameter is evident from 100 nm to 500 nm in Fig. 3.4. With linear fitting of experimental *DP* data shown in Fig. 3.4, around O^{18} ion implanted depth, the value of *d(DP)/dz* is obtained.

Figure 3.5 (a) shows the He ion energy dependence of dechanneling parameter (*DP*) along the normal axis of $Fe1(O^{18}+Fe@R_p)$ at the implantation depth 250-300 nm. The point defects, stacking faults and dislocations show energy dependence of $E^{-0.5}$, E^0 and $E^{0.5}$ respectively [52]. The linear fit of experimental data points (*DP*) shows $E^{0.5}$ dependence which confirms the presence of dislocations. The dechanneling parameter per unit length in the depth range of 200-400 nm (O^{18} ion range is 275±78 nm) versus $E^{0.5}$ is plotted in Fig. 3.5 (b). It shows linear dependence with $E^{0.5}$, indicating the presence of dislocation loops. The dechanneling parameter per unit length increases linearly up to transition energy (E_s) and becomes constant at higher energies. From transition energy (E_s), mean dislocation loop radius (R) can be determined using Kudo's analysis [62] from the relation $E_s = aR^2$, where a is Thomas-Fermi screening distance (0.142 Å). The measured transition energy E_S is 2900 keV. If one assumes the dislocation loops as ½ <111> loops, the obtained mean radius from Kudo's analysis is 20 nm. If the dislocation loops are <100> loops, the mean radius is 40 nm. The defect density of dislocation loops is calculated from the slope of linear fitting to *d(DP)/dz* data points (Fig. 3.5 (b)) using Eq. (2.13). The value of ψ_1 is calculated by using Eq. (2.15), for 2 MeV He^+ ions in bcc Fe crystal. The ψ_1 value is 0.77° for <110> axis. The Burgers vector of <100> loop is 2.87 Å and Burgers vector for ½ <111> loop is 1.43 Å in bcc Fe. However, the present sample may have <111> and <100> loops. The calculated dechanneling factor σ_D is 22 Å for <100> dislocation loops and 16 Å for ½ <111> dislocation loops which are calculated using Eq. (2.14). The observed defect density is 2.8×10^{10} dislocation loops/cm^2 for the case of <100> loops and 4×10^{10} dislocation loops/cm^2 for the case of ½ <111> loops.

3.4. Lattice location of O^{18} in ion implanted Fe(110)

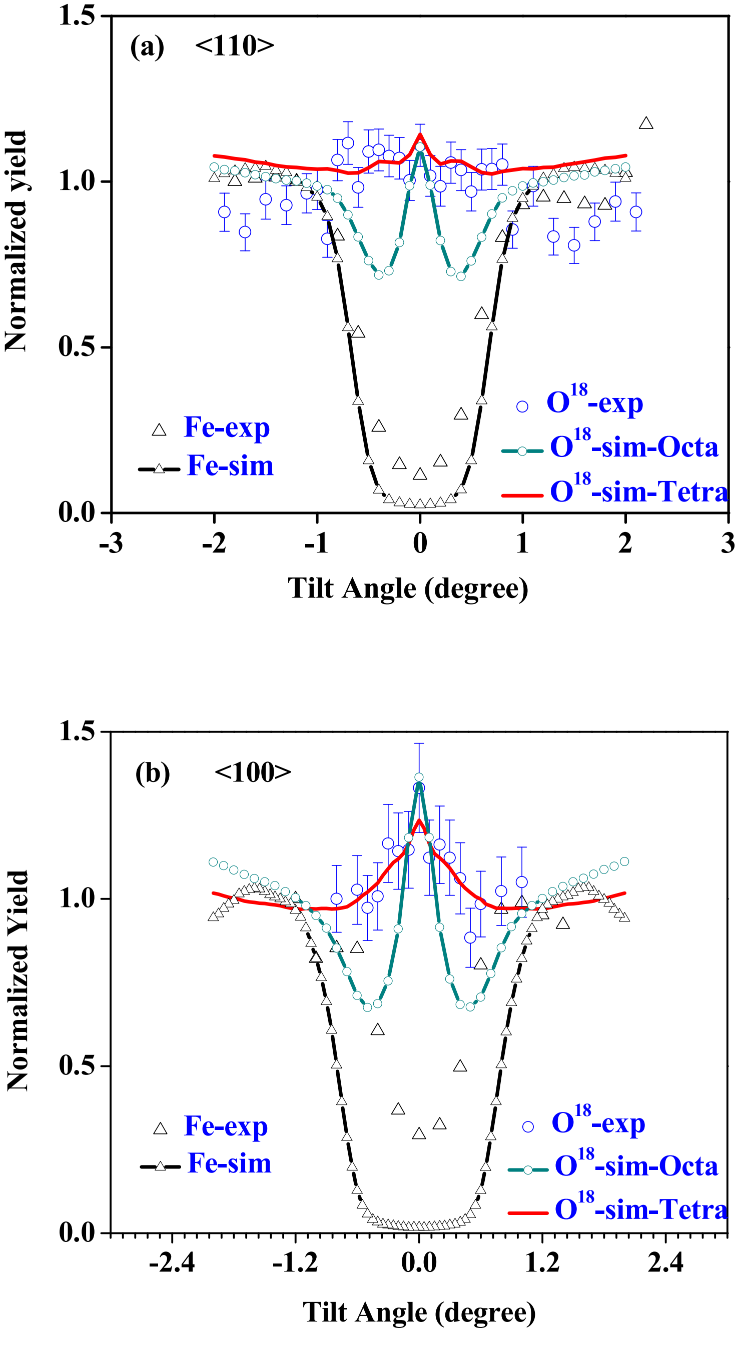

Figure 3.6 Experimental and simulated Fe and O^{18} tilt angular scans of *Fe1(O^{18})* (a) along <110> axis (b) along <100> axis.

To find the lattice location of O^{18} atom in *Fe1(O^{18})* sample, RBS and NRA spectra are obtained around the <110> and <100> axes. From this, tilt angular scans of Fe and O^{18} yield are plotted. Figure 3.6 (a) and 3.6 (b) show the tilt angular scans of proton RBS yield of Fe and NRA yield of O^{18} around <110> and <100> axes respectively. The Fe signal shows a dip while O^{18} signal shows a peak. Experimental χ_{min} from Fe tilt angular scan is 0.12 and 0.3 along <110> and <100> respectively. The width (FWHM) of the experimental scan along <110> axis is 0.6° which is comparable to the simulated value of 0.67°.

The observed peak of NRA signal at aligned angle is due to the presence of O^{18} at interstitial site, as the channeled ion flux density is high around interstitial position compared to near atomic rows in aligned angle (0 tilt angle). Same way the NRA scan around <100> axis also shows a peak at aligned angle, indicating the O^{18} is at interstitial position. In addition to the peak at the middle of the scan, tiny features on either side of the peak are observed in <110> tilt angular scans of O^{18}. In bcc system, there are two high symmetry interstitial sites (i) octahedral interstitial site and (ii) tetrahedral interstitial site which are shown in Fig. 3.7.

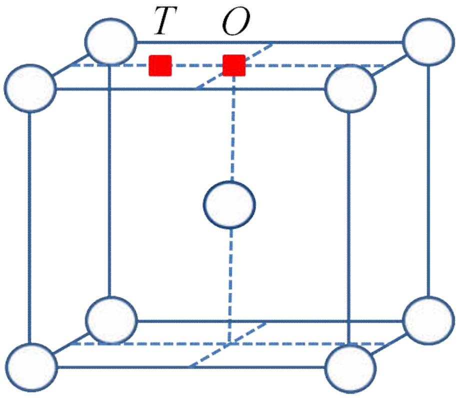

Figure 3.7 Octahedral (*O*) and tetrahedral (*T*) interstitial position in bcc Fe.

To identify the lattice location of O^{18}, tilt angular scans with O^{18} at tetrahedral and octahedral interstitial site are simulated using FLUX7 and are shown as lines in Fig. 3.6 (a) and 3.6 (b). The atomic projections of Fe and O^{18} and their multiplicity for the case of O^{18} at octahedral as well as tetrahedral along <100> and <110> axes, which are given as inputs in the FLUX7 program, are shown in Fig. 3.8. In the simulation, the random fraction (f_R) due to the dechanneling of ions from Fe matrix is also taken into account as in Eq. (2.21). The calculated f_R using Eq. (2.22) is 0.1 and 0.28 for <110> and <100> axes respectively. The good fits for both <100> and <110> axial scans are obtained within error bar of NRA yield for the case of O^{18} at tetrahedral interstitial position. No additional random is added for O^{18} yield.

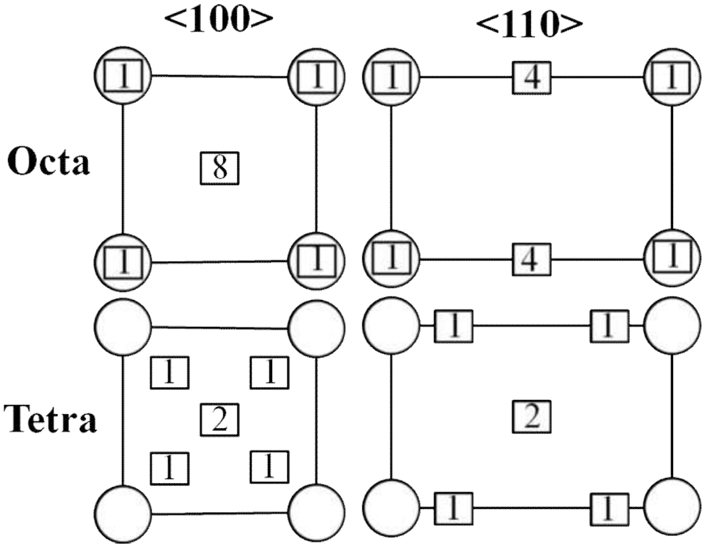

Figure 3.8 Projections of O^{18} (square) at tetrahedral and octahedral interstitial site along <100> and <110> axes of bcc Fe. Circle represent Fe atom.

3.5. Lattice location of O^{18} in O^{18} and self ion implanted Fe(110)

To check the stability of O^{18} at tetrahedral interstitial site, tilt angular scans of O^{18} and Fe signals are measured in *Fe1*(O^{18}+*Fe@*R_p) sample. The experimental and simulated tilt angular scans of Fe and O^{18} yield along <110> and <100> axes of *Fe1*(O^{18}+*Fe@*R_p) are presented in Fig. 3.9 (a) and 3.9 (b) respectively. Experimental χ_{min} of Fe tilt angular scan is 0.13 and 0.3 along <110> and <100> respectively. The width (FWHM) of the experimental scan along <110> axis is 0.6° which is comparable to the simulated value of 0.67°.

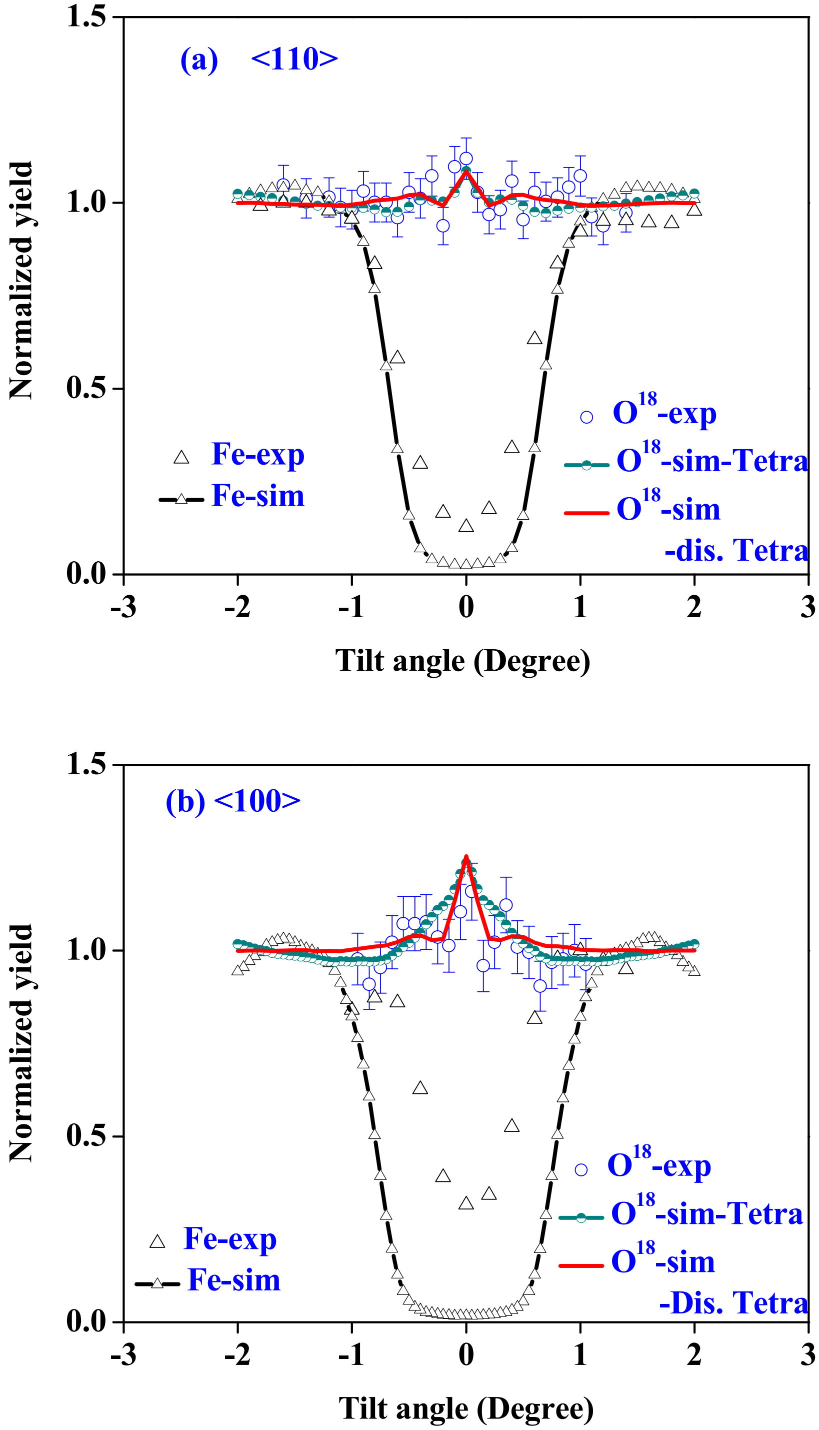

Figure 3.9 Experimental and simulated tilt angular scans of Fe-RBS and O^{18}-NRA signal along (a) <110> (b) <100> axes of $Fe1(O^{18}+Fe@R_p)$. The simulated O^{18} signals are shown for tetrahedral and displaced tetrahedral site (0.15 Å displaced from tetrahedral towards octahedral site).

The experimental tilt angular scans of O^{18} signal is simulated using the FLUX7 software. In the simulation, the random fraction (f_R) due to the dechanneling of ions from Fe matrix is also taken into account as in Eq. (2.21). The calculated f_R using Eq. (2.22) is 0.1, 0.28 for <110>, <100> axes respectively. First tilt angular scans are simulated for tetrahedral interstitial site.

The simulated tilt angular scans of O^{18} at tetrahedral site (shown in the Fig. 3.9 (a) and 3.9 (b)) are matching within the error bar. However, small humps in either side of the central peak, observed in experimental tilt angular scan along <100> is not matching with tetrahedral site simulation. We also simulated O^{18} tilt angular scans with various displacements from tetrahedral interstitial site. Experimental scan along <100> is matching with simulated curve corresponding to O^{18} with a displacement of 0.15 Å from tetrahedral towards octahedral interstitial site. The displaced tetrahedral site is shown in Fig. 3.10 and the projections of O^{18} at tetrahedral and displaced tetrahedral interstitial sites are shown in Fig. 3.11. No additional random contribution from O^{18} is added during the fitting. Hence O^{18} is found to be stable at the displaced tetrahedral interstitial position after self-ion irradiation.

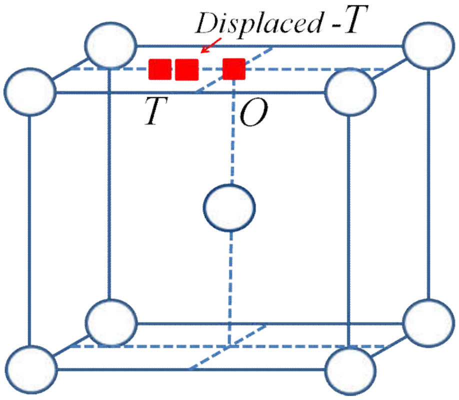

Figure 3.10 Displaced tetrahedral site observed in O^{18} and self ion implanted Fe(110).

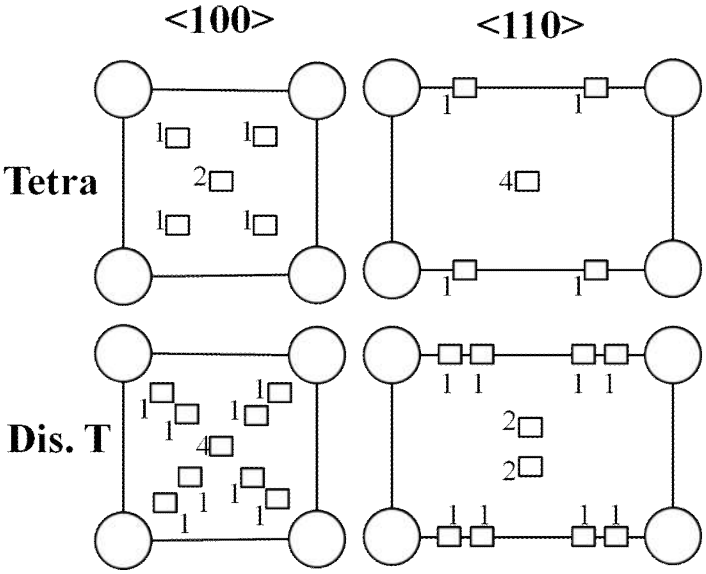

Figure 3.11 Projection of O^{18} along <100> and <110> axis for tetrahedral and displaced tetrahedral site.

3.6. Positron annihilation spectroscopy to study vacancy defects

The SPDBS measurements are done in *Fe1*(O^{18}*+Fe@*R_p) sample. **F**rom SPDBS, the *S* parameter is measured as a function of incident positron beam energy at room temperature. The obtained *S* parameter of this sample at room temperature together with the pristine reference sample is shown in Fig. 3.12 (a). The *S* parameter is sensitive to type of open volume defects such as mono vacancies and vacancy clusters and the diffusion length is sensitive to vacancy defect density where lower defect density has higher diffusion length. Increase of *S* parameter is evident compared to reference sample for all energies. For pristine reference sample, *S*(*E*) curve is analyzed and is fitted with single layer mode by using VEPFIT code, which gives fitted *S* parameter of 0.487 and diffusion length of 130 nm.

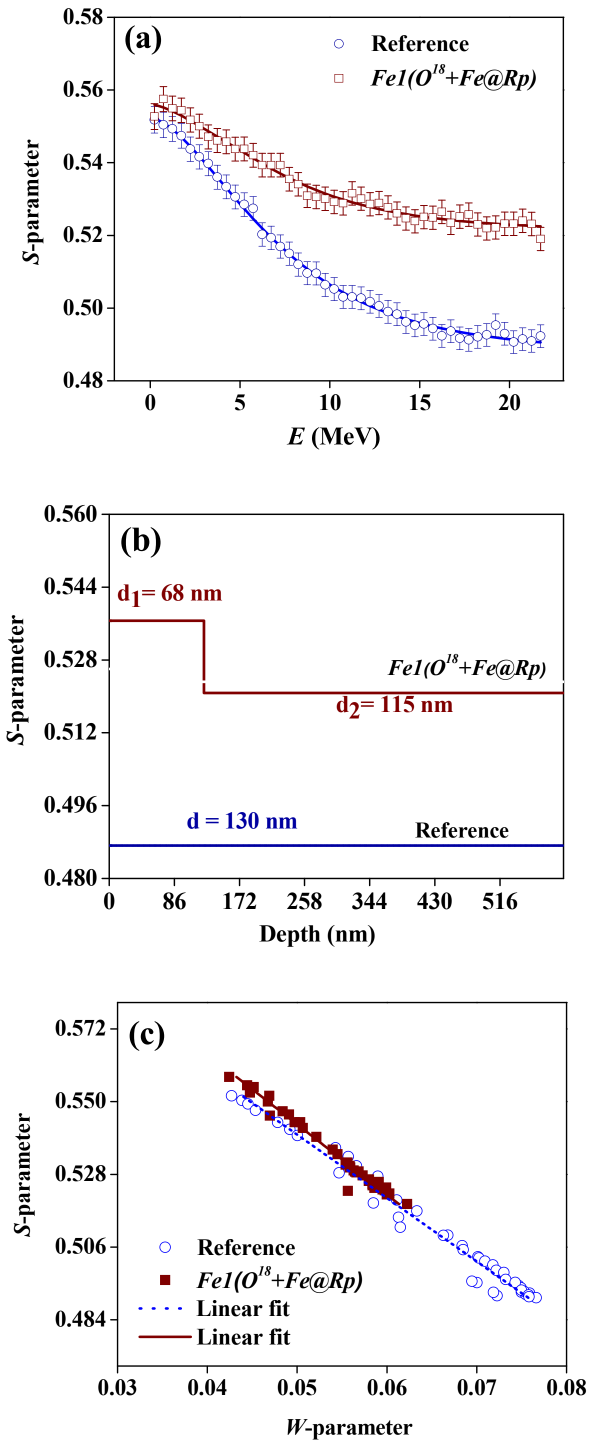

Figure 3.12 (a) The experimental and VEPFIT simulated S parameter as a function of positron energy, (b) Depth resolved S parameter and diffusion lengths, (c) S vs W parameter for reference Fe(110) and $Fe1(O^{18}+Fe@R_p)$.

In $Fe1(O^{18}+Fe@R_p)$, the $S(E)$ curve is analyzed and is fitted using VEPFIT code by assuming two layers. The depth resolved S parameter and diffusion length obtained is shown in Fig. 3.12 (b). The spectrum is fitted by assuming two layers, where first layer is from surface to 120 nm depth and second layer is from 120 nm to 710 nm. The *S* parameter for first layer is 0.537 which is slightly higher than the second layer value 0.52 and the diffusion lengths in first and second layers are 68 nm and 115 nm respectively. The vacancy concentration in the assumed layers is calculated using the relation [83],

$$Nv = \frac{\rho}{\gamma \tau^{b}} \left(\frac{L_{+,b}^{2}}{L_{+.t}^{2}} - 1 \right) (cm^{-3}) \tag{3.1}$$

where ρ is the atomic number density (8.497×10^{22} atoms/cm^3 for pure Fe), τ_b is the annihilation life time of positron in bulk (110 ps for defect free Fe) [84], γ is the specific positron trapping rate of mono vacancy (1×10^{15} s^{-1}) [85], and $L_{+,b}$ and $L_{+,t}$ are the effective diffusion lengths in defect free bulk and defected Fe layer, respectively. The calculated vacancy concentration of first and second layer is 2.05×10^{18} cm^{-3} and 2.15×10^{17} cm^{-3} respectively. High vacancy density is observed in first layer compared to second layer in both irradiated samples. The increase of vacancy concentration in first layers is attributed to the loss and trapping of interstitials at surfaces which induce an imbalance in vacancy with respect to interstitials. These results in a high density of vacancies in surfaces compared to bulk. Recent *ab initio* study of Aliaga *et al*. [86], strongly supports our observation. The *S-W* plot is shown in Fig. 3.12 (c). All data points show single linear fit for reference as well as *Fe1*(O^{18}+*Fe@*R_p) sample, which implies that the same type of vacancy defect is present in the sample.

3.7. DFT studies of O interaction with interstitial defects in Fe

The above experiments confirm the presence of dislocation loops and vacancy defects at O^{18} depth. However the dislocation loops could be vacancy and interstitial type with ½ <111> and <100> structure. When excess interstitial defects are introduced, the interstitial defects and interstitial dislocation loops could be the dominant defects formed at O^{18} depth. Lattice site position of O^{18} is found to be closer to tetrahedral interstitial site in $Fe1(O^{18}+Fe@R_p)$. To elucidate the obtained experimental results, the interaction and lattice location of oxygen with small self-interstitial clusters are studied in bcc Fe by using the DFT calculations.

Ferromagnetic state is found to be stable for defect free bcc Fe lattice by using spin polarized calculations. DFT predicted the lattice constant of 2.831 Å for bcc Fe and magnetic moment per atom of 2.2 μ_B, which are comparable with the experimental values of 2.867 Å and 2.2 μ_B respectively. The octahedral interstitial site is predicted by DFT for O in bcc Fe [51]. For mono interstitial defect <110> dumbbell defect is found to be most stable [21-23]. The self interstitial <110> dumbbell formation energy is calculated by using the equation,

$$E_f(SIA) = E_{N+1}(defect) - \left(\frac{N+1}{N}\right) E_N(perfect) \tag{3.2}$$

where $E_{N+1}(defect)$ is energy of cell containing a dumbbell defect and $E_N(perfect)$ is energy of cell without any defect [13]. The calculated formation energy of <110> dumbbell defect at constant volume condition is 4.08 eV which is comparable to the value of 4.02 eV obtained by Olsson *et al.* [87].

To test the lattice site of oxygen in the presence of most stable <110> dumbbell SIA configuration, DFT calculations are performed with 128 atom bcc Fe lattice with a oxygen atom at nearby octahedral site of <110> self interstitial dumbbell. In all the relaxed structures, oxygen is found around octahedral interstitial site with small displacements. In one configuration which is shown in Fig. 3.13, where the initial site of oxygen is taken at octahedral site (denoted as I), oxygen is found to be displaced away from octahedral site (denoted as F1) towards <110> with a displacement of 0.48Å. These predicted values do not match with experiment (tetrahedral interstitial site). In a separate DFT calculation (GGA-PW method, tetrahedron method of Brillion zone integration and PAW basis set with cut off energy of 400 eV are used, while keeping other parameters same as earlier calculations), the interactions of oxygen (at I site) with <110> SIA dumbbell is studied in 128 atom bcc Fe lattice. Oxygen is observed at tetrahedral site (shown in Fig. 3.13 as F2) after relaxation of ions. However, repulsive binding energy (-0.3 eV) is observed for oxygen interaction with <110> self interstitial dumbbell.

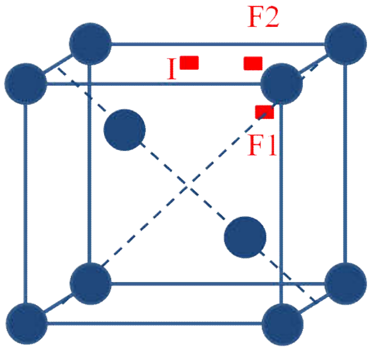

Figure 3.13 Defect structure of <110> dumbbell with oxygen (rectangle).

The O interactions with small interstitial clusters in the form of dislocation loops are also studied to compare with experiment. The dislocation loops with few dumbbell (I) self interstitial clusters are constructed. The ½ <111> and <100> interstitial type dislocation loops consist of <111> and <100> self-interstitial dumbbells, respectively [88]. The cluster of three <111> dumbbells (I_3) for ½ <111> dislocation loop (*I_3-1/2<111>*) is shown in Fig. 3.14 (a) and a cluster of four <100> dumbbell (I_4) for <100> dislocation loop (*I_4-<100>*) is shown in Fig. 3.14 (b). These two defect configurations are considered for studying oxygen interactions with interstitial dislocation loops. As oxygen is predicted at the octahedral interstitial site in defect-free bcc Fe, it is placed at various octahedral interstitial sites of these two interstitial clusters as marked as 1, 2, 3, 4 in Fig. 3.14 (a) and 3.14 (b). The oxygen lattice site location is studied after atomic relaxation. The binding energy and lattice location of oxygen in the defect structures containing oxygen and self interstitial clusters are presented in Table 3.1.

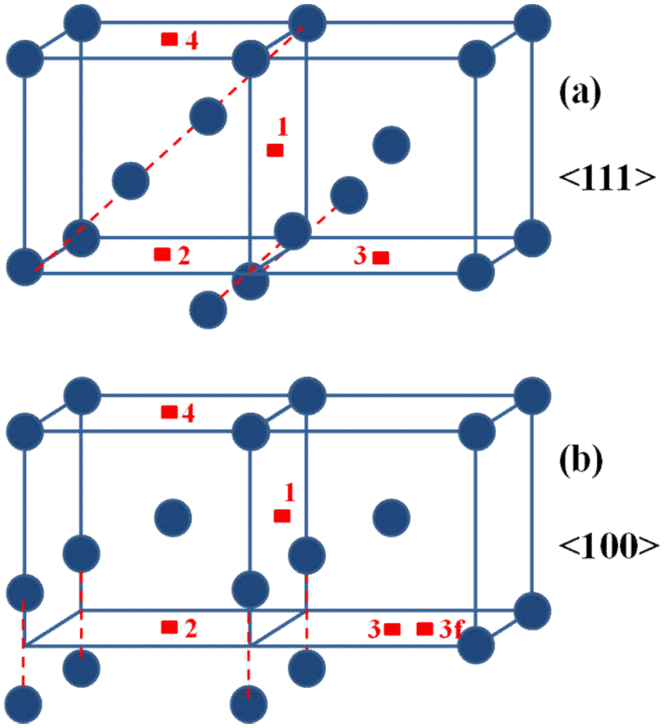

Figure 3.14 The schematic of (a) ½ <111> loop structure containing three <111> dumbbells, (b) <100> loop structure containing four <100> dumbbells. The initial lattice location of oxygen is marked as 1, 2, 3, 4. The final oxygen lattice location is marked as 3f for the case of oxygen at position 3.

The computed results show that the studied defect clusters containing (I_3*-1/2<111>*) dislocation loop and an O atom at four different configurations are found to be unstable after relaxation. The defect clusters containing <100> dumbbells and an O atom, I_4*-<100>-O(1)* and I_4*-<100>-O(4)* (the number within bracket is the oxygen site position marked in Fig .3.14) are also found to be unstable. One of the considered (I_4*-<100>-O(3)*) defect structures shows that the oxygen atom is found to be displaced by 0.37 Å from tetrahedral position towards octahedral interstitial site, as shown in Fig. 3.14 (b), which is closer to the experimentally observed 0.15 Å displaced tetrahedral site. The calculated binding energy of oxygen with the above (I_4*-<100>-O(3)*) cluster is 0.24 eV. This suggests that the oxygen has attractive interactions with interstitial clusters/loops. Hence the observed displaced tetrahedral interstitial site could be due to trapping of oxygen at interstitial dislocation loops.

Table 3.1 DFT predicted binding energy and lattice location of oxygen within the oxygen-self interstitial defect structures

Defect structure	**Lattice location of oxygen**	**Binding energy of oxygen**
I_3-½ <111>-O(1)	Octahedral	-
I_3-½ <111>-O(2)	Octahedral	-
I_3-½ <111>-O(3)	Octahedral	-
I_3-½ <111>-O(4)	Octahedral	-
I_4-<100>-O(1)	Octahedral	-
I_4-<100>-O(2)	Octahedral	-1.5 eV
I_4-<100>-O(3)	0.37 Å displaced from tetrahedral to octahedral	0.24 eV
I_4-<100>-O(4)	Octahedral	-

Oxygen interactions with vacancy defects (mono- and di-vacancy) and vacancy dislocation loops (both ½ <111> and <100> structure) are also studied which will be discussed in chapter.4. The tetrahedral site of O is not observed in presence of vacancy dislocation loops which is also in correlation with present findings.

3.8. Conclusion

The O^{18} ion is implanted in bcc Fe(110) crystal to study O interaction with interstitial defects. During ion implantation, self interstitial defects could be formed at O^{18} implanted depth. The lattice location of O^{18} is measured by ion channeling technique and O^{18} is found around tetrahedral interstitial site. Excess interstitial defects are introduced over the O^{18} depth to study the stability of tetrahedral interstitial site of O^{18}. The O^{18} is found to be stable around the tetrahedral interstitial site with a displacement of 0.15 Å from tetrahedral interstitial position towards octahedral interstitial site. The presence of dislocation loops with mean loop radius higher than 20 nm is confirmed by energy dependant dechanneling parameter measurements. Presence of vacancy defects is also confirmed by SPDBS measurements. However, experimentally observed displaced tetrahedral site of O^{18} is predicted with displacement of 0.37 Å by DFT calculations for the interaction of oxygen with <100> interstitial dislocation loop structure. These results suggest that the experimentally observed displaced tetrahedral interstitial site of oxygen could be due to trapping at interstitial dislocation loops and the oxygen is having attractive interaction with interstitial dislocation loops.

Chapter 4

Interactions of oxygen with vacancy defects in bcc Fe

Vacancies (V) are produced in crystals during neutron damage or ion irradiation. The solute-V interactions play a major role in formation of voids in structural materials. Small amount of C, N, H, O impurities are present in the structural materials during its preparation. The O-V clusters are found as a constituent of fine metal oxide clusters dispersed in ODS alloys where O-V cluster can act as a sinks for radiation induced defects [51,89]. In this regard, the O interaction with vacancy is studied using simulations as well as experiments in literature. However, the visible defect during ion implantation in Fe is the appearance of dislocation loops. Both interstitial and vacancy dislocation loops are formed under ion implantation. In chapter 3, O^{18} ions are implanted in Fe(110) and self ions are also implanted at same depth and the interactions of O with interstitial defects are studied. The present chapter aims to understand interactions of O with vacancy defect and find the defect structure of O-V clusters formed in ion implanted and annealed Fe crystal. To introduce excess vacancy defects, self ion implantation is performed.

4.1. Introduction of O^{18} and vacancy defects by self ion implantation

Ion implantation produces collision cascades in the matrix which promotes the formation of vacancies and self interstitials. The SRIM [54] simulated ion and vacancy profiles for 300 keV O^{18} ions and 1550 keV Fe^+ ions in Fe matrix are shown in Fig. 4.1. The projected range (R_p) and straggling of 300 keV O^+ ions in Fe is 275 nm and 78 nm respectively.

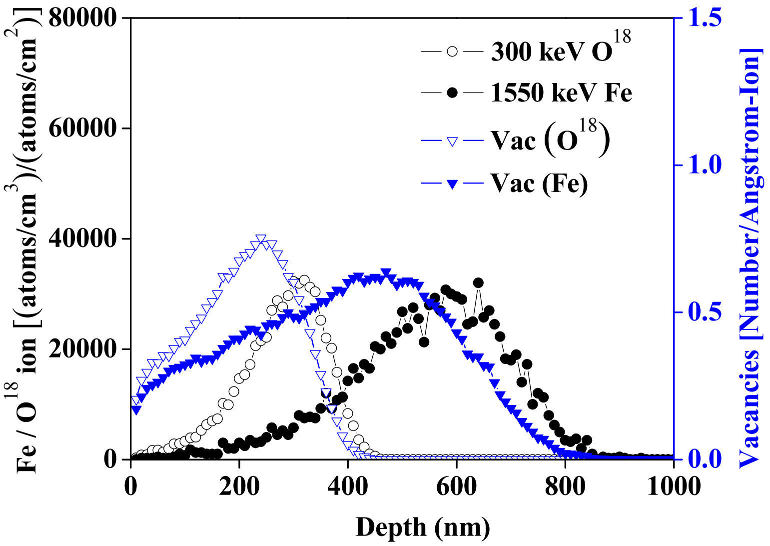

Figure 4.1 SRIM calculated range of ions and vacancies in Fe crystal produced by 1550 keV Fe ions and 300 keV O$^+$ ions.

The energy of Fe ion is chosen such that half of its projected range ($R_p/2$) overlaps with R_p of O. It is known that higher vacancy concentration will be present at a depth equal to half the projected range ($R_p/2$) of implanted ions due to the forward recoil momentum of displaced atoms and recombination of defects [90]. This $R_p/2$ effect is utilized to introduce additional vacancies overlapping with oxygen concentration depth profile, by implanting Fe$^+$ ions with 1550 keV energy, which has a range of 540 nm. In this study, bcc Fe(100) crystal with a chemical purity of 99.98% is first implanted with 1550 keV Fe$^+$ ions at a fluence of 1×10^{16} ions/cm^2 and sequentially implanted with 300 keV O^{18} ions with ion fluence of 5×10^{15} ions/cm^2 at room temperature and *in-situ* annealed at 400 °C for 30 mins. The estimated total damage produced by O^{18} and Fe$^+$ ion implantation is 9.3 dpa at O^{18} depth. Here after, this sample is called as $Fe2(O^{18}+1Fe@2R_p)$. The O^{18} and $1Fe@2R_p$ in the bracket represent O^{18} ion implantation and Fe$^+$ ion implantation at 2R_p of O^{18} with ion fluence of 1×10^{16} ions/cm^2.

After ion channeling measurements, the Fe(100) crystal is implanted again with 1550 keV Fe$^+$ ions with the ion fluence of 1×10^{16} ions/cm^2 and annealed at 400 °C with the aim of increasing the vacancy defect concentration further. Now the estimated total damage at O^{18} depth is increased to 15 dpa. Here after, this sample is called as $Fe2(O^{18}+2Fe@2R_p)$. The O^{18} and $2Fe@2R_p$ in the bracket represent O^{18} ion implantation and Fe^+ ion implantation at $2R_p$ of O^{18} with total ion fluence of 2×10^{16} ions/cm^2.

4.2. Range of defects by RBS/channeling

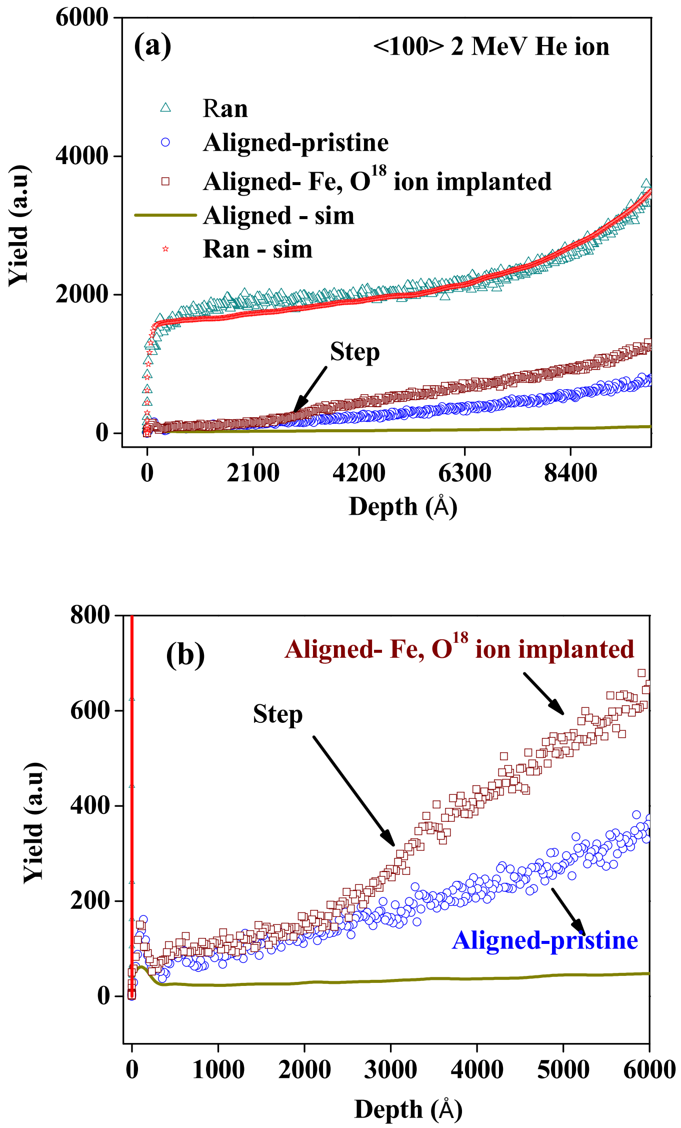

Figure 4.2 (a) RBS spectra of pristine Fe(100) and $Fe2(O^{18}+1Fe@2R_p)$ taken with 2 MeV He^+ ions along <100> axis and random direction. Simulated RBS spectra of ideal Fe(100) along random and <100> axial direction is given for comparison. (b) Same graph with small scale showing a step in the aligned spectrum of $Fe2(O^{18}+1Fe@2R_p)$.

The RBS and channeling measurements are carried out with 2 MeV He^+ ions to study range of defects formed in $Fe2(O^{18}+1Fe@2R_p)$. Figure 4.2 (a) shows the RBS spectra after depth conversion using FLUX7 program from pristine Fe(100) and $Fe2(O^{18}+1Fe@2R_p)$ along random and aligned directions. The random and channeling spectra for ideal Fe(100) crystal, simulated using FLUX7, are also shown in Fig. 4.2. The value $\chi_{min} = Y_{aligned} / Y_{random}$ taken at near surface region of RBS scan is the measure of crystalline quality. For an ideal Fe crystal, it has to be 1.3% along <100> and 1.83% along <110>. Measured χ_{min} is 6.4% at 50 nm depth in pristine crystal, which is retained after ion implantation and annealing also. In contrast to pristine channeling spectrum, a clear dechanneling step could be seen after 250-350 nm depth in implanted Fe(100) (Fig. 4.2 (b)). The dechanneling is high around O^{18} peak concentration (range 275 nm, straggling 78 nm) profile and it implies that defect density is high at the O^{18} depth profile.

4.3. Type of defects by energy dependent dechanneling measurements

To study the type of defects present at O^{18} implanted depth, energy dependent channeling measurements are carried out in $Fe2(O^{18}+2Fe@2R_p)$. The RBS measurements are done using He^+/He^{++} ion beam with energy varying from 1100 keV to 3500 keV at <100> axis and random directions. The RBS spectra are simulated at random and <100> axial directions using FLUX7 program for all incident energies (from 1100 keV to 3500 keV). The random experimental data is fitted with simulation and experimental spectra of random and <100> axial direction are converted to depth *vs* yield. The depth converted experimental and simulated RBS spectra at <100> axis aligned and random direction of $Fe2(O^{18}+2Fe@2R_p)$ crystal are shown in Fig. 4.3 for He^+/He^{++} ion energies from 2000 keV to 3500 keV in steps of 300 keV. From the depth resolved experimental and simulated RBS spectra, the variation of χ_{min} with depth for pristine (χ_V) and ion implanted (χ_D) samples are obtained.

The type of defects at a particular depth can be determined by energy dependence of the dechanneling parameter (*DP*) which is given by Eq. (2.10) in section 2.9 of chapter 2. The calculated *DP* up to the probing depth of He^{+}/He^{++} ions with various incident energies are shown in Fig. 4.4. With linear fitting of experimental *DP* data shown in Fig. 4.4, around O^{18} ion implanted depth, the value of *d(DP)/dz* is obtained.

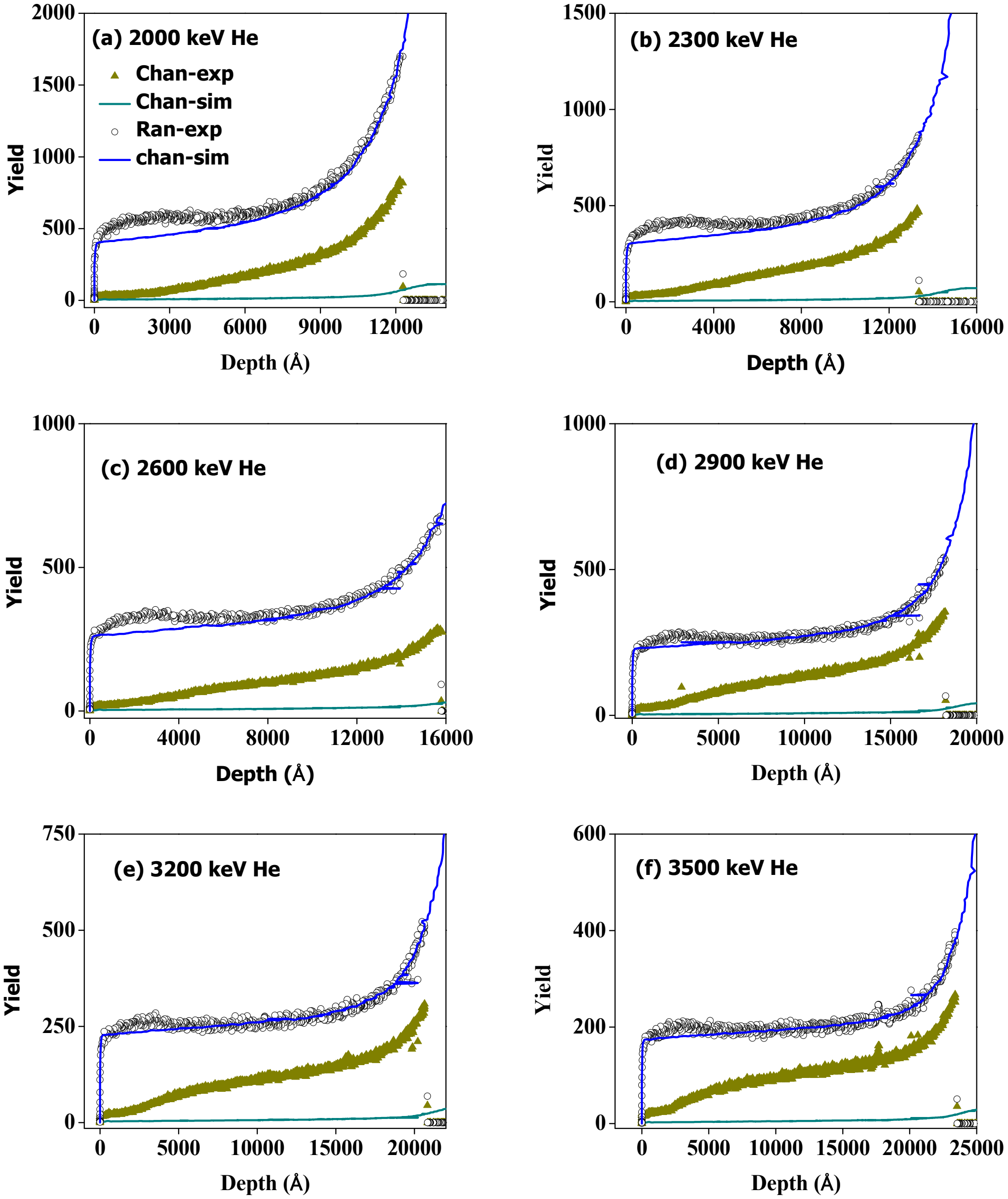

Figure 4.3 Depth converted experimental and simulated RBS spectra at random and <100> axial direction of *Fe2*(O^{18}*+2Fe@2*R_p) crystal performed with (a) 2000 keV, (b) 2300 keV, (c) 2600 keV, (d) 2900 keV, (e) 3200 keV and (f) 3500 keV of He^{+}/He^{++} ions.

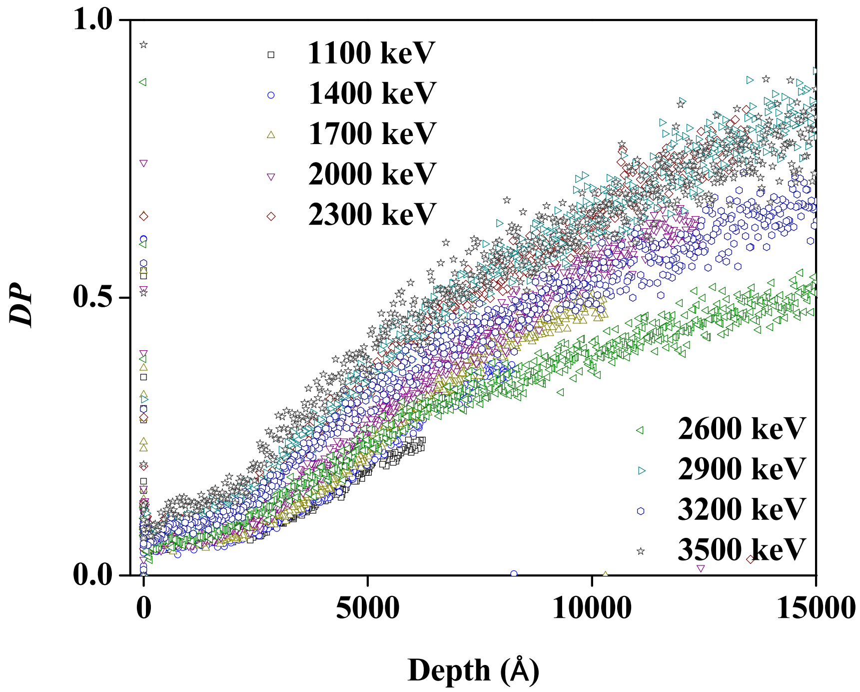

Figure 4.4 The depth resolved *DP* in $Fe2(O^{18}+2Fe@2R_p)$ measured with various helium ion energies.

The He^+ ion energy dependence of *DP*, along <100> axis of $Fe2(O^{18}+2Fe@2R_p)$, around the depth of 270-280 nm, is measured and presented in Fig. 4.5 (a). The linear fit of experimental data points shows $E^{0.5}$ dependence of *DP* which confirms the presence of dislocations [52]. For the ion fluences and annealing temperatures used in this sample, formation of dislocation loops is expected as reported in literature from TEM analysis [28,29]. To verify the presence of dislocation loops, dechanneling parameter per unit length in the depth range of 200-400 nm (O^{18} ion range is 275±78 nm) versus $E^{0.5}$ is plotted in Fig. 4.5 (b). It shows linear dependence with $E^{0.5}$ up to maximum measured ion energy of 3500 keV indicating the presence of dislocation loops. For dislocation loops, the dechanneling parameter per unit length increases linearly up to transition energy (E_s) and becomes constant at higher energies. From E_s, mean dislocation loop radius (*R*) can be determined using Kudo's analysis [62] from the relation $E_s = aR^2$, where a is Thomas-Fermi screening distance = 0.142 Å. In the present sample E_s will be higher than 3500 keV.

If one assumes the dislocation loops as ½ <111> loops, the obtained mean radius is greater than 23 nm. If the dislocation loops are assumed as <100> loops the mean dislocation loop radius will be greater than 45 nm.

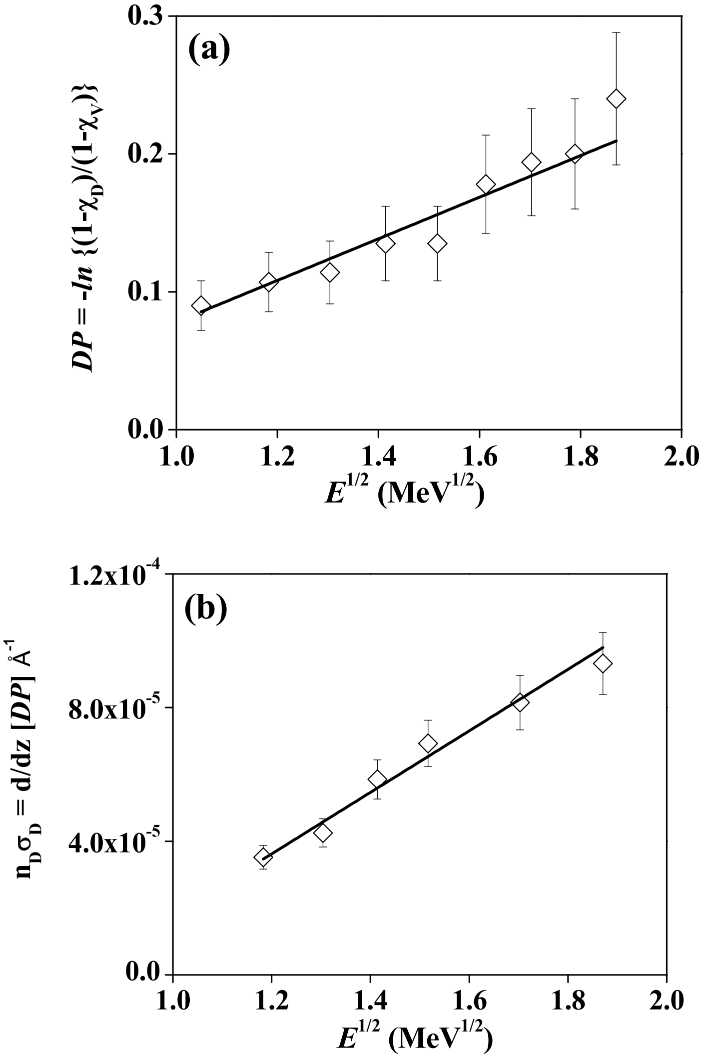

Figure 4.5 (a) Energy dependence of *DP* in $Fe2(O^{18}+2Fe@2R_p)$ along normal axis around the depth of 275 nm. (b) Energy dependence of dechanneling parameter per unit length measured from 200 nm to 400 nm depth.

The defect density of dislocation loops is calculated from the slope of linear fit shown in Fig. 4.5 (b) using Eq. (2.13). The value of ψ_1 is calculated by using Eq. (2.15), for 2 MeV He^+ ions in bcc Fe crystal. The ψ_1 value is 0.9° for <100> axis. The Burgers vector of <100> loop is 2.87 Å and Burgers vector for ½ <111> loop is 1.43 Å in bcc Fe. The calculated dechanneling factor σ_D is 18 Å for <100> dislocation loops and 13 Å for ½ <111> dislocation loops which are calculated using Eq. (2.14). The observed defect density is 6.9×10^{10} dislocation loops/cm^2 for the case of <100> loops and 9.8×10^{10} dislocation loops/cm^2 for the case of ½ <111> loops.

4.4. Lattice location of O^{18} in the presence of excess vacancy defects in Fe(100)

The experimental tilt angular scans of Fe - RBS and O^{18} - NRA signal, taken around <100> and <110> axes in $Fe2(O^{18}+1Fe@2R_p)$ (self ion fluence of 1×10^{16} ions/cm^2) with 850 keV protons are presented in Fig. 4.6 (a) and 4.6 (b) respectively. Figure 4.6 (c) and 4.6 (d) show the tilt angular scans performed in $Fe2(O^{18}+2Fe@2R_p)$ (total self ion fluence of 2×10^{16} ions/cm^2). The shape of the tilt angular scans in Fig. 4.6 (c) and 4.6 (d) are different from that of Fig. 4.6 (a) and 4.6 (b), indicating that oxygen position changes with increase in concentration of vacancy defects. The experimental χ_{min} obtained from the tilt angular scans shown in Fig. 4.6 (a), 4.6 (b), 4.6 (c), and 4.6 (d) are 0.07, 0.1, 0.08, and 0.13 respectively. The observed random dechanneling fraction of protons, for tilt angular scans given in Fig. 4.6 (a), 4.6 (b), 4.6 (c), and 4.6 (d) are 0.05, 0.1, 0.07, and 0.12 respectively, which are calculated using Eq. (2.22). The experimental tilt angular width of the scans given in Fig. 4.6 (a), 4.6 (b), 4.6 (c), 4.6 (d) are 0.78°, 0.6°, 0.78°, 0.57° respectively, which are comparable with the simulated width of 0.8° for <100> and 0.67° for <110> axis.

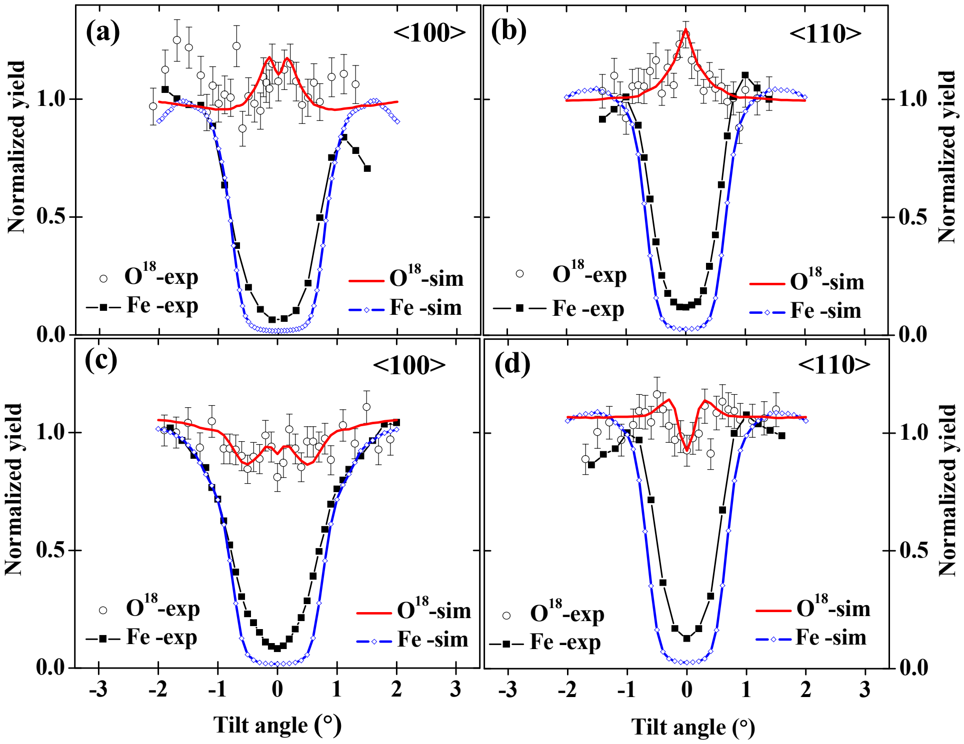

Figure 4.6 Experimental and simulated Fe and O^{18} tilt angular scans of $Fe2(O^{18}+1Fe@2R_p)$ along (a) <100> (b) <110> axes. Experimental and simulated Fe and O^{18} tilt angular scans of $Fe2(O^{18}+2Fe@2R_p)$ are given in (c) along <100>, (d) along <110>.

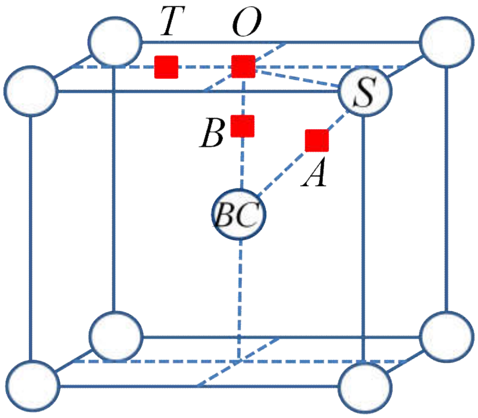

Figure 4.7 Lattice site locations of substitutional (*S*), body centre (*BC*), octahedral (*O*) interstitial, tetrahedral (*T*) interstitial, site *A* and site *B* in bcc Fe lattice.

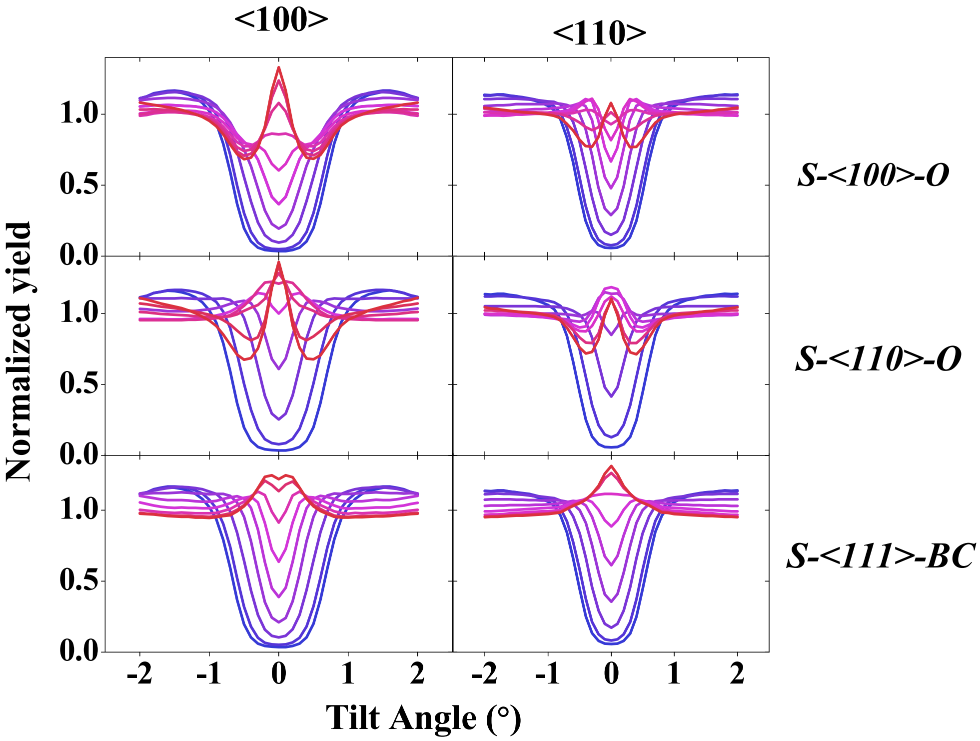

Figure 4.8 FLUX7 simulated tilt angular scans of O^{18} signal along <100>, <110> axis with 850 keV protons. In the simulated scans the lattice site of O^{18} is shifted from substitutional to nearest octahedral (*S-<100>-O*), substitutional to second nearest octahedral (*S-<110>-O*) and substitutional to body centre (*S-<111>BC*).

To identify the O^{18} site, the tilt angular scans along <100> and <110> axes with O^{18} at standard sites; substitutional (*S*), body centre (*BC*), octahedral (*O*) and tetrahedral (*T*) interstitial sites (shown in Fig. 4.7) are simulated. The tilt angular scans of O^{18} signal along <100> and <110> axes are also simulated by varying O^{18} position from *S* to nearest octahedral site along <100> direction (*S-<100>-O*), *S* to second nearest octahedral site along <110> direction (*S-<110>-O*) and *S* to *BC* along <111> direction (*S-<111>-BC*) as marked in Fig. 4.7. The simulated tilt scans with the above positions of O^{18} are presented in Fig. 4.8. Each of tilt angular scans is different for different positions of O^{18}.

All the simulated scans are compared with experimental scans, however, the best fit shown in Fig. 4.6 (a) and 4.6 (b) is obtained for the site *A* which is displaced 1.2 Å from lattice site along <111> direction. During fitting process, random fraction from Fe matrix is accounted as in Eq. (2.21). In addition, 30 % random fraction of O^{18} is added which gives strong evidence of 70 % of O^{18} at site *A*. The best fit in Fig. 4.6 (c) and 4.6 (d) is obtained with 70% of O^{18} at site *B* which is displaced 0.85 Å from lattice site to 1st nearest neighbor octahedral interstitial site along <100> or in other words 0.62 Å from octahedral along <100>. During fitting process, random fraction from Fe matrix is accounted as in Eq. (2.21) with addition of 30% random fraction of O^{18}. The projection of O^{18} at site *A* and site *B* is shown in Fig. 4.9. It is obvious that O^{18} is shifting to a different lattice site position with increase in density of vacancy defects. These positions may have correlation with trapping of oxygen with ½<111> and <100> dislocation loops which are expected for the ion fluences used here. It is to be noted that the positions of oxygen observed here are much different from the tetrahedral interstitial sites observed in the previous chapter with implantation of O^{18} alone, as the defect structures are different.

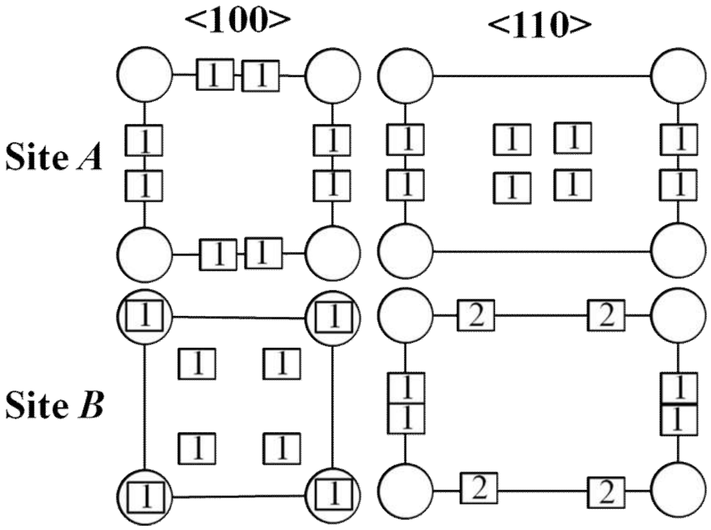

Figure 4.9 Projection of Fe (circle), O^{18} (rectangle) at site *A* and site *B* along <100> and <110> axis in bcc Fe.

4.5. Positron annihilation spectroscopy to study vacancy defects

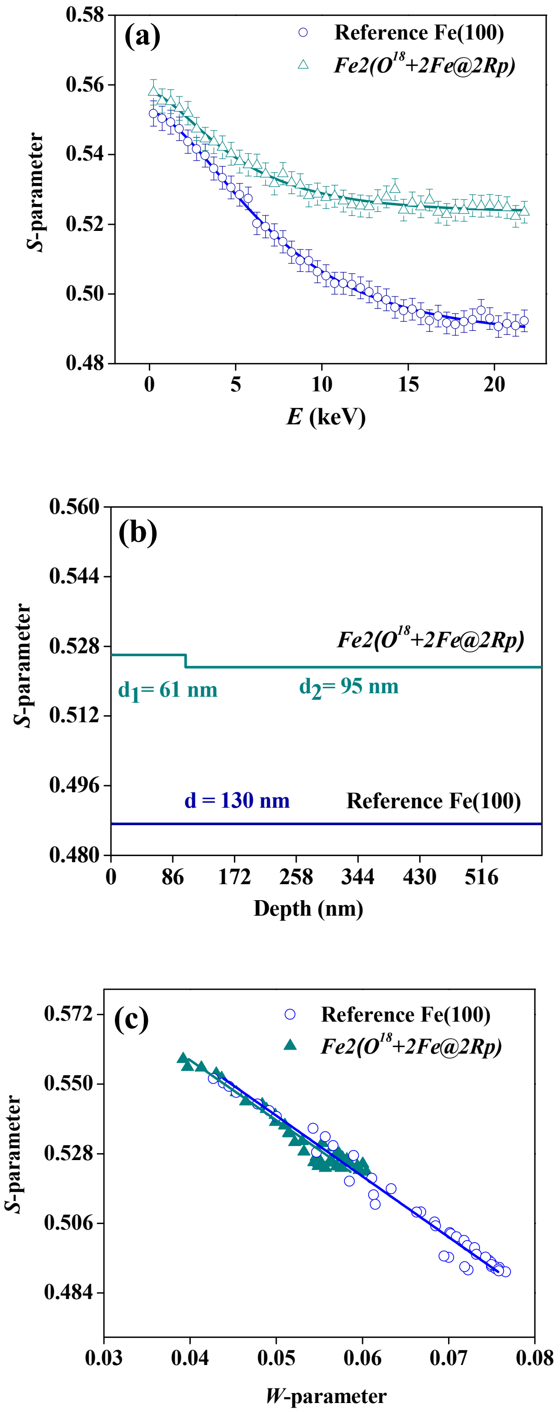

Figure 4.10 (a) The experimental and VEPFIT simulated *S* parameter as a function of positron energy, (b) Depth resolved *S* parameter and diffusion lengths, (c) *S vs W* plot for reference Fe(100) and *Fe2(*O^{18}*+2Fe@2*R_p*)*.

The SPDBS measurements are done in *Fe2*(O^{18}*+2Fe@2*R_p) sample. The *S* parameter as a function of incident positron beam energy from SPDBS measurements performed in this sample at room temperature together with the pristine reference sample is shown in Fig. 4.10 (a). The *S* parameter is sensitive to type of open volume defects such as mono vacancies and vacancy clusters and the diffusion length is sensitive to vacancy defect density where lower defect density has higher diffusion length. The *S* parameter has increased when compared to reference sample for all energies. For pristine reference sample, *S*(*E*) curve is analyzed and fitted with single layer model by using VEPFIT code, which shows *S* parameter of 0.487 and diffusion length of 130 nm. The *S* parameter and effective fitted diffusion length of *Fe2*(O^{18}*+2Fe@2*R_p) is obtained through VEPFIT code with two layer fitting, and is shown in Fig. 4.10 (b). The first layer is from surface to 100 nm and the second layer is from 100 nm to 710 nm where there is O^{18} concentration depth profile. The *S* parameter of first layer is 0.526 which is slightly higher than that of second layer value 0.523 and respective diffusion lengths are 61 nm and 95 nm.

The vacancy concentration is calculated by using Eq. (3.1) (Section 3.6 of chapter 3). The calculated vacancy concentration of first and second layer is 2.74×10^{18} cm^{-3} and 6.74×10^{17} cm^{-3} respectively. The high vacancy density in first layer is attributed to the loss and trapping of interstitials at surfaces. The *S vs W* plot shows single linear fit of experimental data points of reference as well as ion implanted sample (shown in Fig. 4.10 (c)). This implies that one type of vacancy cluster is present in the sample.

4.6. DFT study of O interactions with vacancy defects in Fe

The experimentally observed O^{18} lattice sites in the present chapter do not match with DFT calculations performed for O interactions with interstitial defects in chapter 3. As the vacancies are intentionally introduced at O^{18} depth in this experiment, studying the interaction of O with vacancy defects by DFT is important to understand the present experimental results. The DFT calculations are performed with vacancy defects in a 128 atom Fe cell. The vacancy formation energy of Fe is calculated by the equation,

$$E_f(V) = E_{N-1}(defect) - \left(\frac{N-1}{N}\right) E_N(perfect) \qquad (4.1)$$

where $E_{N-1}(defect)$ is energy of cell containing a dumbbell defect and $E_N(perfect)$ is energy of cell without any defects [13]. The calculated formation energy of vacancy defect at constant volume condition is 2.17 eV which is comparable to the value of 2.15 eV obtained by Derlet *et al.*,[91] and to value of 2.07 obtained by Fu *et al.*, [21].

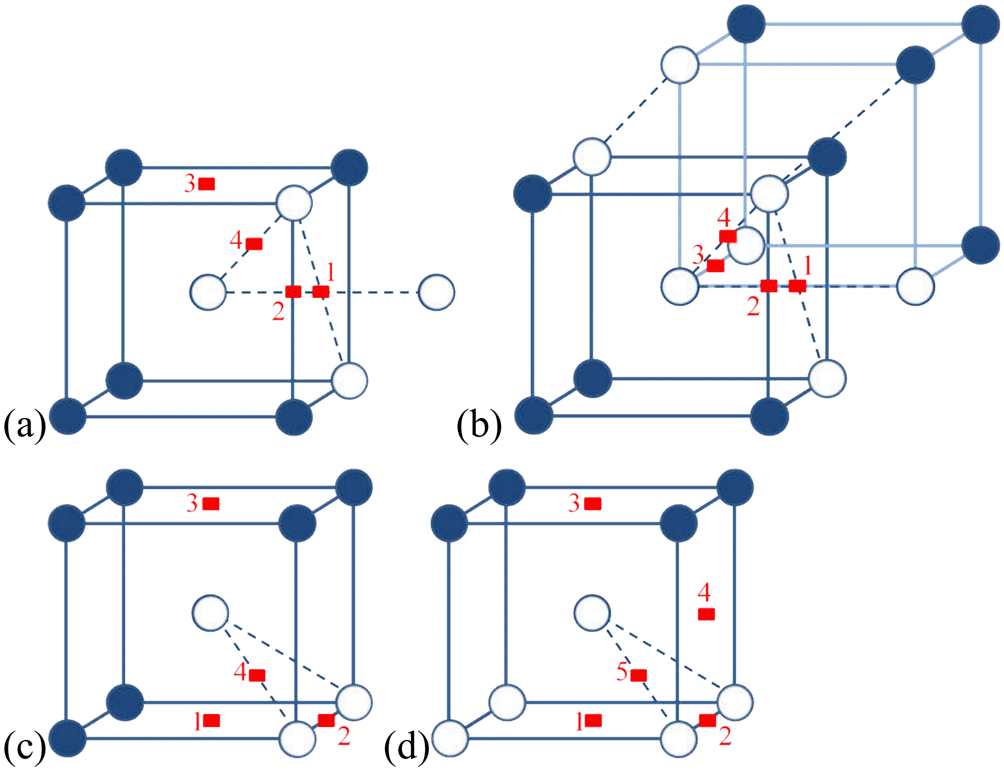

Figure 4.11 Defect structure of ½ <111> dislocation loop with 4 vacancies (a), 7 vacancies (b), and structure of <100> loops with 3 vacancies (c), 5 vacancies (d). The solid circle represents Fe, open circle represents vacancy and various oxygen positions 1, 2, 3, 4 and 5 are represented as solid rectangle.

To identify defect structure of O-V clusters, O interaction with mono and di vacancy defect is studied by using DFT calculations. Oxygen is found to bind at octahedral interstitial site in defect free bcc Fe lattice and also in the presence of di-vacancy. In the presence of mono vacancy, O occupies first nearest neighbor octahedral positions with a displacement of 0.22 Å. The binding energy of O with *V* and V-O are 1.75 eV and 1.81 eV respectively. The results of DFT calculations are in good agreement with the literature [51]. These predications are not matching with the lattice position of oxygen in ion implanted Fe(100) determined by channeling experiments. Since positron annihilation spectroscopy and ion channeling experiments performed in ion implanted Fe(100) predict formation of vacancy and dislocation loop defects respectively, the presence of vacancy dislocation loops would be prominent at O^{18} depth.

These experimentally observed O^{18} lattice location is not matching with O-SIA clusters studied in chapter 3 which also implies that the oxygen is not trapped by interstitial dislocation loops. The vacancy dislocation loop structure can be either ½<111> or <100> type. The trapping sites of oxygen in oxygen-vacancy loop clusters are studied by DFT calculations in order to correlate the experimentally observed lattice sites.

In construction of ½ <111> and <100> vacancy loops many structures could be formed depending on number of vacancies. However, in this chapter, small vacancy loops containing few vacancies are used, due to size restriction of simulation cell. DFT calculations are performed with two ½ <111> vacancy loop structures (Fig. 4.11 (a) and Fig. 4.11 (b)) containing 4 vacancies (V_4-*½<111>*) and 7 vacancies (V_7-*½<111>*) and two <100> vacancy loop structure (Fig. 4.11 (c) and Fig. 4.11 (d)) containing 3 vacancies (V_3-*<100>*) and 5 vacancies (V_5-*<100>*). In order to study oxygen trapping sites in these defects, oxygen atoms are introduced at various octahedral sites 1, 2, 3, 4 and 5 as marked in Fig. 4.11 and the corresponding binding energy and lattice location of oxygen in relaxed minimum energy states are determined by constant volume (*CV*) and zero pressure (*ZP*) methods.

The DFT predicted binding energy of oxygen with vacancy dislocation loops are presented in Table 4.1 along with oxygen lattice position in relaxed structures. In case of V_4-½<111>, attractive interaction of oxygen is observed with binding energy up to 2.13 eV for *CV* and *CP* methods. Oxygen binds at octahedral interstitial site in V_4-½<111>-O(1) configuration (the number within bracket is the oxygen site position marked in Fig .4.11), while in V_4-½<111>-O(2) and V_4-½<111>-O(3) defect configurations, displacement of up to 0.3 Å is observed from octahedral towards <100> directions. The *CV* calculations on defect structures containing similar oxygen sites in V_7-½<111> have been performed. Oxygen is found at off-centered site, with displacement of 0.58 Å, 0.45 Å, 0.45 Å along <111> from substitutional site (*S*) for V_7-½<111>-O(1), V_7-½<111>-O(3), V_7-½<111>-O(4) respectively. In V_7-½<111>-O(2) defect structure, oxygen is found near octahedral displaced 0.29 Å along <100> from octahedral site. The binding energy of oxygen with ½ <111> vacancy loop structure is found to increase with increasing number of vacancies. Out of the considered configurations in DFT calculations, interaction of oxygen in V_4-½<111>-O(4) configuration gives the displacement of 1.16 Å for oxygen from substitutional site along <111> direction comparable to experimental observation of the displacement of 1.2 Å for oxygen from substitutional site along <111> direction (site *A*) in Fe(100).

In $Fe2(O^{18}+2Fe@2R_p)$ crystal, channeling measurements show a displacement of 0.62 Å for O^{18} from octahedral to substitutional site along <100>. Interaction of oxygen with <100> vacancy dislocation loop is considered. In case of O interaction in the defect configuration V_3-<100>-O(2), highest positive binding energy of 2.1 eV is observed and oxygen is found at octahedral interstitial site. Oxygen is found to relax near octahedral for the defect configuration V_3-<100>-O(4). For other defects configurations of V_3-<100>-O with oxygen at 1 and 3 positions, it is found to relax near octahedral site with maximum displacement of 0.3 Å along <100>. For the defect configurations of *V5-<100>-O* with oxygen at 1, 2 and 4 positions, oxygen is relaxed up to a maximum of 0.3 Å along <100> direction. Oxygen is displaced by 0.9 Å along <111> from *S* for the defect configuration *V_5-<100>-O(5).* In case of *V_5-<100>-O(3)* defect structure, oxygen is found to be relaxed 0.46 Å towards the vacancy cluster along <100> in both *CV* and *CP* calculations. Among all the above studied defect configurations, *V_5-<100>-O(3)* gives the displacement of 0.46 Å towards the vacancy cluster along <100>, which is closer to the experimental observation of 0.62 Å displacement from octahedral along <100> (site *B*) in $Fe2(O^{18}+2Fe@2R_p)$.

Table 4.1 DFT calculated binding energy of oxygen with vacancy dislocation loop structures. The lattice location of oxygen in relaxed structures is presented with displacement from octahedral (*O*) or substitutional (*S*) site

Defect structure	Binding energy in eV		O lattice site	
	CV	*ZP*	*CV*	*ZP*
V_4-½<111>-O(1)	1.8	1.68	*O*	*O*
V_4-½<111>-O(2)	2.0	1.87	0.24Å displaced along <100> from *O*	0.23Å displaced along <100> from *O*
V_4-½<111>-O(3)	2.13	2.01	0.3Å displaced along <100> from *O*	0.31Å displaced along <100> from *O*
V_4-½<111>-O(4)	1.9	1.82	1.16Å displaced along <111> from *S*	1.04Å displaced along <111> from *S*
V_7-½<111>-O(1)	2.5	-	0.58Å displaced along <111> from *S*	-
V_7-½<111>-O(2)	1.92	-	0.29Å displaced along <100> from *O*	-
V_7-½<111>-O(3)	2.5	-	0.45Å displaced along <111> from *S*	-
V_7-½<111>-O(4)	2.51	-	0.45Å displaced along <111> from *S*	-
V_3-<100>-O(1)	1.87	1.86	0.23Å displaced along <100> from *O*	0.25Å displaced along <100> from *O*
V_3-<100>-O(2)	2.11	2.1	*O*	*O*
V_3-<100>-O(3)	1.78	1.76	0.3Å displaced along <100> from *O*	0.3Å displaced along <100> from *O*
V_3-<100>-O(4)	1.97	1.92	0.25Å displaced along <100> from *O*	0.26Å displaced along <100> from *O*
V_5-<100>-O(1)	1.2	1.09	0.2Å displaced along <100> from *O*	0.22Å displaced along <100> from *O*
V_5-<100>-O(2)	2.3	2.23	0.1Å displaced along <100> from *O*	0.11Å displaced along <100> from *O*
V_5-<100>-O(3)	2.14	1.96	0.46Å displaced along <100> from *O*	0.46Å displaced along <100> from *O*
V_5-<100>-O(4)	2.07	1.97	0.3Å displaced along <100> from *O*	0.31Å displaced along <100> from *O*
V_5-<100>-O(5)	2.07	2.0	0.9Å displaced along <111> from *S*	0.9Å displaced along <111> from *S*

The 0.9 Å displacement of oxygen along <111> from substitutional site, observed for the defect configuration *V_5-<100>-O(5),* is also closer to experimental observation of site *A*

(displacement of 1.2 Å for oxygen from substitutional site along <111> direction) in *Fe2(*O^{18}*+1Fe@2*R_p*)*. The experimentally observed site *A* is found to be stable for interaction of oxygen with both ½ <111> and <100> vacancy loop structures. From experimental results and DFT predictions, the observed displacement of oxygen is attributed to trapping of oxygen at vacancy dislocation loops.

4.7. Conclusion

Positron experiments confirm the presence of vacancy defects and energy dependent dechanneling measurements show the presence of dislocation loops in ion implanted Fe(100). When excess vacancies are introduced, experimentally, O^{18} is found at site *A*, which is displaced 1.2 Å long <111> from lattice site/vacancy center and upon increasing vacancy defect concentration it is shifting to site *B*, which is 0.62 Å away along <100> from octahedral. From Table 4.1, it can be seen that for the interaction of oxygen with ½<111> vacancy dislocation loop, oxygen is displaced prominently along <111> and for the interaction of oxygen with <100> vacancy dislocation loop, oxygen is displaced prominently along <100>. Oxygen displacement along <100> is observed with increasing vacancies. It is likely that with additional introduction of vacancy defects, there is increase in concentration of ½<111> vacancy dislocation loops which interact among themselves and transform to <100> vacancy dislocation loops during annealing. The displacements predicted by DFT calculations for the interaction of oxygen with ½<111> and <100> vacancy dislocation loops are consistent with the experimentally observed displacements of oxygen. These results provide strong evidence of attractive interaction of oxygen with vacancy dislocation loops and defect trapping of oxygen at dislocation loops in bcc Fe under radiation damage. Furthermore the oxygen-vacancy dislocation defect structure is found to be stable after ion implantation and annealing at 400 °C in the radiation induced microstructure.

Chapter 5

Interaction of oxygen and chromium with interstitial defects in bcc Fe

The FeCr alloy with 5-15 atomic % of Cr is used as a base material for structural materials including ODS steel which show low void swelling under neutron damage [92]. It is important to understand Cr interactions with defects in FeCr alloy. There are many experimental and theoretical studies in FeCr alloy [93]. The Cr interaction strongly depends on Cr percentage and density of defects. Another important problem of FeCr alloy is that the Cr segregates to grain boundaries and defects under radiation damage which affects material properties [93]. The Cr segregation to small interstitial clusters and vacancy clusters has been studied by DFT calculations. The Cr segregated dislocation loops are reported by experimental methods [94] and are also predicted by theoretical calculations [95] in FeCr alloy. But presence of C, H, N, O impurities affects the defect evolution in FeCr alloy [96]. To understand the interstitial solute interaction with dislocation loops in iron, the O^{18} and self ion implanted Fe crystals are studied in chapter 3 and in chapter 4. This chapter aims to better understand the interaction of Cr, a substitutional solute, with defects in iron. It is important to study competing interactions of interstitial solute O and substitutional solute Cr with vacancy and interstitial defects which may shed some light on radiation resistant mechanism of these alloys. The lattice location of O^{18} and Cr in ion implanted and annealed Fe is studied by ion channeling analysis and the corresponding defect structure is studied by using DFT to understand oxygen and chromium interactions with interstitial dislocation loops.

5.1. Introduction of O^{18} and Cr by ion implantation at same depth

A high purity bcc Fe(100) crystal is implanted with 700 keV Cr^+ ions with the ion fluence of 1×10^{16} ions/cm^2 at random directions in room temperature. The sample is annealed *in-situ* in vacuum of 2×10^{-7} mbar at 400 °C for 30 minutes. The lattice location of Cr is measured. Here after, this sample is called as *Fe3(Cr)*. In addition to Cr, 300 keV O^{18} ions with ion fluence of 1×10^{16} ions/cm^2 is implanted in same crystal at random direction and annealed *in-situ* in vacuum of 2×10^{-7} mbar at 400 °C for 30 minutes. This sample is called *Fe3(O^{18}+Cr@R_p)*. The lattice location of O^{18} and Cr are measured to study the effect of Cr^+ ion implantation on O^{18} lattice location. The ion and vacancy range profiles of 700 keV Cr^+ ions and 300 keV O^{18} ions in Fe are simulated by SRIM calculations and are shown in Fig. 5.1. The Cr^+ and O^{18} ion energies are chosen such that both ion profiles are overlapping to interact with each other. The concentration of Cr at peak position is 0.6% and estimated damage is 5.8 dpa at peak position. The concentration of O^{18} is 0.4% at peak position and the estimated damage level is increased to 15 dpa at O^{18} depth.

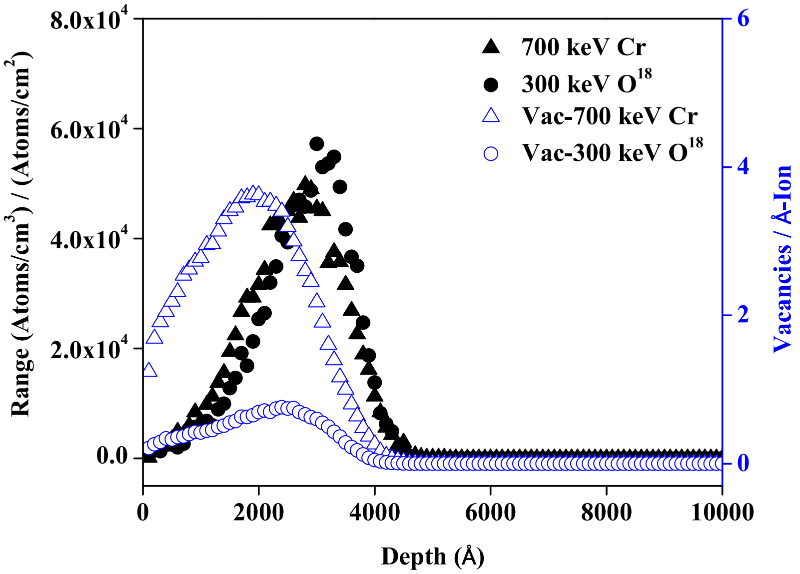

Figure 5.1 The calculated SRIM ion range and vacancy concentration profiles of 700 keV Cr^+ ions and 300 keV O^{18} ions in Fe.

5.2. Depth of defects by RBS/channeling

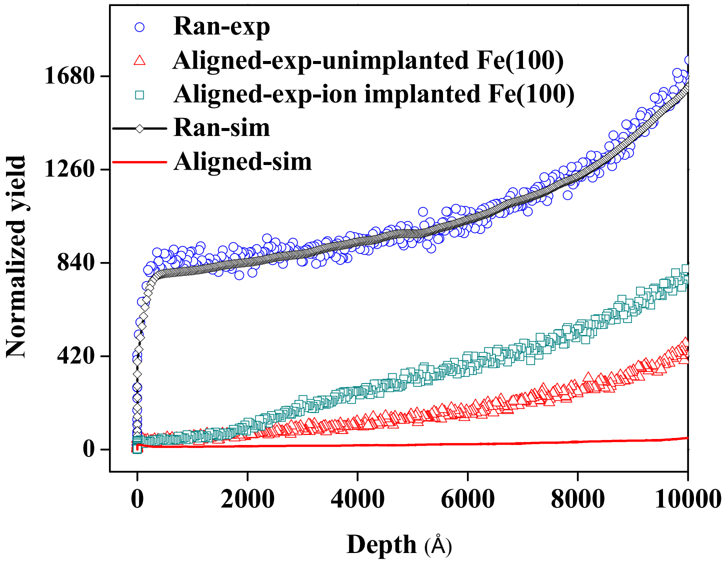

Figure 5.2 Depth converted experimental RBS spectra of pristine and *Fe3(*O^{18}*+Cr@*R_p*)* samples taken by 2 MeV He^+ ions along <100> axis. The simulated RBS spectra of <100> axial and random directions of ideal Fe is given for comparison.

The depth converted RBS spectra recorded along random and <100> axial direction of pristine and *Fe3(*O^{18}*+Cr@*R_p*)* crystal is shown in Fig. 5.2. Only Fe signal is visible in RBS spectra. The Cr and O^{18} signals are taken using PIXE and NRA respectively, which will be discussed later. The RBS spectra of ideal Fe (simulated using FLUX7) along <100> axis and random directions are also shown in Fig. 5.2 for comparison. The value $\chi_{min} = Y_{aligned} / Y_{random}$ measured at 50 nm depth is 5% in pristine crystal which indicates that crystal quality is good. After ion implantation and annealing, the same value is retained. In contrast to pristine channeling spectrum, a clear dechanneling can be seen from 200 nm in implanted Fe(100) due to defects which gives strong evidence of defects at Cr and O^{18} ion implanted depth.

5.3. Type of defects by energy dependant dechanneling measurement

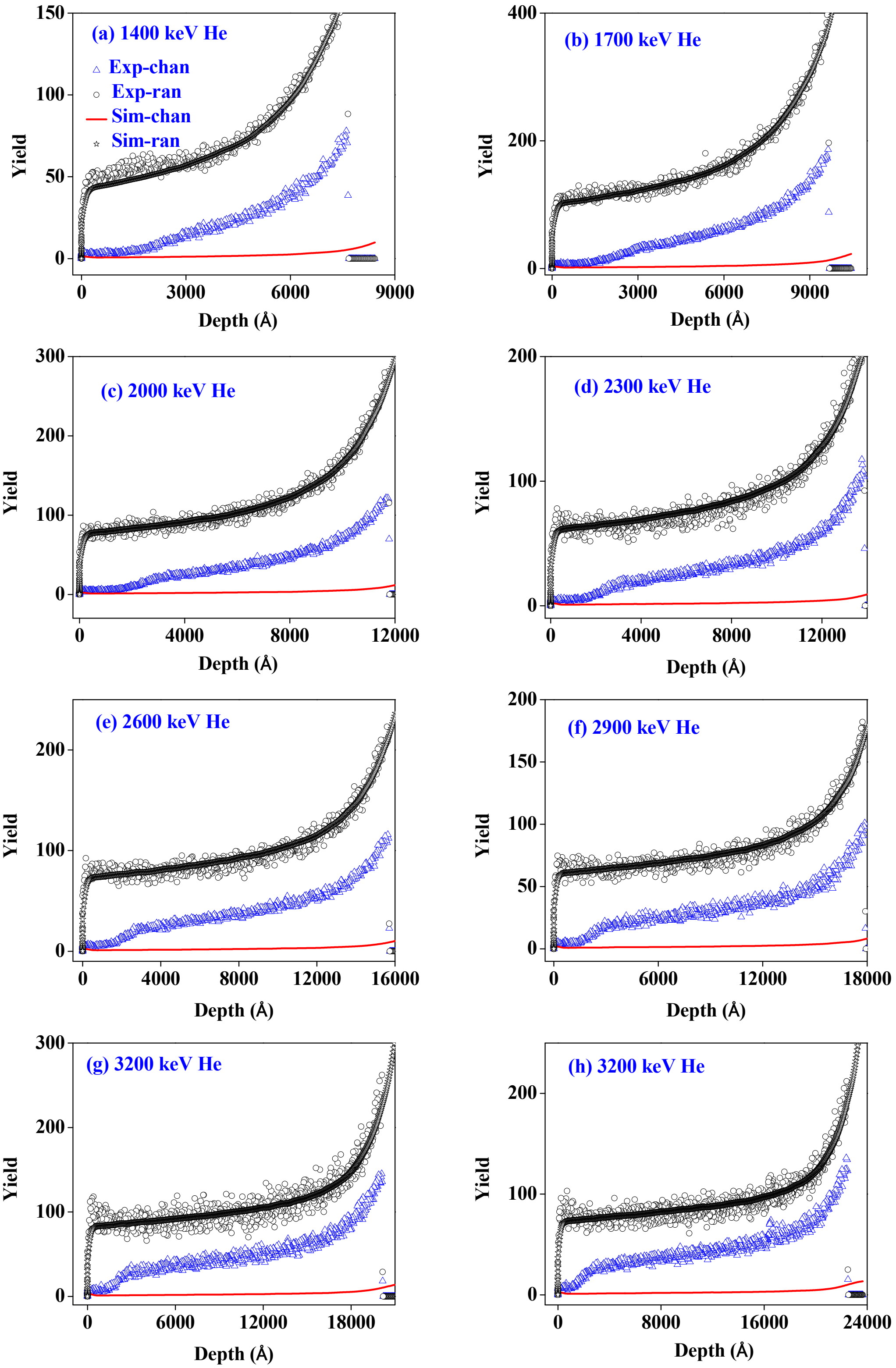

Figure 5.3 Experimental and simulated RBS spectra at <100> axial direction and random direction of *Fe3(O^{18}+Cr@R$_p$)* crystal recorded with He$^+$/He^{++} ions with the energy ranging from (a) 1100 keV to (h) 3200 keV.

Energy dependent channeling measurements are carried out to study the type of defects present at O^{18} implanted depth. The RBS measurements are done using He^{+}/He^{++} ion beam with energy varying from 1400 keV to 3800 keV at <100> axis and random directions of $Fe3(O^{18}+Cr@R_p)$.

The RBS spectra are simulated at random and <100> axial directions using FLUX7 program for all incident energies. The random experimental data is fitted with simulation and experimental spectra of random and <100> axial direction are converted to depth *vs* yield. The depth converted experimental and simulated RBS spectra at <100> axis aligned and random direction of $Fe3(O^{18}+Cr@R_p)$ sample are shown in Fig. 5.3, for He^{+}/He^{++} ion energies from 1400 keV to 3500 keV in steps of 300 keV. From the depth resolved experimental and simulated RBS spectra, the variation of χ_{min} with depth for pristine (χ_V) and ion implanted (χ_D) samples are obtained.

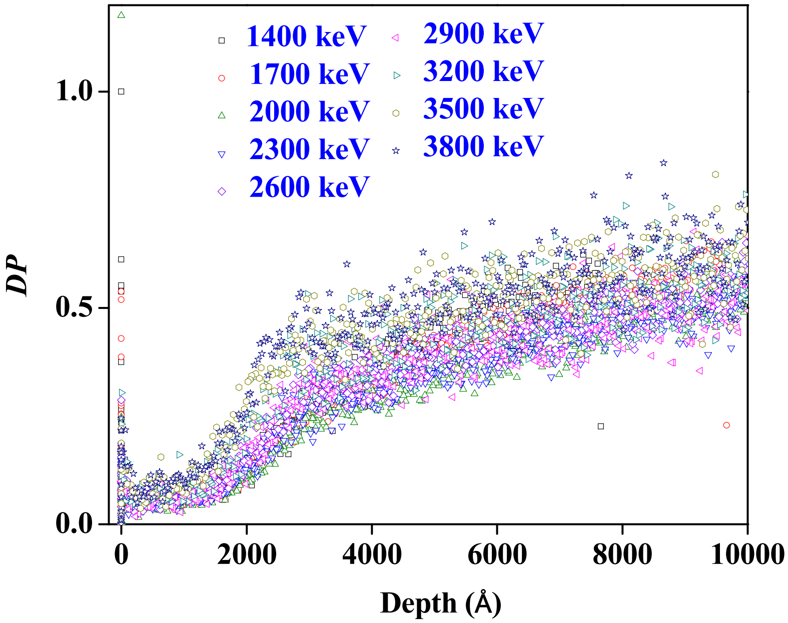

Figure 5.4 The depth resolved *DP* with different He^{+}/He^{++} ion energies from 1400 keV to 3800 keV in $Fe3(O^{18}+Cr@R_p)$ along normal axis.

The type of defects at a particular depth can be determined by energy dependence of the dechanneling parameter (*DP*) which is given by Eq. (2.10) in section 2.9 of chapter 2. The calculated *DP* up to the probing depth of He^+/He^{++} ions with various incident energies are shown in Fig. 5.4. The clear increase of dechanneling from 100 nm to 300 nm is evident for all He^+/He^{++} ion energies.

Energy dependence of dechanneling parameter (*DP*), along <100> axis of $Fe3(O^{18}+Cr@R_p)$ around the depth of 270-280 nm is presented in Fig. 5.5 (a). With linear fitting of experimental *DP* data shown in Fig. 5.4, around O^{18} ion implanted depth, the value of *d(DP)/dz* is obtained. The dechanneling parameter per unit length in the depth range of 200-300 nm (O^{18} ion range is 275±78 nm) versus $E^{0.5}$ is plotted and is shown in Fig. 5.5 (b). From the linear fit of experimental data points within error bar, $E^{0.5}$ dependence of *d(DP)/dz* is confirmed which also confirms the presence of dislocation loops. The dechanneling parameter per unit length also shows linear dependence with $E^{0.5}$ up to maximum measured ion energy of 3800 keV indicating the presence of dislocation loops. The dechanneling parameter per unit length increases linearly up to 3800 keV. Within the experimental error, there appears to be a transition closer to 3800 keV (E_s). The dislocation loop radius (R) could be determined using Kudo's [62] analysis from the relation $E_s = aR^2$. If one assumes the dislocation loops as ½ <111> loops, the obtained mean radius is greater than 23 nm. If the dislocation loops are <100> loops, the mean dislocation loop radius is 46 nm. The defect density is found to be 4.6×10^{10} dislocation loops/cm^2 for the case of <100> loops and 6.5×10^{10} dislocation loops/cm^2 for the case of ½ <111> loops, which are calculated by using Eq. (2.13). These results are similar to O^{18} and Fe^+ ion implanted Fe(110) (section 3.3).

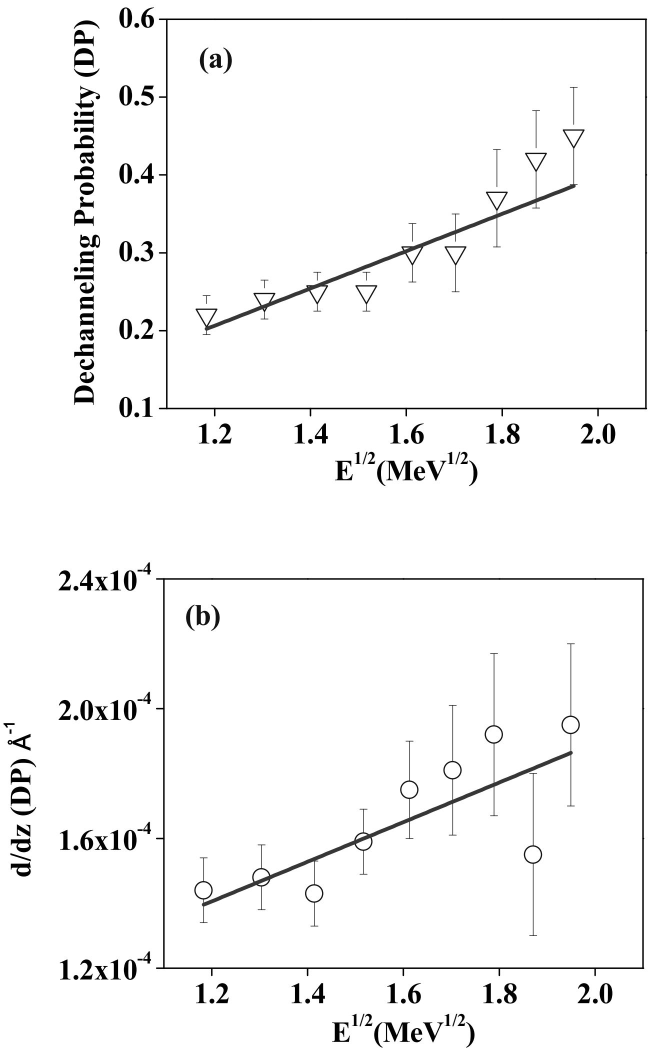

Figure 5.5 (a) Energy dependence of dechanneling parameter (*DP*) in $Fe3(O^{18}+Cr@R_p)$ along normal axis around the depth of 270-280 nm. (b) Energy dependence of dechanneling parameter per unit length measured from 200 nm to 300 nm depth.

5.4. Lattice location of Cr in ion implanted Fe(100)

The PIXE spectrum taken by 890 keV proton beam in Cr^+ ion implanted Fe(100) is shown in Fig. 5.6. The Cr signal is clearly seen from Cr-K_α and Cr-K_β peak along with Fe-K_α and Fe-K_β peaks. Both Fe and Cr yield is considerably reduced in the <100> axial direction compared to random direction. It is good to mention that the Cr signal is from surface and Fe signal is from whole range of 890 keV (6 μm) protons.

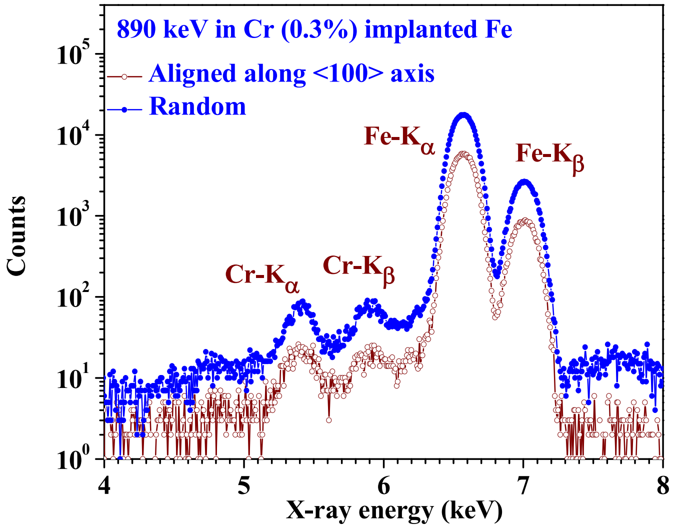

Figure 5.6 PIXE spectra of *Fe3(Cr)* (Cr^+ ion implanted bcc Fe(100)) at random and <100> axial directions.

The PIXE spectra are recorded around <100> axis and {110} plane of Cr^+ ion implanted Fe(100). The tilt angular scan is plotted by counting cumulative yields of Cr and Fe signals in PIXE spectra taken with small tilt angles. The measured tilt angular scan around <100> axis and {110} plane is shown in Fig. 5.7 (a) and 5.7 (b) respectively. The width of tilt angular scan measured along <100> axis is 0.7° and its χ_{min} is 36% for Fe. Higher value of χ_{min} in PIXE tilt angular scan is due to the signal coming from the whole probing depth of the proton beam. The width is measured to be 0.42° and χ_{min} is 70% for {110} planar scan of Fe.

For quantitative measurements, the PIXE tilt angular scans of Fe and Cr signals are simulated using FLUX7. During the simulation, the proton induced experimental cross sections for K-shell X-Ray production from reference [97] is included for both Fe and Cr signals. The experiment Fe yield is from whole proton range (6 μm) and Fe tilt angular scans are simulated for 6 μm depth of bcc Fe. For Cr tilt angular scans, SRIM concentration profile with range 280±80 nm is used. The Debye temperature of 470 K is used for Fe and

Cr which corresponds to a thermal vibration amplitude of 0.08 Å and 0.09 Å respectively. The simulated Fe and Cr tilt angular scans along <100> and {110} are shown in Fig. 5.7 (a) and 5.7 (b) respectively. The width of Fe tilt angular scan is 0.68° and 0.3° for <100> and {110} which are well matching with experiment. However width of simulated tilt angular scan is 0.8° long <100> for substitutional Cr which is higher than experimental value 0.68°.

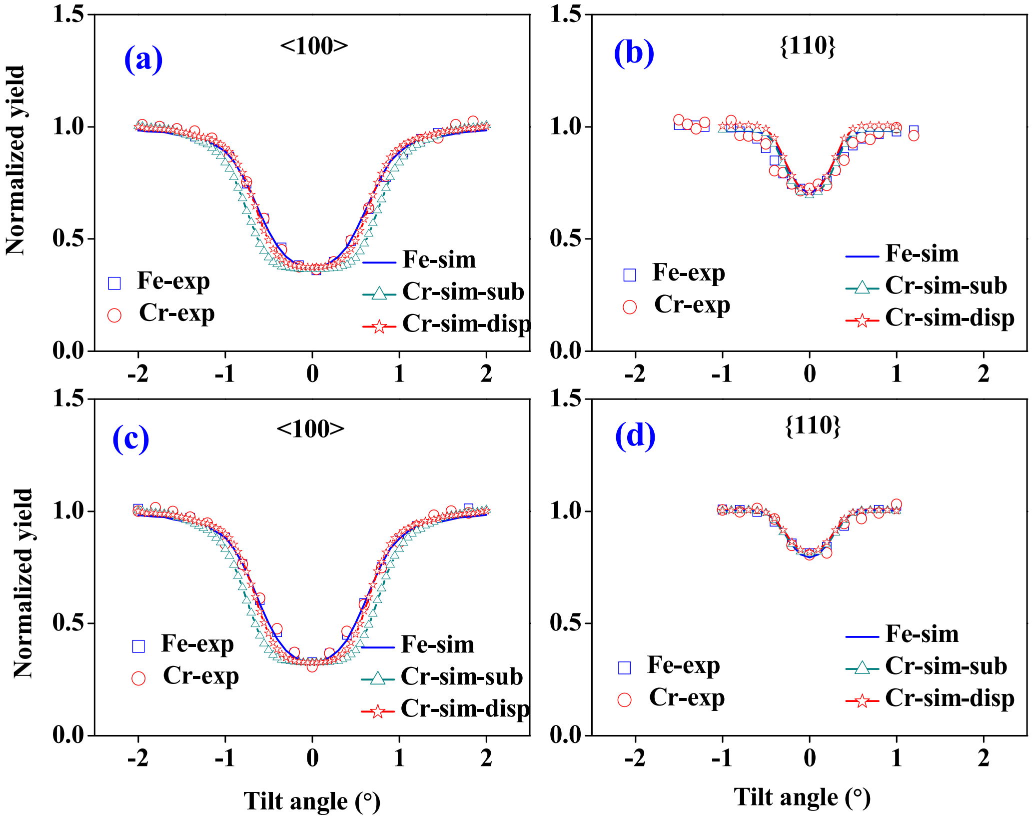

Figure 5.7 Tilt angular scans of Fe and Cr signals measured (a) along <100> axis, (b) along {110} plan of *Fe3(Cr)* and (c) along <100> axis, (b) along {110} plan of *Fe3*(O^{18}*+Cr@*R_p). Tilt angular scans of Fe and Cr is measured from PIXE experiments performed by 890 keV protons.

The width of experimental Cr tilt angular scan is matching with simulation for Cr displaced 0.15 Å along <100> from substitutional site. The {110} tilt angular scan of Cr at substitution and displaced site is similar. Substitutional site of Cr with small displacement is predicted by PIXE/channeling experiment and simulations. The experimental and simulated tilt angular scan of $Fe3(O^{18}+Cr@R_p)$ are given in Fig. 5.7 (c) and 5.7 (d) for <100> and {110} respectively. Experimental tilt angular scans given in Fig. 5.7 (c) and 5.7 (d) are similar to 5.7 (a) and 5.7 (b), which implies that the lattice location of Cr is not altered by O^{18} ion implantation and annealing.

5.5. Lattice location of O^{18} in Cr^+ and O^{18} ion implanted Fe(100)

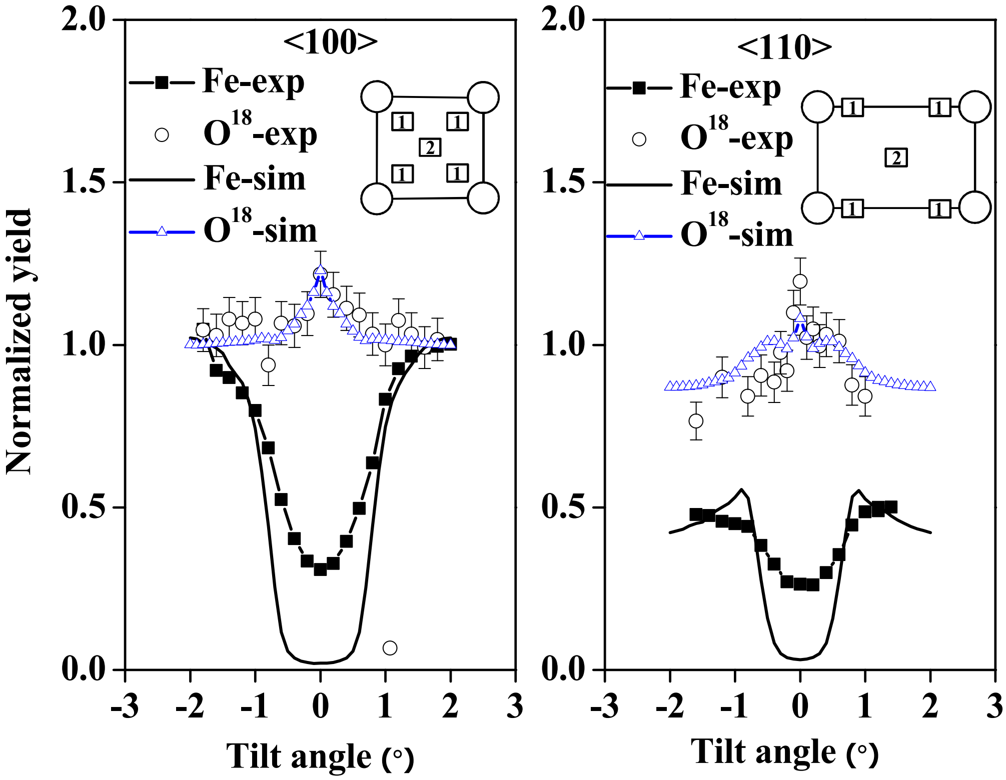

Figure 5.8 Tilt angular scans of Fe and O^{18} signals of $Fe3(O^{18}+Cr@R_p)$ along <100> and <110> axis. Tilt angular scans of Fe is measured from RBS and O^{18} is from NRA experiments performed by 850 keV protons. The projections of O^{18} at tetrahedral position in bcc Fe lattice are shown in insets.

Tilt angular scans of O^{18} from NRA and Fe from RBS are measured around <100> and <110> axis to measure the lattice location of O^{18}. The experimental and simulated tilt angular scans of Fe and O^{18} signals from $Fe3(O^{18}+Cr@R_p)$ measured by 850 keV protons are shown in Fig. 5.8. The measured χ_{min} of Fe signal is 30%, 28% along <100>, <110> axis respectively. The width of Fe tilt angular scans is 0.78° for <100> axis which is closer to simulated value of 0.82°. There are difficulties in locating the <110> off normal axis due to the presence of planar channels around this angle. So, the experimentally observed width of <110> axis is 0.55° which is small compared to simulated value of 0.67°. To match with experiment, the simulation is performed with a nearby plane in <110> axis for Fe as well as O^{18} tilt angular scans. Now the simulated width of Fe tilt angular scan is 0.58° which is closer to experimental value of 0.55°. The random fraction f_R (Eq. (2.22)) that accounts the dechanneling from defects in the matrix is 0.28, 0.25 for <100>, <110> axis respectively. From the fit by Eq. (2.21), 100% of the implanted O^{18} is found at tetrahedral interstitial position as shown in Fig. 5.8.

5.6. Positron annihilation spectroscopy studies of vacancy defects

The SPDBS measurements are done in $Fe3(O^{18}+Cr@R_p)$. The S parameter as a function of incident positron beam energy of the pristine reference sample and $Fe3(O^{18}+Cr@R_p)$ sample are shown in Fig. 5.9 (a). For pristine reference sample, $S(E)$ curve is analyzed and fitted with single layer model by using VEPFIT code, which shows S parameter of 0.513 and diffusion length of 152 nm. The ion implanted sample shows good fit of depth resolved S parameter and effective diffusion length for two layer fitting, and is shown in Fig. 5.9 (b). The spectrum is fitted by assuming two layers, where first layer is from surface to 100 nm depth and second layer is from 60 nm to 710 nm. The S parameter for first layer is 0.564 which is slightly higher than the second layer value 0.534 and the diffusion lengths in first and second layers are 14 nm and 61 nm respectively.

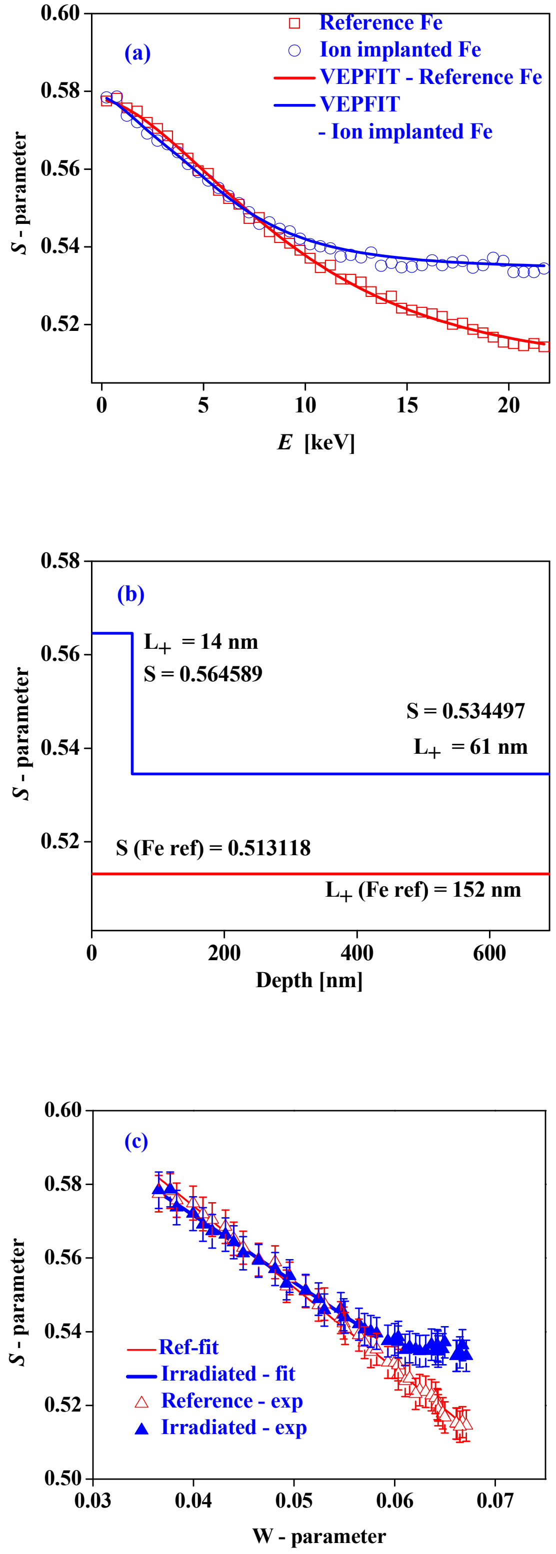

Figure 5.9 (a) The experimental and VEPFIT simulated *S* parameter as a function of positron energy, (b) Depth resolved *S* parameter and diffusion lengths and (c) *S*-*W* plot for reference Fe(100) and ion implanted Fe(100) ($Fe3(O^{18}+Cr@R_p)$).

The vacancy concentration in the assumed layer is calculated using Eq. (3.1). The calculated vacancy concentration of first and second layer is 7×10^{18} cm^{-3} and 1.2×10^{18} cm^{-3} respectively. The presence of vacancy defects at O^{18} implanted depth is confirmed by SPDBS measurements. The *S-W* plot of reference as well as $Fe3(O^{18}+Cr@R_p)$ is shown in Fig. 5.9 (c). The reference plot show linear fit and $Fe3(O^{18}+Cr@R_p)$ also show linear fit of data points. However, at higher depths, the *S-W* plot deviates from linear fit which imply that the vacancy defects formed near surface is different from defects formed at higher depth in $Fe3(O^{18}+Cr@R_p)$, which is very different from *S-W* plot of ion implanted Fe(110) used in chapter 3 and ion implanted Fe(100) used in chapter 4.

5.7. DFT study of Cr and O interactions with interstitial defects in Fe

In order to find the defect structure, oxygen interactions with interstitial and vacancy defects in bcc Fe is studied in chapters 3 and 4. Here, O^{18} is found at tetrahedral interstitial site in $Fe3(O^{18}+Cr@R_p)$ by ion channeling measurement. The tetrahedral interstitial site of O^{18} is due to trapping at interstitial dislocation loop which is well understood from chapter 3. In addition to this, the experimental results show 0.15 Å displacement of Cr which is implanted at same depth profile of O^{18} in same crystal. To understand this experimental result, DFT calculations are performed in bcc Fe. First the interactions and lattice location of Cr in presence of mono (I_1) and di-interstitial (I_2) defects are studied to compare with experimental values. The studied defects are shown in Fig. 5.10. The computed formation energies of most stable mono interstitial (<110> dumbbell), di-interstitial with parallel dumbbell configuration and di-interstitial with planar configuration are 4.08 eV, 7.52 eV and 7.37 eV respectively which are compared with literature values and given in Table 5.1. For di-interstitial defect, the computational results show lower formation energy for planar structure compared parallel dumbbell structure in agreement to literature. In order to compare with experiment the binding energy and lattice location of Cr is studied with mono and di-interstitial defects.

Table 5.1 Formation energy of self interstitial clusters in bcc Fe.

Defect type	Defect structure	Formation energy (eV)	
		Present study	Others
Mono interstitial	<110> dumbbell	4.08	4.02 [Ref. 87]
Di-interstitial	Two parallel <110> dumbbells	7.52	7.55 [Ref. 23], 7.15 [Ref. 22]
	Triangular ring around <111> plane	7.37	7.45 [Ref. 23], 7.04 [Ref. 22]

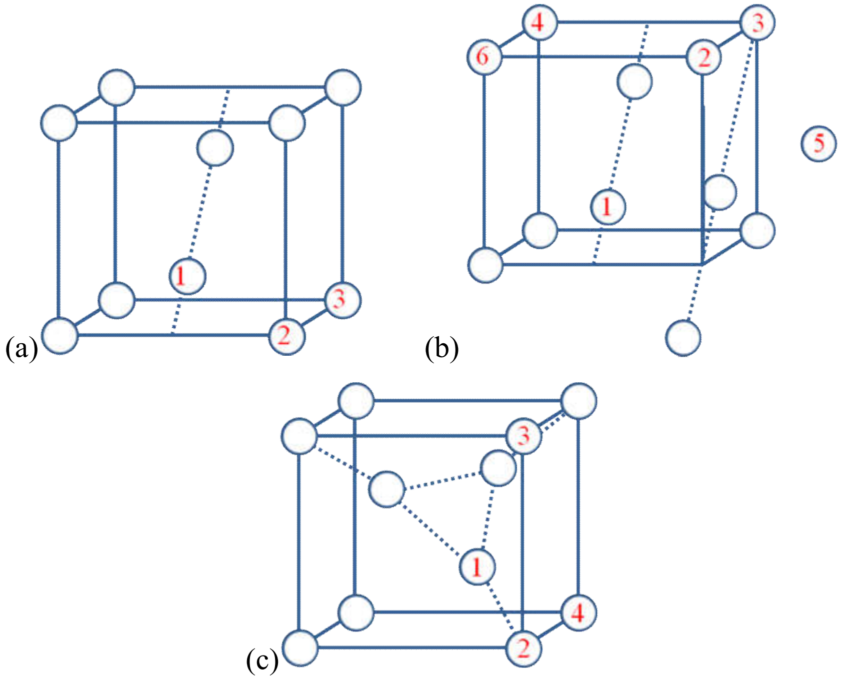

Figure 5.10 Schematic diagram shows (a) mono interstitial defect with <110> dumbbell configuration and di-interstitial with (b) parallel dumbbell configuration, (c) planar configuration. The studied Cr positions are marked as 1, 2,..etc.

The interactions of Cr with defect sites of <110> dumbbell (labeled as 1, 2, 3 in Fig. 5.10 (a)) is studied. The calculated binding energy of Cr and its lattice location at various defect configurations are given in Table 5.2. For <110> dumbbell, Cr strongly binds in *I_1-<110>-Cr(1)* configuration and forms Cr mixed dumbbell structure. Binding energy of Cr in mixed <110> dumbbell is calculated to be 0.078 eV which is comparable with literature value of 0.08 eV reported by Klaver *et al.*, [98]. The binding energy of Cr at site-2 is 0.053 eV while at site-3, it is repulsive with the binding energy of -0.058 eV. In the most sable <110> mixed dumbbell the lattice location of Cr is found to be displaced 0.7 Å along <110> from substitutional site which is much different than the experimental value. Hence the experimentally observed Cr displacement from substitutional site in *Fe3(Cr)* is not from Cr mixed <110> dumbbell.

The interactions of Cr at various sites of the di-interstitial defect with parallel dumbbell configuration are studied by calculating the binding energy of Cr. The schematic diagram of di-interstitial and Cr positions studied (labeled as 1, 2, 3, 4, 5, 6) in the parallel dumbbell configuration as well as planar configuration are shown in Fig. 5.10 (b) and 5.10 (c) respectively. For parallel dumbbell configuration, positive binding energy (0.04 eV) is observed only in case of I_2-*<110>-Cr(1)* cluster. The lattice location of Cr is found at 0.67 Å displaced along <110> from substitutional site like mixed <110> dumbbell configuration.

Table 5.2 Chromium interactions with self interstitial defects.

Defect structure	**Binding energy of Cr**	**Cr lattice location**
I_1-*<110>-Cr(1)*	0.078 eV	0.7 Å displaced along <110> from substitutional site
I_1-*<110>-Cr(2)*	0.053 eV	0.3 Å displaced along <100> from substitutional site
I_1-*<110>-Cr(3)*	-0.058 eV	Substitutional site
I_2-*<110>-Cr(1)*	0.04 eV	0.67 Å displaced along <110> from substitutional site
I_2-*<110>-Cr(2)*	-0.007 eV	0.4 Å displaced along <110> from substitutional site
I_2-*<110>-Cr(3)*	-0.006 eV	0.3 Å displaced along <100> from substitutional site
I_2-*<110>-Cr(4)*	-0.059 eV	Substitutional site
I_2-*<110>-Cr(5)*	-0.007 eV	0.4 Å displaced along <110> from substitutional site
I_2-*<110>-Cr(6)*	-0.079 eV	Substitutional site
I_2-*{111}-Cr(1)*	-0.075 eV	1 Å displaced along <111> from substitutional site
I_2-*{111}-Cr(2)*	0.108 eV	0.78 Å displaced along <111> from substitutional site
I_2-*{111}-Cr(3)*	-0.075 eV	Substitutional site
I_2-*{111}-Cr(4)*	-0.087 eV	0.2 Å displaced along <110> from substitutional site

For planar configuration of I_2, the binding energy of Cr placed at sites 1, 3, 4 is -0.078 eV, -0.078 eV, -0.087 eV respectively. In contrast to Cr mixed <110> dumbbell configuration, where Cr binds with the interstitial site, Cr interaction is repulsive with interstitial sites of I_2. The positive average binding energy of Cr is found only in case of Cr placed at site-2. The binding energy of Cr at site-2 is 0.108 eV which is 0.03 eV higher than the mixed dumbbell configuration. The lattice site of Cr in the most stable Cr-planar di-interstitial is displaced 0.78 Å along <111> from substitutional site. These values are also not matching with experiment. Hence, the DFT results of Cr mixed small interstitial defects are not observed in this crystal.

In addition to the studies of lattice site location of Cr in the defects, it is observed that the magnetic interactions are playing important role (in addition to other effects) in the Cr mixed interstitial cluster. For planar di-interstitial cluster, systematic change of magnetic moments upon substituting Cr in defective region is observed. The magnetic moment of atoms around a planar di-interstitial is shown in Fig. 5.11. The magnetic moments of interstitial atoms (denoted as *M* in Fig. 5.11) are negative. Atoms at tensile (denoted as *T* in Fig. 5.11) regions have magnetic moments of 2.53 μ_B. The magnetic moment of Fe atoms at compressive sites (denoted as *C* in Fig. 5.11) is reduced considerably compared to defect free atoms (2.2 μ_B).

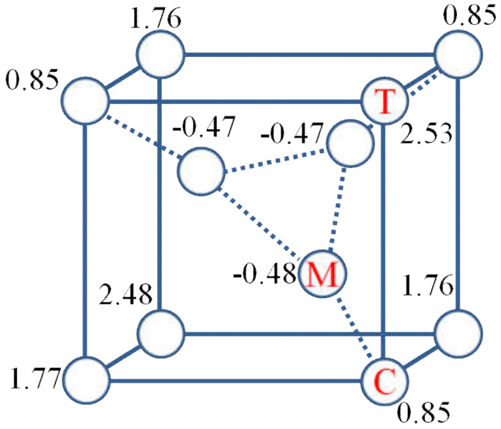

Figure 5.11 DFT predicted magnetic moment of Fe atoms around the di-interstitial defect with planar configuration. Sites *T*, *M* and *C* represent tensile, mixed and compressive configurations respectively.

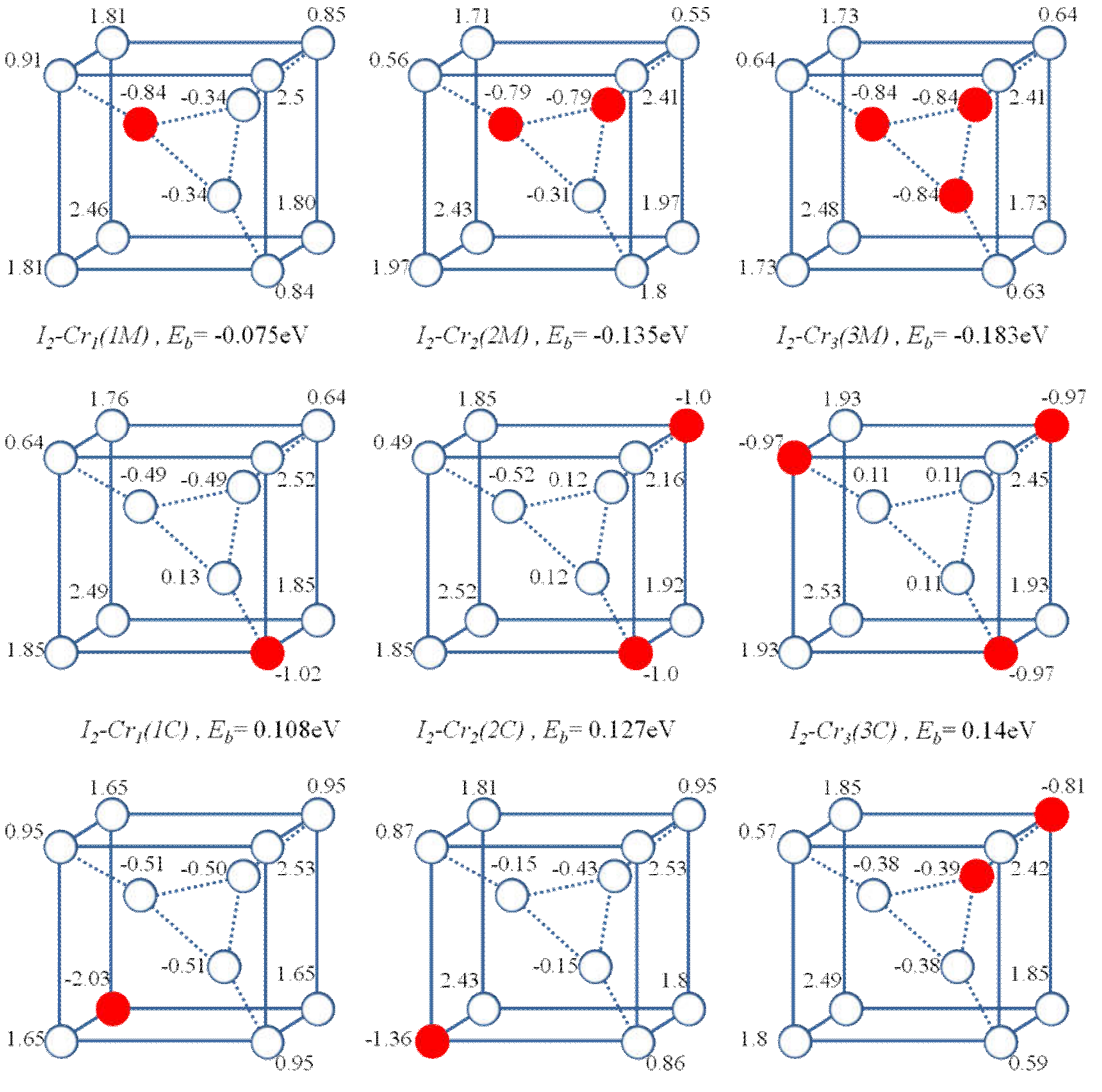

I_2-$Cr_1(1M)$, E_b= -0.075eV I_2-$Cr_2(2M)$, E_b= -0.135eV I_2-$Cr_3(3M)$, E_b= -0.183eV

I_2-$Cr_1(1C)$, E_b= 0.108eV I_2-$Cr_2(2C)$, E_b= 0.127eV I_2-$Cr_3(3C)$, E_b= 0.14eV

I_2-$Cr_1(1T)$, E_b= -0.075eV I_2-$Cr_1(1S)$, E_b= -0.087eV I_2-$Cr_2(1C\text{-}1M)$, E_b= -0.19eV

Figure 5.12 Schematics of defect structures containing Cr in I_2 clusters, (a) 1 Cr at *M* (I_2-$Cr_1(1M)$), (b) 2 Cr at *M* (I_2-$Cr_2(2M)$), (c) 3 Cr at *M* (I_2-$Cr_3(3M)$), (d) 1Cr at *C* (I_2-$Cr_1(1C)$), (e) 2 Cr at *C* (I_2-$Cr_2(2C)$), (f) 3 Cr at *C* (I_2-$Cr_3(3C)$), (g) 1 Cr at *C* and 1 Cr at nearest *M* (I_2-$Cr_2(1C\text{-}1M)$), (h) 1 Cr at *T* (I_2-$Cr_1(1T)$), (i) 1 Cr at *S* (I_2-$Cr_1(1S)$). The open circle represents Fe atom while solid circle denotes Cr atom. Individual magnetic moments of Fe and Cr atoms are shown in units of μ_B. The average binding energy of Cr is shown for each structure.

The magnetic moments of Cr and Fe atoms around the Cr mixed planar di-interstitial defect is shown in Fig. 5.12. For point defect clusters, one can calculate two types of binding energies, one is incremental binding energy and another one is average binding energy [38,99]. The incremental binding energy of p^{th} Cr with defect cluster containing *(p-1)* Cr in self-interstitial cluster (I_q) is defined by,

$$E_b^{inc} = E(Cr_{p-1}I_q) + E(Cr) - E(Cr_pI_q) - E_o \tag{5.1}$$

where $E(Cr_pI_q)$ and $E(Cr_{p-1}I_q)$ is energy of cell containing p and *(p-1)* Cr with I_q, respectively. $E(Cr)$ is the energy of cell containing Cr in substitutional site and E_o is the energy of defect-free cell. The average binding energy of Cr in defect configurations containing p^{th} Cr in self-interstitial cluster is given by,

$$E_b^{ave} = \frac{1}{p}[E(I_q) - E(Cr_pI_q)] + E(Cr) - E_o \tag{5.2}$$

The total binding energy is a product of average binding energy and number of Cr atoms. In this equation, positive binding energy represents the energy lowering attraction of Cr with defect. The defect structures and DFT calculated average binding energies are shown in Fig. 5.12.

Substitution of Cr atoms at interstitial sites (denoted as *M* in Fig. 5.11) result in increase of system energy and repulsive interaction is observed. The repulsive interaction is increased upon substitution of Cr up to 3 atoms at *M* site (Fig. 5.13 (a), 5.13 (b) and 5.13 (c)). In contrast to substitution at site-*M*, substitution of Cr atoms at site *C* is found to be attractive. The incremental binding energy of 1st Cr substituted at site *C* is found to be 0.108 eV. The increase of incremental binding energy is observed up to 0.2 eV for 1st to 3rd Cr atom at site-*C* which is seen in Fig. 5.13 (d), 5.13 (e) and 5.13 (f). At site *C*, Cr interacts antiferromagnetically with substitutional Fe atoms and the magnetic moment of nearest interstitial Fe atom is changing from -0.47 μ_B to 0.13 μ_B. The magnetic moment of interstitial Fe atom changes from negative to positive upon substituting 2nd and 3rd Cr atom also at site *C*. These imply that there is a clear influence of magnetic interactions on binding energy of Cr with interstitial defects, in addition to other effects like solute size factor, electronic structure etc.

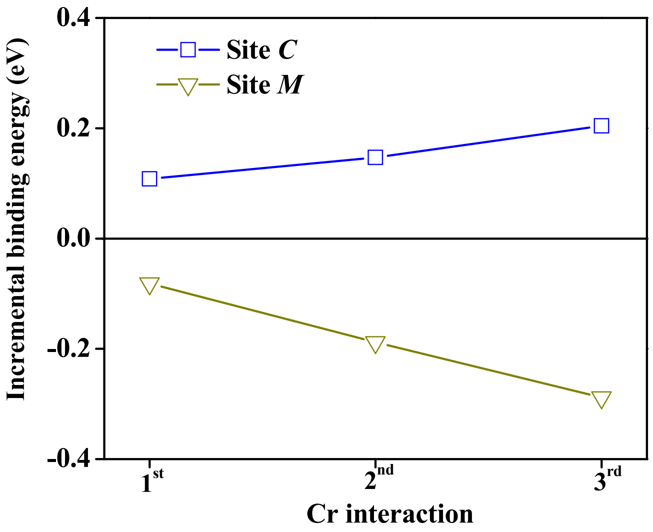

Figure 5.13 Incremental binding energies of Cr atom at site *C* and site *M* in the planar di-interstitial defect.

In chapter 3, O^{18} is found at tetrahedral interstitial position (experimentally) in O^{18} ion implanted Fe and similar oxygen position is identified using DFT calculations for the interaction of oxygen with interstitial dislocation loop structure. In this sample also the interstitial dislocation loops could be dominant defect formed during Cr^+ and O^{18} ion implantation at same depth and annealing. In this sample also O^{18} is found at tetrahedral interstitial site, which implies that the O^{18} is segregated on interstitial dislocation loops. To better understand Cr interactions with interstitial dislocation loops in iron, the interactions of Cr atom with few atom dumbbell cluster in the form of ½ <111> and <100> dislocation loop structure is studied by using DFT calculations. The ½ <111> interstitial dislocation loop structure is found to collapse during ionic relaxation at fixed volume. However, the four atom <100> interstitial dislocation loop structure (shown in Fig. 5.14) is found to be stable after ionic relaxation, which is used for further studies of Cr and O interactions with <100> interstitial dislocation loop. The Cr atom is substituted in the defective region as mentioned in Fig. 5.14 (numbers 1 to 7 indicate position of Cr) and total energy calculations are performed with fixed volume. The calculated binding energies and the lattice location of Cr in each defect configurations are shown in Table 5.3.

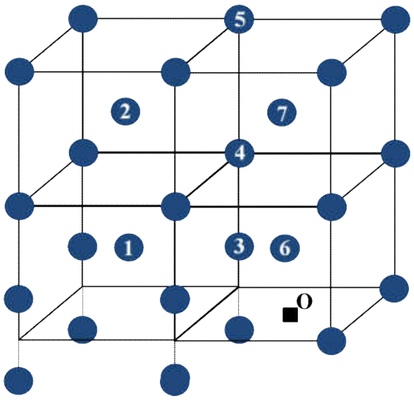

Figure 5.14 Schematic of four atom <100> interstitial dislocation loop structure in bcc Fe. Solid circle and solid square represent Fe atom and oxygen atom respectively. The studied Cr positions are marked from 1 to 7.

Table 5.3 DFT predicted binding energy of Cr and O with interstitial dislocation loops and lattice location of Cr in the defect cluster.

Defect structure	**Binding energy of Cr**	**Cr lattice location**
I_4-<100>-Cr(1)	0.4 eV	1.2 Å displaced along <100> from substitutional site
I_4-<100>-Cr(2)	0.7 eV	0.4 Å displaced along <100> from substitutional site
I_4-<100>-Cr(3)	-	-
I_4-<100>-Cr(4)	-	-
I_4-<100>-Cr(5)	-	-
I_4-<100>-Cr(6)	-	-
I_4-<100>-Cr(7)	-	-
I_4-<100>-O-Cr(1)	-	-
I_4-<100>-O-Cr(2)	-	-

All structures are found to collapse except I_4-*<100>-Cr(1)* and I_4-*<100>-Cr(2)* cluster. The DFT calculations of I_4-*<100>-Cr(1)* and I_4-*<100>-Cr(2)* cluster in presence of an oxygen atom is performed with atomic positions as illustrated in Fig. 5.14. These structures are found to be unstable during ionic relaxation. The binding energy of Cr with I_4-*<100>-Cr(1)* and I_4-*<100>-Cr(2)* is found to be 0.4 eV and 0.7 eV respectively. The displacement of Cr from substitutional site is 1.2 Å, 0.4Å for *I_4-<100>-Cr(1)*, *I_4-<100>-Cr(2)* respectively. The DFT predicted displacement of 0.4 Å is comparable with experimentally observed displacement of 0.15 Å. This result shows that the Cr is trapped at interstitial dislocation loops.

The DFT results show that the weak attractive interaction of oxygen (binding energy 0.24 eV) with interstitial dislocation loops and strong attractive interaction of Cr solute (binding energy 0.7 eV) with interstitial dislocation loops and the O and Cr decorated interstitial dislocation loops are stable in the microstructure of ion implanted and annealed Fe crystal. The vacancy concentration at O^{18} depth in $Fe3(O^{18}+Cr@R_p)$ is higher compared to O^{18} and Fe ion implanted Fe(110) and Fe(100). However, the lattice location and DFT studies show strong evidence of binding of O and Cr with interstitial dislocation loops. This suggests that the Cr and O^{18} segregated interstitial loops could be formed during damage cascade itself.

5.8. Conclusion

The Cr atoms are found to be displaced 0.15 Å along <100> from substitutional site and O atoms are found at tetrahedral interstitial site in presence of self interstitial defects in iron. The interactions of Cr and O with interstitial dislocation loop structures are studied by DFT calculations and the lattice site location of Cr and O is studied within the defect structure. Good agreement with experiment is observed. Formation of Cr and O segregated interstitial dislocation loops could be responsible for the displacement of Cr and O from their equilibrium lattice sites. The positron annihilation spectroscopy studies show high concentration of vacancies at O^{18} depth. However O^{18} is found to bind with interstitial dislocation loops.

Chapter 6

Interactions of oxygen and chromium with interstitial and vacancy defects in FeCr alloy

It is well known that the void swelling is less in FeCr (typically 8-15 atomic percentage of Cr) compared to Fe during radiation damage [92]. Understanding the role of Cr in FeCr alloy under neutron/ion implantation is important to find a better strategy in structural material designing. In this regard, there are many experimental and theoretical studies have been reported in FeCr alloy in the recent years [100-118]. Comparison of radiation damage in Fe and FeCr alloy is reported in literature by experiments [100] and computer simulations [101]. The dislocation loop density and dislocation loop size in ion implanted Fe and FeCr model alloys are examined by TEM analysis and the defect density is found to be high in FeCr alloy due to pinning of defects by Cr atoms [100]. The resistivity recovery experiments show multiple trapping of interstitial clusters by Cr solutes at the concentrations of 5-15% [102]. Presence of C impurities is found to suppress the Cr clustering with interstitial defects in FeCr alloy [46]. These experimental results show strong proof of competing interactions of Cr with interstitial solutes. Hence, it influence the defect kinetics, the radiation induced microstructure is modified. To understand the O and Cr interactions with defects, in chapter 5, O and Cr ions are implanted in Fe(100). However Cr concentration is very small. To better understand the competing interactions of Cr and O with interstitial and vacancy defects in bcc FeCr, in this chapter, the lattice location of O^{18} in ion implanted and annealed Fe15%Cr alloy is studied by ion channeling analysis and the corresponding defect structure is studied by using DFT calculations.

The reason for choosing this concentration of Cr is as follows. The solubility of Cr in FeCr alloy is dependent on temperature, alloying technique and annealing time [119]. At 300ºC, 8% of Cr is soluble in Fe [120]. At high temperatures the whole range of chromium concentration is soluble as seen in the FeCr phase diagram (Fig. 6.1) [121]. But Cr concentration in the range of 8 to 12% and less than 20% are of interest in metallurgy as the void swelling is less and we can use the γ to α phase transitions for nucleating different grain structures.

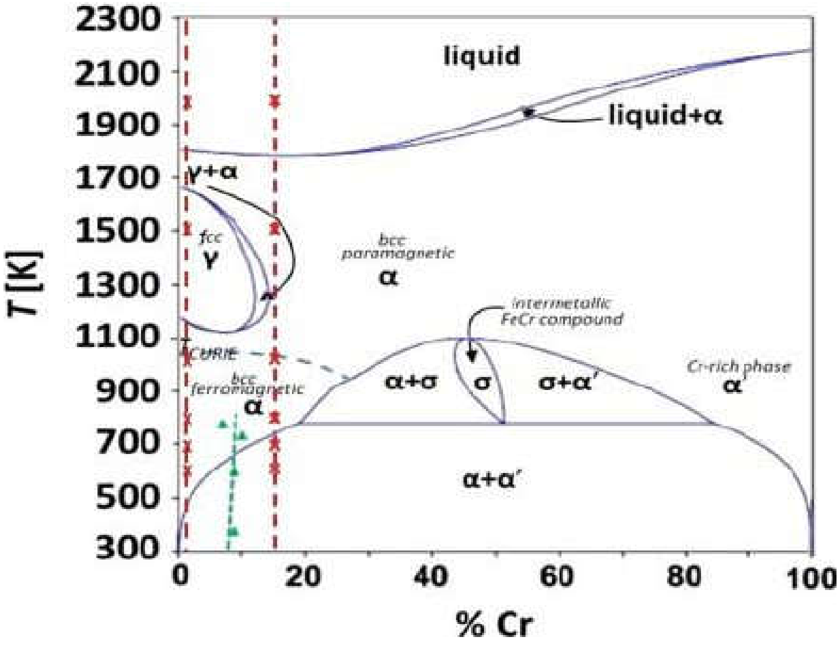

Figure 6.1 Phase diagram of FeCr alloy from reference [121].

6.1. Introduction of O and defects by ion implantation in FeCr alloy

A high purity bcc FeCr(100) crystal with 15 atomic % of Cr is implanted with 300 keV O^{18} ions with the ion fluence of 5×10^{15} ions/cm^2 at random directions in room temperature. Sample is annealed *in-situ* in vacuum of 2×10^{-7} mbar at 400 °C for 30 minutes. Here after this sample is called as *FeCr(*O^{18}*)*. The projected range (R_p) and straggling of O^{18} is 280 nm and 90 nm respectively obtained from SRIM calculations [54]. In Gaussian profile of O^{18}, the concentration is around 0.2% at peak position. The lattice location of O^{18} is measured. To introduce vacancy at O^{18} depth, the sample is irradiated 1550 keV Fe^+ ions at room temperature, with ion fluence of 1×10^{16} ions/cm^2, which is having twice the projected range of O^{18}. The sample is subsequently annealed *in-situ* in vacuum of 2×10^{-7} mbar at 400 °C for 30 minutes. This sample is called as *FeCr(*O^{18}*+Fe@2*R_p*)*. The calculated (using SRIM) ion and vacancy profiles of 1550 keV Fe^+ and 300 keV O^{18} ions are presented in Fig. 6.1. More vacancies will be present at O^{18} depth ($R_p/2$ of 1550 keV Fe^+ ions). The lattice location of O^{18} is measured again. The calculated damage level during O^{18} implantation is 3.5 dpa which is increased to 9.3 dpa after self ion implantation.

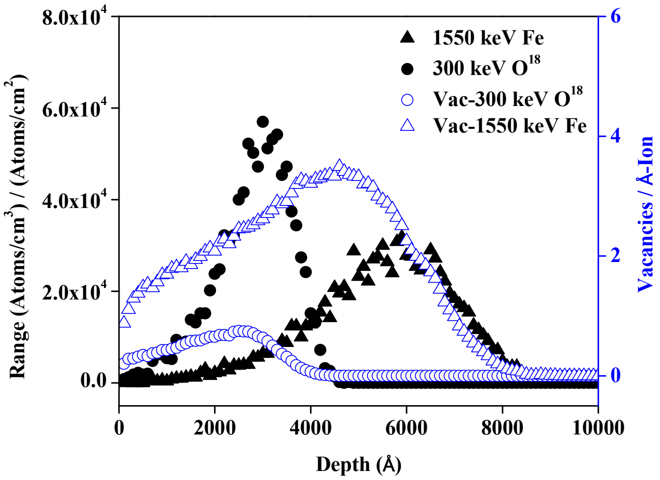

Figure 6.2 Calculated (using SRIM) ion range and vacancy concentration profiles of 300 keV O^{18} ions and 1550 keV Fe^+ ions in Fe15%Cr.

6.2. Range of defects by RBS/channeling

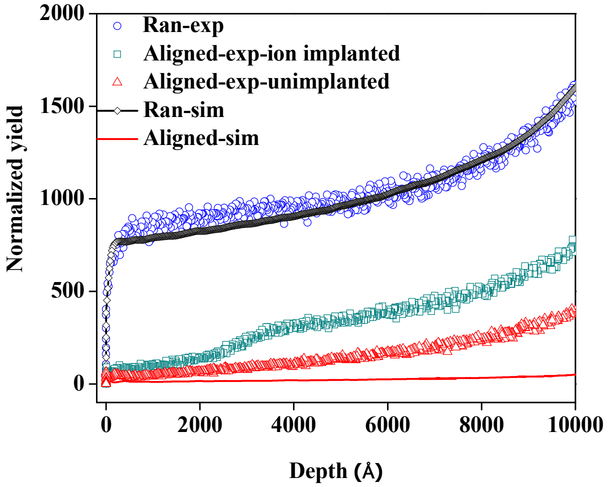

Figure 6.3 Depth converted experimental RBS spectra of pristine and *FeCr(*O^{18}*)* crystal taken by 2 MeV He^+ ions along <100> axis. The simulated RBS spectra of <100> axial and random directions of ideal Fe15%Cr is given for comparison.

The depth converted RBS spectra taken along random and <100> axial direction of pristine and $FeCr(O^{18})$ sample by 2 MeV He^+ ions are shown in Fig. 6.2. The FLUX7 simulated RBS spectra of pristine Fe along <100> axis and random directions are shown for comparison. The value χ_{min} measured at 50 nm depth is 6 % in pristine crystal. A clear dechanneling can be seen from 200 nm to 300 nm in $FeCr(O^{18})$ due to defects, which suggest that more defects are produced and survived around O^{18} implanted depth.

6.3. Type of defects by energy dependant dechanneling measurements

Energy dependent channeling measurements are carried out to study the type of defects present at O^{18} implanted depth. The RBS measurements are done using He^+/He^{++} ion beam with energy varying from 1100 keV to 3500 keV along <100> axis and random directions.

The RBS spectra are simulated at random and <100> axial directions using FLUX7 program for all incident energies. The random experimental data is matched with simulation and experimental spectra of random and <100> axial direction are converted to depth *vs* yield. The depth converted experimental and simulated RBS spectra at <100> axis aligned and random direction of $FeCr(O^{18}+Fe@2R_p)$ crystal are shown in Fig. 6.3 for He^+/He^{++} ion energies from 1400 keV to 3500 keV in steps of 300 keV. From the depth converted experimental and simulated RBS spectra, the variation of χ_{min} with depth for pristine (χ_V) and ion implanted (χ_D) samples are obtained.

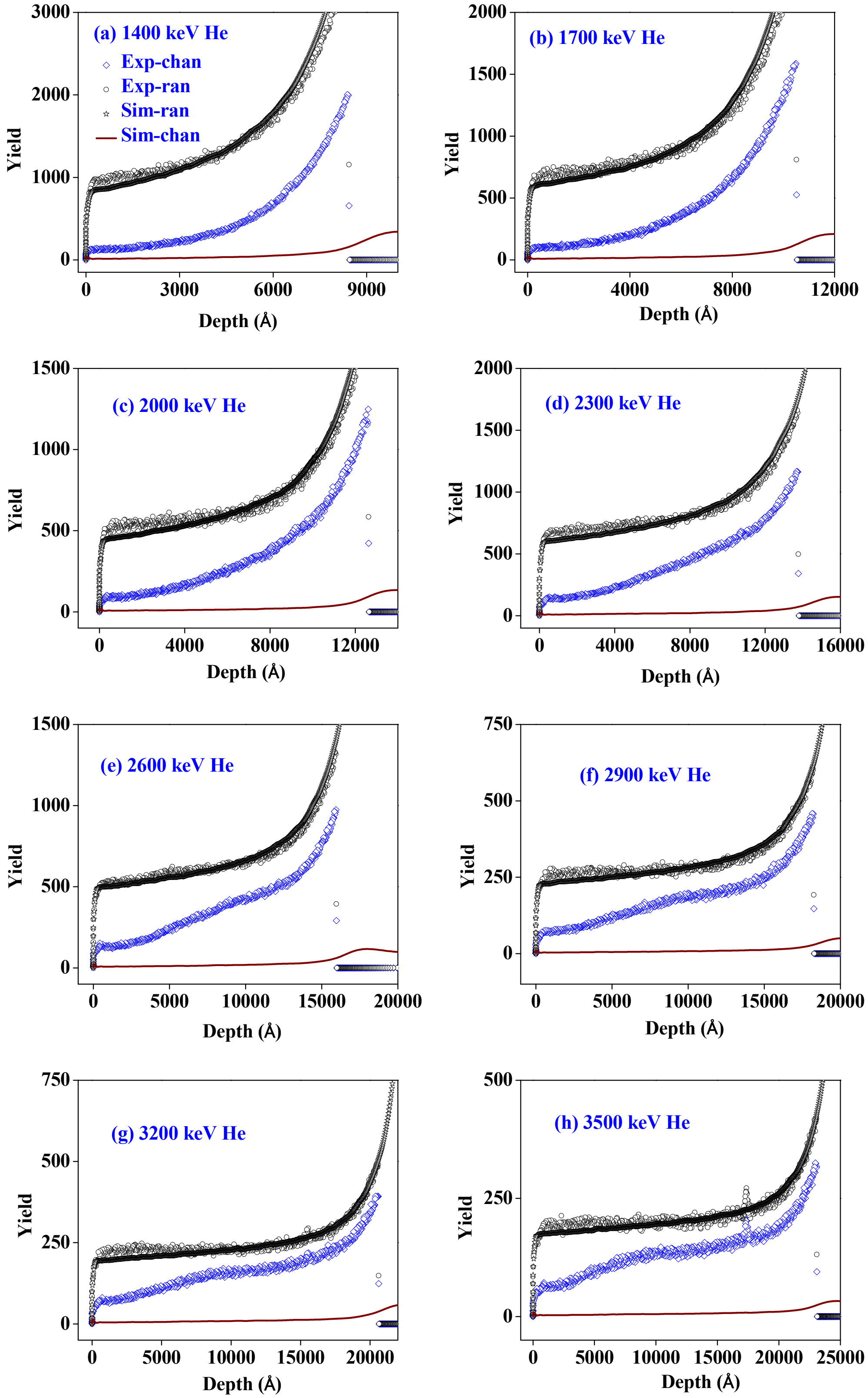

Figure 6.4 The depth converted experimental and simulated RBS spectra of *FeCr*(O^{18}+*Fe@2*R_p) with He^+/He^{++} ion energy of (a) 1400 keV, (b) 1700 keV, (c) 2000 keV, (d) 2300 keV, (e) 2600 keV, (f) 2900 keV, (g) 3200 keV and (h) 3500 keV.

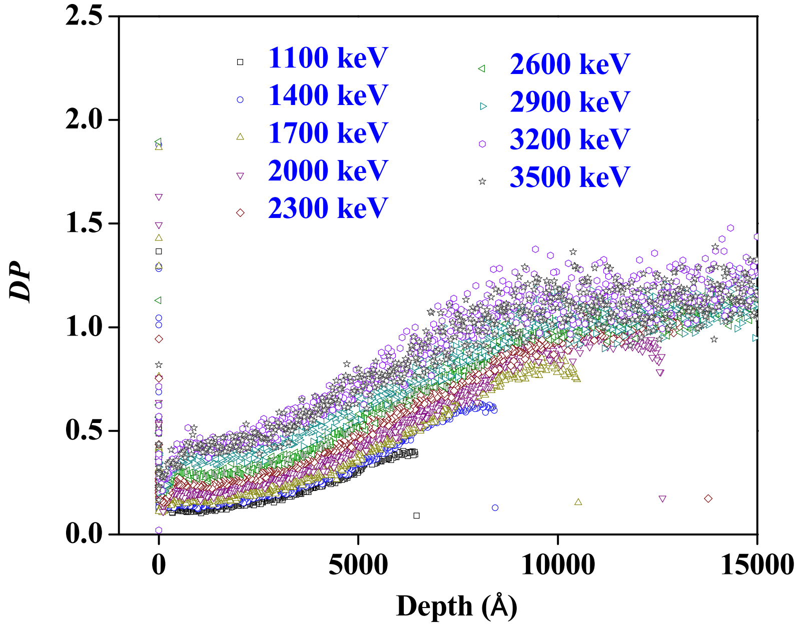

Figure 6.5 The depth resolved *DP* measured in $FeCr(O^{18}+Fe@2R_p)$ with various He^+/He^{++} ion energies from 1100 keV to 3500 keV in steps of 300 keV.

The type of defects at a particular depth can be determined by energy dependence of the dechanneling parameter (*DP*) which is given by Eq. (2.10) in section 2.9 of chapter 2. The calculated *DP* up to the probing depth of He^+/He^{++} ions with various incident energies are shown in Fig. 6.4. From 200 nm to 800 nm, the dechanneling parameter has increased as clearly evident from the spectra of $FeCr(O^{18}+Fe@2R_p)$ (Fig. 6.4), due to 1550 keV Fe^+ ion implantation. However, experimental *DP* data shown in Fig. 6.4 is fitted with linear function to measure *d(DP)/dz* value around O^{18} ion implanted depth.

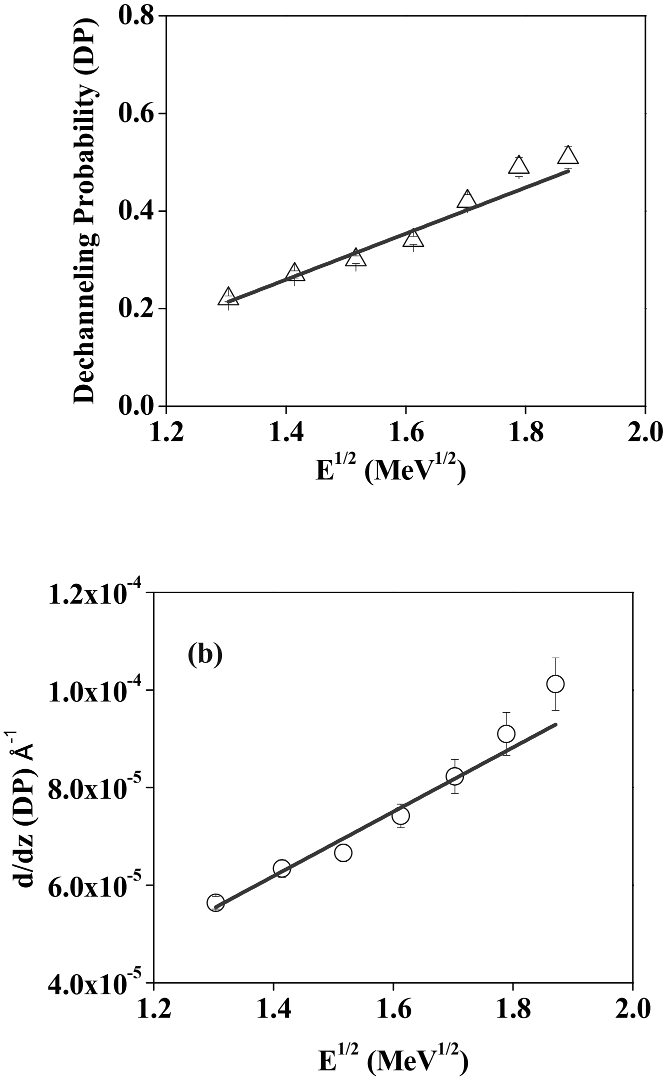

Figure 6.6 (a) Energy dependence of dechanneling parameter (*DP*) from 270-280 nm depth, (b) Energy dependence of *DP* per unit depth measured from 200-400 nm by He^+/He^{++} ions with 1100 keV-3500 keV energy in $FeCr(O^{18}+Fe@2R_p)$.

The He^+/He^{++} ion energy dependence of dechanneling parameter (*DP*), along normal axis of $FeCr(O^{18}+Fe@2R_p)$ around the depth of 270-280 nm, is shown in Fig. 6.5 (a). The linear fit of experimental data points shows $E^{0.5}$ dependence of *DP* which confirms the presence of dislocations. The dechanneling parameter per unit length in the depth range of 200-400 nm (O^{18} ion range; 275±78 nm) versus $E^{0.5}$ is plotted as in Fig. 6.5 (b) which shows linear dependence up to maximum measured ion energy of 3500 keV indicating the presence of dislocation loops. From Kudo's [62] analysis, the obtained mean radius is greater than 23 nm if one assumes ½ <111> loops and if one assumes the dislocation loops as <100> the mean dislocation loop radius will be greater than 45 nm. The defect density of dislocation loops is calculated from the slope of linear fitting shown in Fig. 6.5 (b) using Eq. (2.13). The same value of ψ_1 calculated by using Eq. (2.15), for 2 MeV He^+ ions in bcc Fe crystal is used in FeCr crystal also. The observed defect density is 3.8×10^{10} dislocation loops/cm^2 for the case of <100> loops and 5.3×10^{10} dislocation loops/cm^2 for the case of ½ <111> loops.

6.4. Lattice location of O^{18} ion implanted in FeCr(100) alloy

The experimental and simulated tilt angle dependence of host (Fe+Cr) and O^{18} signal in *FeCr(*O^{18}*)* is given in Fig. 6.6 (a) and 6.6 (b) along <100> and <110> axes respectively. For the simulation of host FeCr signal 15% of Cr atoms are added at substitutional position of bcc Fe lattice. The Debye temperature of Fe and Cr are taken as 470 K. The experimental χ_{min} of FeCr tilt angular scan performed along <100> axis is 8% and <110> axis is 38%. Angular width of host experimental scans performed along <100>, <110> are 0.8°, 0.77° which are comparable to the simulated values of 0.82°, 0.7° respectively.

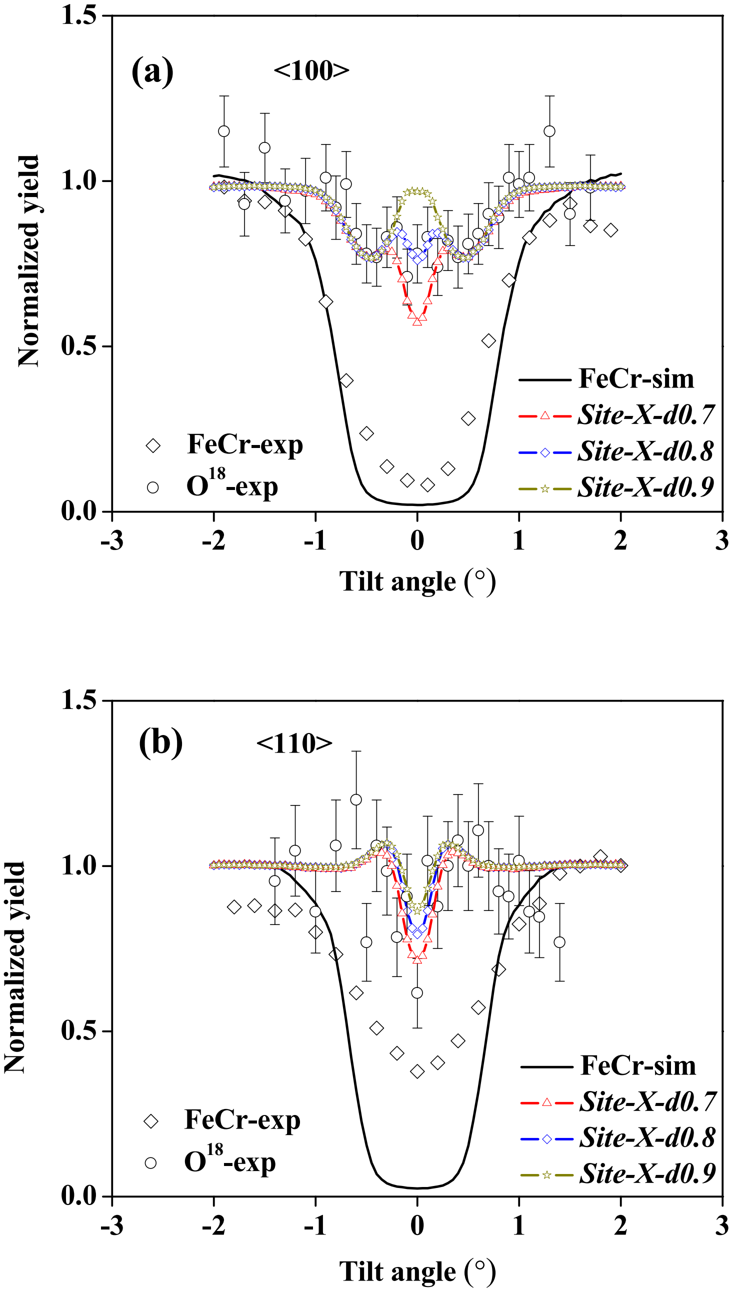

Figure 6.7 Experimental and simulated tilt angular scans of Fe+Cr and O^{18} signals in *FeCr(O^{18})* sample along (a) <100> and (b) <110> axis.

In all the experiments, O^{18} signal is not following the host signal, indicating that its lattice location is not substitutional site. The O^{18} signal is simulated for all standard sites of bcc crystal and compared with experiment. The best fit is obtained for the case of off-centered site *X* (shown in Fig. 6.7), which is displaced along <100> from octahedral as shown in

Fig. 6.6 (a) along <100> and Fig. 6.6 (b) along <110> axis. The projection of the site *X* along <100>, <110> is shown in Fig. 6.8, which are used to simulate the O^{18} impurity tilt angular scans using FLUX7 program. Simulated scan *site-X-d0.8* (displaced 0.8 Å from substitutional to nearest octahedral site in other words displaced 0.63 Å along <100> from octahedral interstitial site) is matching with experimental scan performed along <100> and <110>. Simulated scans *site-X-d0.7* and *site-X-d0.9* is shown for comparison. Within our experimental error bar, the displacement of the site could be 0.63 Å along <100> from octahedral interstitial site within an error of 0.1 Å. The random fraction f_R (Eq. (2.22)) that account the dechanneling from defects in the matrix is 0.06, 0.36 for <100>, <110> axes respectively. In the fitting of simulated scans with experiment using Eq. (2.21), no additional fraction of random yield is added in all the simulation of O^{18} scans, these indicates all O^{18} ions are at *site-X-d0.8*.

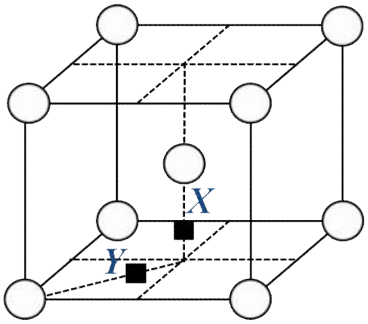

Figure 6.8 Lattice location of site *X* and site *Y* in bcc system.

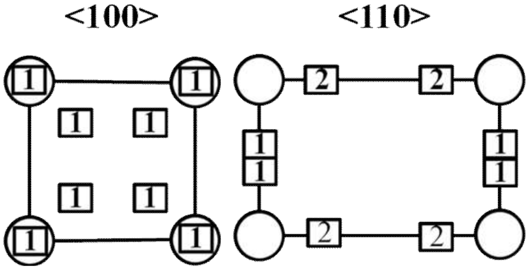

Figure 6.9 Projection of site *X* in bcc system along <100> and <110> axis.

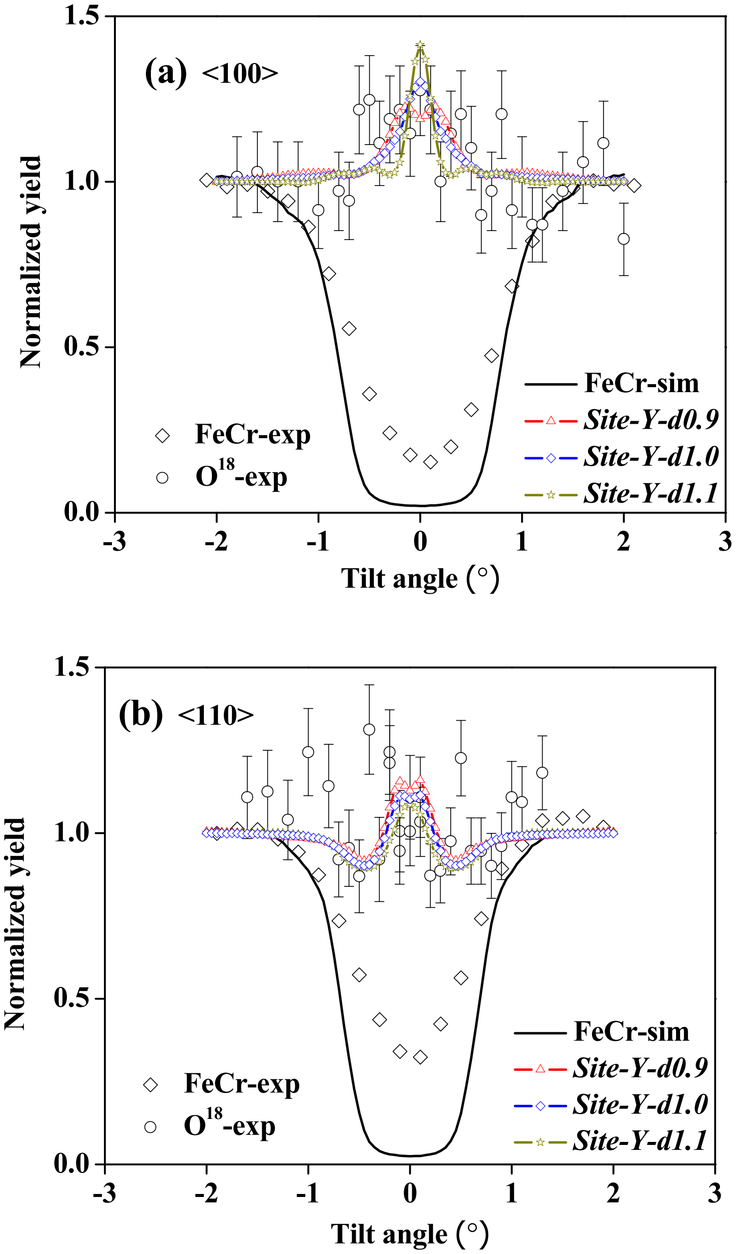

Figure 6.10 Experimental and simulated tilt angular scans of Fe+Cr and O^{18} signals along (a) <100>, (b) <110> axis of *FeCr(*O^{18}*+Fe@2*R_p*)*.

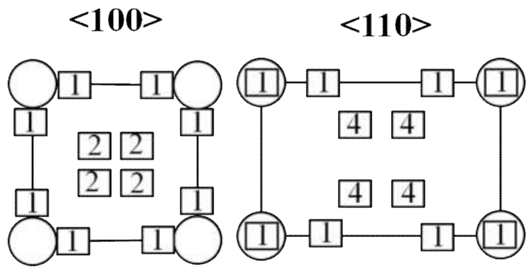

Figure 6.11 Projection of site *Y* in bcc system along <100> and <110> axis.

The experimental and simulated tilt angular scans of host and O^{18} signal obtained in *FeCr*(O^{18}+*Fe@2*R_p) are shown in Fig.6.9 (a) along <100> and Fig. 6.9 (b) along <110>. Compared to earlier O^{18} signal, a clear difference in the O^{18} signal is observed while there is no considerable change in the host signal in both <100> and <110> axes. From this, one can infer that the lattice location of O^{18} is shifted due to the introduction of vacancy and annealing. By considering the host signal, the χ_{min} of experimental scans along <100>, <110> axes is 16%, 32% respectively. The width of the experimental scans 0.79°, 0.62° are comparable with simulated values of 0.82°, 0.7° along <100>, <110> directions respectively.

For the case of O^{18} signals, the experimental scans are matching with simulation of O^{18} at site *Y* (shown in Fig. 6.7) as shown in Fig. 6.9 (a) and 6.9 (b) which is displaced along <110> from octahedral site. The projection of site *Y* is shown in Fig. 6.10. Experimental scans are fitted with simulated scans assuming different displacements and the best fit is obtained for *site-Y-d1.0* (displaced 1.0 Å from substitutional to octahedral interstitial site in other words 1.0 Å from octahedral to substitutional site along <110>) along <100>, <110> respectively. By fitting the experimental scans within error bar the lattice location of O^{18} is at *site-Y-d1.0* which is displaced 1.0±0.1 Å along <110> from octahedral interstitial site. The random fraction f_R (Eq. (2.22)) that account the dechanneling from defects in the matrix is 0.14, 0.3 for <100>, <110> axis respectively. During fitting by using Eq. (2.21), no extra random yield is added for O^{18}.

6.5. Positron annihilation spectroscopy study of vacancy defects

The SPDBS measurements are done in reference and *FeCr*(O^{18}+*Fe@2*R_p). The *S* parameter as a function of incident positron beam energy of the pristine reference sample and *FeCr*(O^{18}+*Fe@2*R_p) sample are shown in Fig. 6.11 (a). For pristine reference sample, $S(E)$

curve is analyzed and fitted with single layer model by using VEPFIT code, which shows depth resolved *S* parameter of 0.507 and diffusion length of 92 nm. The $FeCr(O^{18}+Fe@2R_p)$ sample shows good fit of depth resolved *S* parameter and effective diffusion length for two layer fitting, and is shown in Fig. 6.11 (b). The spectrum is fitted by assuming two layers, where first layer is from surface to 66 nm depth and second layer is from 66 nm to 710 nm. The *S* parameter for first layer is 0.529 which is slightly higher than the second layer value 0.522 and the diffusion lengths in first and second layers are 45 nm and 59 nm respectively. The vacancy concentration in the assumed layer is calculated using Eq. (3.1) without accounting the Cr effect.

$$Nv = \frac{\rho}{\gamma\tau^{b}}\left(\frac{L_{+,b}^{2}}{L_{+.t}^{2}} - 1\right)(cm^{-3})$$

where ρ is the atomic density (8.338×10^{22} atoms/cm^3 for pure Fe15%Cr), τ_b is the annihilation life time of positron in bulk (110 ps for defect free Fe [84] which is adopted here for FeCr also), γ is the specific positron trapping rate of mono vacancy (1×10^{15} s^{-1}) [85], and $L_{+,b}$ and $L_{+,t}$ are the effective diffusion lengths in defect free bulk and defected FeCr layer, respectively. The calculated vacancy concentration of first and second layer is 2.4×10^{18} cm^{-3} and 1.1×10^{18} cm^{-3} respectively. The effect of Cr is not accounted in calculating vacancy concentration and these values may contain errors [122]. However, the SPDBS measurements show presence of vacancy defects at O^{18} implanted depth. The *S-W* plot of ion implanted FeCr(100) is shown in Fig. 11 (c). The data points show linear fitting for reference as well as ion implanted sample which indicates same type of vacancy defects are present in the sample.

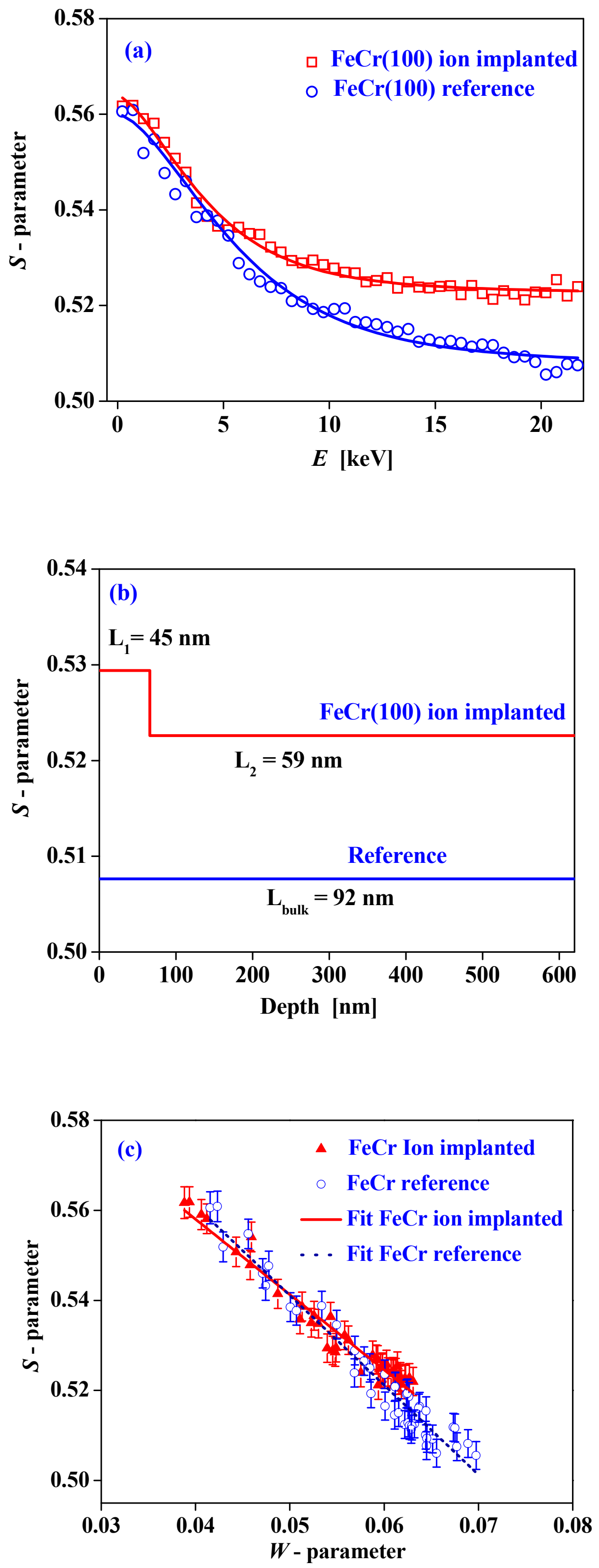

Figure 6.12 (a) The experimental and VEPFIT simulated *S* parameter as a function of positron energy, (b) Depth resolved *S* parameter and diffusion lengths and (c) *S*-*W* plot for reference FeCr(100) and $FeCr(O^{18}+Fe@2R_p)$.

6.6. DFT study of Cr interactions with vacancy defects in Fe

From the experiment, O^{18} is found to trap at site *X* which is displaced along <100> from octahedral interstitial site in ion implanted FeCr. Same site is experimentally observed for O^{18} in Fe(100) in chapter 5 and same is found by DFT for the O interaction with <100> vacancy dislocation loops. This show strong evidence of O^{18} trapping at vacancy dislocation loops in ion implanted FeCr also. To understand the effect of Cr on O-dislocation loop structure, interactions of Cr with interstitial dislocation loop structure was studied by DFT and presented in chapter 5. In this chapter, interactions of Cr with vacancy clusters are studied by using DFT calculations to understand the experimental results. The Cr interactions with vacancy clusters in the form of ½ <111> and <100> dislocation loops are studied. The considered vacancy clusters of <100> and ½ <111> loop structures are shown in Fig. 6.12. The studied Cr positions are marked from 1 to 8. The total energy calculations at constant volume (*CV*) are performed for all structures and the obtained binding energy and lattice location of Cr is given in Table 6.1. The binding energy of Cr is less than 0.1 eV in all the structures studied except *V_5-<100>-Cr(3)* configuration where binding energy of 0.15 eV is observed. The lattice location of Cr is found around substitutional sites with less than 0.1 Å displacement in all the structures except *V_5-<100>-Cr(3)* where 0.56 Å displacement is observed along <100> from substitutional site. These lattice site locations of Cr are not matching with previous experiment, where 0.15 Å displacement is observed for Cr^+ ion implanted in Fe(100) (section 5.4 of chapter 5). The binding energies of Cr with vacancy dislocation loop structures studied here are lower than that of interstitial dislocation loop structures (studied in chapter 5).

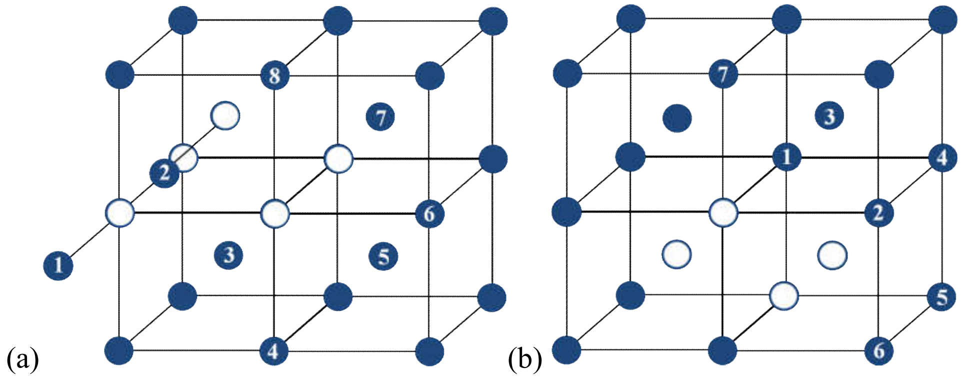

Figure 6.13 (a) Schematic of a <100> vacancy dislocation loop structure containing five vacancies. (b) Schematic of a ½ <111> vacancy dislocation loop structure containing four vacancies. Open circle, solid circle represent vacancy, Fe atom respectively. The studied Cr atom positions are marked from 1 to 8.

Table 6.1 DFT predicted binding energy of Cr with vacancy defects.

Defect structure	**Binding energy of Cr**	**Cr lattice location**
V_5-<100>-Cr(1)	-0.02 eV	Substitutional site
V_5-<100>-Cr(2)	0.07 eV	Substitutional site
V_5-<100>-Cr(3)	0.15 eV	0.56 Å displaced along <100> from substitutional site
V_5-<100>-Cr(4)	-0.02 eV	Substitutional site
V_5-<100>-Cr(5)	0.03 eV	Substitutional site
V_5-<100>-Cr(6)	-0.02 eV	Substitutional site
V_5-<100>-Cr(7)	0.07 eV	Substitutional site
V_5-<100>-Cr(8)	0.057 eV	Substitutional site
V_4-<111>-Cr(1)	0.02 eV	Substitutional site
V_4-<111>-Cr(2)	0.07 eV	Substitutional site
V_4-<111>-Cr(3)	0.03 eV	Substitutional site
V_4-<111>-Cr(4)	0.034 eV	Substitutional site
V_4-<111>-Cr(5)	0.07 eV	Substitutional site
V_4-<111>-Cr(6)	0.034 eV	Substitutional site
V_4-<111>-Cr(7)	0.006 eV	Substitutional site

The experimentally observed O^{18} lattice location in FeCr is similar to O^{18} ion implanted Fe(100) with excess vacancies (section 4.4 of chapter 4) which implies that O^{18} is trapped at <100> vacancy dislocation loops. The effect of Cr on O-defect interaction could be understood from the experimental and DFT studies. First, one can compare the O^{18} lattice location in bcc Fe(110) and FeCr(100) crystal. The O^{18} is found at tetrahedral interstitial site in O^{18} ion implanted and annealed (400 °C) Fe(110). In contrast to this the O^{18} is found atsite *X* which is displaced along <100> from octahedral interstitial site in O^{18} ion implanted and annealed (400 °C) Fe15%Cr(100) alloy. The DFT study shows that the tetrahedral site of O^{18} is should be due to segregation at interstitial dislocation loops in Fe and site *X* should be due to O^{18} trapping at vacancy dislocation loops in Fe. Also, DFT calculations predict high binding energy of O with vacancy dislocation loop (~2 eV) and low binding energy with interstitial dislocation loop (~0.2 eV). For Cr, the DFT calculations predict that Cr is more attractive to interstitial dislocation loop (binding energy 0.7 eV) than vacancy dislocation loops (binding energy ~0.15 eV). These results suggest that in presence of both vacancy and interstitial dislocation loops in FeCr alloy, the Cr atoms segregate to interstitial loops only and O atoms are trapped at vacancy loops only. In Fe crystal, oxygen is segregating either to interstitial loop or trapped at vacancy loop depending on the interstitial/vacancy dislocation loop density. The present experimental and DFT results show strong evidence of Cr segregation on interstitial dislocation loops in FeCr alloy which also restricts the O interactions with interstitial dislocation loops and favors the O interactions with vacancy loop in FeCr alloy.

6.7. Conclusion

The lattice location of O^{18} ion implanted in Fe15%Cr alloy is found to be displaced 0.6 Å from octahedral interstitial site to substitutional site by ion channeling experiments which is found to be trapped at vacancy dislocation loops. The Cr interactions with vacancy dislocation loop structures are studied by using DFT calculations. The Cr is found to be attractive towards vacancy clusters; however, the binding energy is lower than that of interstitial dislocation loops. The positron annihilation spectroscopy shows the presence of vacancy defects and the energy dependant dechanneling measurements show the presence of dislocation loop defects. This suggests that both interstitial and vacancy dislocation loops are coexisting in the FeCr alloy. However the O^{18} is trapped at vacancy defects in FeCr alloy which is in contrast to the O^{18} implanted in Fe where it segregates to interstitial dislocation loops (both the experimental and annealing conditions are same). The Cr solute strongly affects the O-defect structures. The Cr segregates to interstitial dislocation loops and restricts the O interactions with interstitial dislocation loops as well as promotes the O interactions with vacancy defects.

Chapter 7

Summary and scope of the future work

7.1. Summary

The interactions of solute atoms with vacancy and interstitial clusters is an important factor affecting the microstructural changes in the structural materials used in high radiation environement. The FeCr alloys with 9-15 atomic percentage is reported to be suitable matrix for nuclear sructural materials due to its high voids welling resistance. These are also used as matrix for ODS alloys. However, the effect of Cr on the defect interactions is not well understood. In order to understand the interactions of O and Cr with interstitial and vacancy defects in Fe and FeCr model system, the Cr and O^{18} solutes along with defects are introduced in Fe and FeCr single crystals by ion implantation technique. For introducing excess interstitials, self ions are implanted at R_p of O^{18} ions. For introducing excess vacancy defects, $R_p/2$ effect is used by implanting self ions at twice the range of O^{18} ions. The range and type of defects are characterized by RBS channeling experiments. The lattice location of ion implanted O^{18} is studied by $O^{18}(p,\alpha)N^{15}$ NRA/channeling and Cr is studied by PIXE/channeling techniques. The vacancy concentraion at O^{18} ion implanted depth was studied by SPDBS technique. In order to find the O-defect and Cr-defect structures formed in ion implanted crystls, the Cr and O interactions with small vacancy and interstitial clusters as well as dislocation loop structures in bcc Fe system are studied by using DFT calculations. All the experimental and DFT resuls reported in this thesis are presented in Table 7.1 and Table 7.2 for comparison. The energy dependent dechannenneling parameter study confirms the presence of dislocation loops and SPDBS study confirms the presence of vacancy defects. Both of these studies give proof for the presence of both interstitial and vacancy dislocation loops in the samples as reported in reference [33].

Table 7.1 Summary of experimental and DFT results is shown here. The dislocation loop density given is for <100> loops. All samples are *in-situ* annealed at 400 °C for 30 mins.

Sample	**Sample condition**	**Oxygen trapping**	**<100> Dislocation loop density**	**Vacancy concentr-ation**	**Defect configuration predicted by DFT to match experimental result**
Fe1(O^{18})	300 keV O^{18} (5×10^{15} ions/cm^2)	Tetrahedral	-	-	Displaced 0.37 Å towards octahedral from tetrahedral for O interaction with interstitial dislocation loop
Fe1(O^{18}+Fe@R_p)	5×10^{15} ions/cm^2 (300 keV O^{18}) + 1×10^{16} ions/cm^2 (750 keV Fe)	Displaced tetrahedral (0.2 Å towards octahedral from tetrahedral)	2.8×10^{10}/cm^2	2.15×10^{17} cm^{-3}	Displaced 0.37 Å towards octahedral from tetrahedral for O interaction with interstitial dislocation loop
Fe2(O^{18}+1Fe@2R_p)	5×10^{15} ions/cm^2 (300 keV O^{18}) + 1×10^{16} ions/cm^2 (1550 keV Fe)	Displaced 1.1 Å along <111> from substitutional site	-	-	Displaced 1.1 Å along <111> from substitutional site for O interaction with ½ <111> vacancy dislocation loop
Fe2(O^{18}+2Fe@2R_p)	5×10^{15} ions/cm^2 (300 keV O^{18}) + 2×10^{16} ions/cm^2 (1550 keV Fe)	Displaced 0.6 Å along <100> from octahedral	6.9×10^{10}/cm^2	6.74×10^{17} cm^{-3}	Displaced 0.46 Å along <100> from substitutional site for O interaction with <100> vacancy dislocation loop
Fe3(O^{18}+Cr@R_p)	1×10^{16} ions/cm^2 (300 keV O^{18}) + 1×10^{16} ions/cm^2 (750 keV Cr)	Tetrahedral	4.6×10^{10}/cm^2	1.2×10^{18} cm^{-3}	Displaced 0.37 Å towards octahedral from tetrahedral for O interaction with interstitial dislocation loop
FeCr(O^{18})	300 keV O^{18} (5×10^{15} ions/cm^2)	Displaced 0.6 Å along <100> from octahedral	-	-	Displaced 0.46 Å along <100> from substitutional site for O interaction with <100> vacancy dislocation loop
FeCr(O^{18}+Fe@2R_p)	5×10^{15} ions/cm^2 (300 keV O^{18}) + 1×10^{16} ions/cm^2 (1550 keV Fe)	Displaced 1.0 Å along <110> from octahedral	3.7×10^{10}/cm^2	1.1×10^{18} cm^{-3}	-

In O^{18} and self ion implanted and annealed Fe(110), the O^{18} is observed around tetrahedral interstitial site. The DFT predicts that this observed site of O^{18} is due to trapping at interstitial dislocation loops. This is the first report of observation of O^{18} at tetrahedral interstitial site in bcc Fe.

In another sample where excess vacancy defects are introduced intensionally at O^{18} depth by self ion implantation, O^{18} is found to displaced along <111> direction from substitutional site and it is found to be displaced along <100> from octahedral interstitial site upon increasing concentration. The DFT calculations predict that the observed O^{18} sites are due to trapping at vacancy dislocation loops. From this, it is concluded that the O is attractive towards both interstitial and vacancy dislocation loops.

When Cr and O^{18} ions are implanted at same depth of Fe(100), O^{18} is found around tetrahedral interstitial site which implies that here also O^{18} is trapped at interstitial dislocation loops. The Cr is found to be slighly displaced from substitutional site and DFT predicts that Cr could strongly bind similar sites in presence of interstitial dislocation loops and Cr binds weakly with vacancy dislocation loops. In this study Cr concentration is low and it is found to be trapped at interstitial dislocation loop.

Table 7.2 The DFT predicted solute interaction strength with defects in Fe.

Solute	**Defect**	**Binding energy (eV)**
O	Interstitial dislocation loop	0.24
O	Vacancy dislocation loop	2.0
Cr	Interstitial dislocation loop	0.7
Cr	Vacancy dislocation loop	<0.1

In contrast to O^{18} ion implanted bcc Fe, O^{18} is found to be displaced along <100> from octahedral interstitial site in Fe15%Cr(100) alloy which is due to trapping at vacancy dislocation loops. For comparison, the DFT calculated binding energies of solutes with defects are shown in Table 7.2. It is clearly seen the O binds strongly with vacancy dislocation loops and moderately with interstitial dislocation loops. The Cr binds strongly with interstitial dislocation loops and weekly with vacancy dislocation loops. In O^{18} ion implanted Fe15%Cr alloy interstitial defect could be more dominant at O^{18} depth. However, the observation shows that O^{18} is trapped at vacancy dislocation loop which is due to the effect of Cr solute. The Cr could be segregated to interstitial dislocation loops due to its strong interaction which blocks the O interactions with interstitial dislocation loops. The O diffuses in the matrix and is trapped at vacancy defects. This thesis provides a strong evidence of competing interactions between defects and solutes in Fe and FeCr and their strong influence on the defect evolution under radiation damage.

7.2. Future directions

Oxygen and carbon are the important interstitial solutes in bcc systems. Understanding the C interactions with defect is also important which influences the microstructure as well as properties of ferritic steels. The MD simulations already predicted that the C controls radiation damage recovery in bcc based materials [39]. Experimental study of defect structure in C^+ ion implanted and annealed bcc Fe can help to understand C influence on defect evolution.

All DFT and MD computational tools predict <110> dumbbell defect is the most stable mono interstitial structure and Cr mixed <110> dumbbell is predicted as most stable in iron-chromium alloy [37]. All the radiation damage models rely on this <110> dumbbell model. However no clear experimental evidence is shown to support this model. Experimental studies of these interstitial defects are very difficult due to its high mobility and clustering tendency. Based on these, the following future directions of the defect studies are in planning.

- Lattice location measurements of C in presence of excess self interstitial and vacancy defects and DFT study of C interactions with interstitial and vacancy dislocation loops and its lattice location in the stable defect configuration.
- Lattice location measurements of C in the presence of excess self interstitial and vacancy defects in iron-chromium alloy.
- Finding the defect structure of <110> Cr mixed dumbbell in bcc FeCr by ion channeling experiments.

Staking fault tetrahedral (SFT) is a vacancy defect observed in fcc systems. The SFT is observed during radiation damage of fcc systems like multi elemental high entropy alloy (FeNiCrCu) which is one of proposed structural materials for nuclear reactors [123]. However solute-SFT interactions are not well understood yet. To understand that one can do lattice location measurements of C and O in the presence of SFT in fcc Ni and Cu system.

References

[1] Qing Peng, Fanjiang Meng, Yizhong Yang, Chenyang Lu, Huiqiu Deng, Lumin Wang, Suvranu De & Fei Gao. Shockwave generates < 100 > dislocation loops in bcc iron. Nat. Commun. 9 (2018) 4880.

[2] Z. Lv, J. Fan, K. Guan, Z. Wu, D. Zhao, W. Fu. Effects of interstitial atoms (N/O) in bcc Fe from first-principle calculations. Fusion Eng. Des. 137 (2018) 22-29.

[3] X. Wang, M. Posselt, and J. Faßbender. Influence of substitutional atoms on the diffusion of oxygen in dilute iron alloys. Phys. Rev. B 98 (2018) 064103.

[4] A. V. Ponomareva, A. V. Ruban, B. O. Mukhamedov, I. A. Abrikosov. Effect of multicomponent alloying with Ni, Mn and Mo on phase stability of bcc Fe-Cr alloys. Acta Mater. 150 (2018) 117-129.

[5] Yaxuan Zhang, Daniel Schwen, Xian-Ming Bai. Effect of solute-SIA binding energy on defect production behaviours in Fe-based alloys. J. Nucl. Mater. 509 (2018) 124-133.

[6] Shipeng Shu, Nathan Almirall, Peter B. Wells, TakuyaYamamoto, G. Robert Odette, Dane D. Morgan. Precipitation in Fe-Cu and Fe-Cu-Mn model alloys under irradiation: Dose rate effects. Acta Mater. 157 (2018) 72-82.

[7] D. J. M. King, S. C. Middleburgh, P. A. Burr, T. M. Whiting, P. C. Fossati, and M. R. Wenman. Density functional theory study of the magnetic moment of solute Mn in bcc Fe. Phys. Rev. B 98 (2018) 024418.

[8] Dominik Gölden, Hongbin Zhang, Iliya Radulov, Imants Dirba, Philipp Komissinskiy, Erwin Hildebrandt, and Lambert Alff, Evolution of anisotropy in bcc Fe distorted by interstitial boron. Phys. Rev. B 97 (2018) 014411.

[9] L.K. Mansur. Theory and experimental background on dimensional changes in irradiated alloys. J. Nucl. Mater. 216 (1994) 97-123.

[10] A.A.F. Tavassoli. Present limits and improvements of structural materials for fusion reactors – a review. J. Nucl. Mater. 302 (2002) 73-88.

[11] C.J. Ortiz, M.J. Caturla, C.C. Fu, and F. Willaime. Influence of carbon on the kinetics of He migration and clustering in α-Fe from first principles. Phys. Rev. B 83 (2011) 139905.

[12] H. Amara, C.C. Fu, F. Soisson, and P. Maugis. Aluminum and vacancies in α-iron: Dissolution, diffusion, and clustering. Phys. Rev. B 81 (2010) 174101.

[13] S. L. Dudarev. Density Functional Theory Models for Radiation Damage. Annu. Rev. Mater. Res. 43 (2013) 35-61 (2013).

[14] Y.de. Carlan, J.L. Bechade, P. Dubuisson, J.L. Seran, P. Billot, A. Bougault, T. Cozzika, S. Doriot, D. Hamon, J. Henry, M. Ratti, N. Lochet, D. Nunes, P. Olier, T. Leblond, M. H. Mathon. CEA developments of new ferritic ODS alloys for nuclear applications. J. Nucl. Mater. 386–388 (2009) 430-432.

[15] G.S. Was, Fundamentals of radiation materials science (Springer, New York, 2007).

[16] B.C. Masters. Dislocation loops in irradiated iron. Philos. Mag. 11 (1964) 881-893.

[17] B.L. Eyre, A.F. Bartlett. An electron microscope study of neutron irradiation damage in alpha-iron. Philos. Mag. 12 (1965) 261-272.

[18] S.L. Dudarev, K. Arakawa, X. Yia, Z. Yao, M.L. Jenkins, M.R. Gilbert, P.M. Derlet. Spatial ordering of nano-dislocation loops in ion-irradiated materials. J. Nucl. Mater. 455 (2014) 16-20.

[19] J.J. Laidler, B. Mastel. Nucleation of Voids in Irradiated Stainless Steel. Nature 239 (1972) 97–98.

[20] V.I. Pastukhov, S.A. Averin, V.L. Panchenko, I.A. Portnykh, P.D. Freyer, L.A. Giannuzzi, F.A. Garnerc. Application of backscatter electrons for large area imaging of cavities produced by neutron irradiation. J. Nucl. Mater. 480 (2016) 289-300.

[21] C.C. Fu and F. Willaime. Stability and Mobility of Mono-and Di-Interstitials in α-Fe. Phys. Rev. Lett. 92 (2004) 175503.

[22] A. Terentyev, T.P.C. Klaver, P. Olsson, M.C. Marinica, F. Willaime, C. Domain, and L. Malerba. Self-Trapped Interstitial-Type Defects in Iron. Phys. Rev. Lett. 100 (2008) 145503.

[23] L. Dézerald, M.C. Marinica, L. Ventelon, D. Rodney, F. Willaime. Stability of self-interstitial clusters with C15 Laves phase structure in iron. J. Nucl. Mater. 449 (2014) 219-224.

[24] M.C. Marinica, F. Willaime, and J.P. Crocombette. Irradiation-Induced Formation of Nanocrystallites with C15 Laves Phase Structure in bcc Iron. Phys. Rev. Lett. 108 (2012) 025501.

[25] M.Yu. Lavrentiev, D. Nguyen-Manh, S.L. Dudarev. Chromium-vacancy clusters in dilute bcc Fe-Cr alloys: An ab initio study. J. Nucl. Mater. 499 (2018) 613-621.

[26] B.D. Wirth. How Does Radiation Damage Materials? Science 318 (2007) 923-924.

[27] N. Gao, J. Chen, R. J. Kurtz, Z. G. Wang, R. F. Zhang and F. Gao. New understanding of nano-scale interstitial dislocation loops in BCC iron. J. Phys.: Condens. Matter 29 (2017) 455301.

[28] B.C. Masters. Dislocation Loops in Irradiated Iron. Nature 200 (1963) 254.

[29] C.A. English, B.L. Eyre, M.L. Jenkins. Heavy-ion damage in α Fe. Nature 263 (1976) 400–401.

[30] C.C. Fu, J.D. Torre, F. Willaime, J.L. Bocquet, A. Barbu. Multiscale modelling of defect kinetics in irradiated iron. Nat. Mater. 4 (2005) 68–74.

[31] Takaki S., Fuss J., Kugler H., Dedek U., Schultz H. The resistivity recovery of high purity and carbon doped iron following low temperature electron irradiation. Radia. Eff. Defects Solids 79 (1983) 87–122.

[32] Z. Yao, M.L. Jenkins, M. Hernández-Mayoral and M.A. Kirk. The temperature dependence of heavy-ion damage in iron: A microstructural transition at elevated temperatures. Philos. Mag. 90 (2010) 4623-4634.

[33] F. Wan, Q. Zhan, Y. Long, S. Yang, G. Zhang, Y. Du, Z. Jiao, S. Ohnuki. The behavior of vacancy-type dislocation loops under electron irradiation in iron. J. Nucl. Mater. 455 (2014) 253-257.

[34] M. Hernández-Mayoral, Z. Yao, M.L. Jenkins and M.A. Kirk. Heavy-ion irradiations of Fe and Fe–Cr model alloys Part 2: Damage evolution in thin-foils at higher doses. Philos. Mag. 88 (2008) 2881-2897.

[35] K. Arakawa, T. Amino, H. Mori. Direct observation of the coalescence process between nanoscale dislocation loops with different Burgers vectors. Acta Mater. 59 (2011) 141-145.

[36] J. Marian, B.D. Wirth, and J.M. Perlado. Mechanism of Formation and Growth of <100> Interstitial Loops in Ferritic Materials. Phys. Rev. Lett. 88 (2002) 255507.

[37] C.S. Becquart, C. Domain. Solute–point defect interactions in bcc systems: Focus on first principles modelling in W and RPV steels. Curr. Opin. Solid State Mater. Sci. 16 (2012) 115-125.

[38] P. Olsson, T. P. C. Klaver, and C. Domain. Ab initio study of solute transition-metal interactions with point defects in bcc Fe. Phys. Rev. B 81 (2010) 054102.

[39] N. Anento, A. Serra. Carbon-vacancy complexes as traps for self-interstitial clusters in Fe-C alloys. J. Nucl. Mater. 440 (2013) 236-242.

[40] N. Gao, H. Van Swygenhoven, M. Victoria, and J. Chen. Formation of dislocation loops during He clustering in bcc Fe. J. Phys.: Condens. Matter 23 (2011) 442201.

[41] D. Terentyev, F. Bergner, Y. Osetsky. Cr segregation on dislocation loops enhances hardening in ferritic Fe-Cr alloys. Acta Mater. 61 (2013) 1444-1453.

[42] Chenwei He. Experimental study of the interaction of vacancy defects with Y, O and Ti solutes to better understand their roles in the nanoparticles formation in ODS steels. Materials. Universite d'Orleans (2014). English. <NNT: 2014ORLE2057>. <tel-01207172>. <https://tel.archives-ouvertes.fr/tel-01207172/document>.

[43] R. Idczaka, R. Konieczny, and J. Chojcan. A study of defects in iron-based binary alloys by the Mössbauer and positron annihilation spectroscopies. J. Appl. Phys. 115 (2014) 103513.

[44] X. Hu, D. Xu, B.D. Wirth. Quantifying He-point defect interactions in Fe through coordinated experimental and modeling studies of He-ion implanted single-crystal Fe. J. Nucl. Mater. 442 (2013) S649-S654.

[45] A. Benkaddour, C. Dimitrov, O. Dimitrov. Irradiation-Induced Defects in Ferritic FeCr Alloys. Mater. Sci. Forum. 15-18 (1987) 1263-1268.

[46] G. Apostolopoulos, V. Lukianova, Z. Kotsina, A. Lagoyannis, K. Mergia, S. Harissopoulos, S. Messoloras. The influence of carbon on the resistivity recovery of proton irradiated Fe–11 at.% Cr alloys. Nucl. Mater. Energy 9 (2016) 465-470.

[47] M.M. Kijek, D.W. Palmer. Trapping of Interstitials and Vacancies at Solute Molybdenum Atoms in Iron/(0.3 at % Mo)Studied by the Ion-Channelling/Lattice-Location Technique. Mater. Sci. Forum 15-18 (1987) 703-708.

[48] S.M. Myers, S.T. Picraux, R.E. Stoltz. Defect trapping of ion-implanted deuterium in Fe. J. Appl. Phys. 50 (1979) 5710.

[49] Daniel Brimbal, Brigitte Décamps, Jean Henry, Estelle Meslin, Alain Barbu. Single- and dual-beam in situ irradiations of high-purity iron in a transmission electron microscope: Effects of heavy ion irradiation and helium injection. Acta Mater. 64 (2014) 391-401.

[50] K. Arakawa, K. Ono, M. Isshiki, K. Mimura, M. Uchikoshi, H. Mori. Observation of the One-Dimensional Diffusion of Nanometer-Sized Dislocation Loops. Science 318 (2007) 956-959.

[51] C.L. Fu, M. Krčmar, G.S. Painter, and X.Q. Chen. Vacancy Mechanism of High Oxygen Solubility and Nucleation of Stable Oxygen-Enriched Clusters in Fe. Phys. Rev. Lett. 99 (2007) 225502.

[52] L.C. Feldman, J.W. Mayer, S.T. Picraux, Materials Analysis by Ion Channeling. Academic Press, New York (1982).

[53] M. Nastasi and J. W. Mayer, Ion Implantation and Synthesis of Materials. Springer-Verlag, Berlin (2006).

[54] Z.F. Ziegler, J.P. Biersack, U. Littmark, Stopping and Range of Ions in Solids. Pergamon Press, New York (1985).

[55] Wei-Kan Chu, James W. Mayer, and Marc-A. Nicolet, Backscattering Spectrometry. Academic Press (1978).

[56] Leonard C. Feldman, James W. Mayer. Fundamentals of surface and thin film analysis. North-Holland (1986).

[57] RBS lab, https://sites.google.com/a/lbl.gov/rbs-lab/ion-beam-analysis.

[58] Georges. Amsel, and David. Samuel. Microanalysis of the stable isotopes of oxygen by means of nuclear reactions. Anal. Chem. 39 (14) (1967) 1689–1698.

[59] André Vantomme. 50 years of ion channeling in materials science. Nucl. Instr. Meth. B 371 (2016) 12-26.

[60] M. Motapothula, Z.Y. Dang, T. Venkatesan, M.B.H. Breese. A study of ion channeling patterns at minor axes in silicon. Nucl. Instr. Meth. B 330 (2014) 24-32.

[61] K. Suresh, B. Sundaravel, B.K. Panigrahi, K.G.M. Nair, and B. Viswanathan. Virtual instrument automation of ion channeling setup for 1.7 MV tandetron accelerator. Rev. Sci. Instrum 75 (2004) 4891.

[62] Hiroshi Kudo. Energy dependence of dechanneling by a dislocation loop. Phys. Rev. B, 18 (1978) 5995.

[63] Flux, http://www.pjms.nl/flux.html

[64] P.J.M. Smulders and D.O. Boerma. Computer simulation of channeling in single crystals. Nucl. Instr. Meth. B 29 (1987) 471.

[65] R.B. Alexander, P.T. Callaghan, and J.M. Poate. Use of the channeling technique and calculated angular distributions to locate Br implanted into Fe single crystals. Phys. Rev. B 9 (1974) 3022.

[66] Krause-Rehberg R and Leipner H S 1999 "Positron Annihilation in Semiconductors: Defect Studies" (Springer series in solid-state sciences) 127 ed Manuel Cardona et al (Berlin: Springer).

[67] Vinita J. Ghosh and G.C. Aers. Positron stopping in elemental systems: Monte Carlo calculations and scaling properties. Phys. Rev. B 51 (1995) 45.

[68] The Slow-Positron System of Rossendorf. https://www.hzdr.de/db/Cms?pOid=35320&pNid=0

[69] D.A. Fischer, K.G. Lynn, and D.W. Gidley. High-resolution angle-resolved positron reemission spectra from metal surfaces. Phys. Rev. B 33 (1986) 4479.

[70] K. F. Canter, A. P. Mills Jr. Slow positron beam design notes. Can. J. Phys. 60 (1982) 551-557.

[71] Knoll G F 2000 "Radiation detection and measurement"3rd edition (New York : John Wiley and Sons).

[72] A. van Veen, H. Schut, J. de Vries, R. A. Hakvoort, and M. R. Ijpma. Analysis of positron profiling data by means of ''VEPFIT''. AIP Conf. Proc. 218 (1990) 171.

[73] R. Dreizler, E. Gross, Density Functional Theory. (Plenum Press, New York, 1995).

[74] W. Koch, M. C. Holthausen, A Chemist's Guide to Density Functional Theory. (Wiley-VCH, Weinheim, ed. 2, 2002).

[75] R. G. Parr, W. Yang, Density-Functional Theory of Atoms and Molecules. (Oxford University Press, New York, 1989).

[76] P. Hohenberg and W. Kohn. Inhomogeneous Electron Gas. Phys. Rev. 136 (1964) B864.

[77] W. Kohn and L. J. Sham. Self-Consistent Equations Including Exchange and Correlation Effects. Phys. Rev. 140 (1965) A1133.

[78] G. Kresse, J. Furthmuller. Efficient iterative schemes for ab initio total-energy calculations using a plane-wave basis set. Phys. Rev. B, 54 (1996) 11169.

[79] P.E. Bloch. Projector augmented-wave method. Phys. Rev. B 50 (1994) 17953.

[80] H.J. Monkhorst, J.D. Pack. Special points for Brillouin-zone integrations. Phys. Rev. B 13 (1976) 5897.

[81] W.A. Counts, C. Wolvertona, R. Gibala. First-principles energetics of hydrogen traps in α-Fe: Point defects. Acta Mater, 58 (2010) 4730-4741.

[82] https://indico.ph.ed.ac.uk/event/2/session/2/contribution/12/material/slides/0.pdf.

[83] J. Čižek, I. Procházka, G. Brauer, W. Anwand, R. Gemma, E. Nikitin, R. Kirchheim and A. Pundt. Hydrogen Interaction with Vacancies in Electron Irradiated Niobium. Acta Phys. Pol. A, 133 (2008) 1293-1299.

[84] P. Hautojärvi, L. Pöllänen, A. Vehanen, J. Yli-Kauppila. Vacancies and carbon impurities in α-iron: Neutron irradiation. J. Nucl. Mater. 114 (1983) 250-259.

[85] A. Vehanen, P. Hautojärvi, J. Johansson, J. Yli-Kauppila, and P. Moser. Vacancies and carbon impurities in α-iron: Electron irradiation. Phys Rev B 25 (1982) 762.

[86] M.J. Aliaga, R. Schäublin, J.F. Löffler, M.J. Caturla. Surface-induced vacancy loops and damage dispersion in irradiated Fe thin films. Acta Mater. 101 (2015) 22-30.

[87] Pär Olsson, Christophe Domain, and Janne Wallenius, Ab initio study of Cr interactions with point defects in bcc Fe, Phys. Rev. B 75 (2007) 014110.

[88] R. Alexander, M.C. Marinica, L. Proville, F. Willaime, K. Arakawa, M.R. Gilbert, S.L. Dudarev. Ab initio scaling laws for the formation energy of nanosized interstitial defect clusters in iron, tungsten, and vanadium. Phys. Rev. B, 94 (2016) 024103.

[89] A. Hirata, T. Fujita, Y. R. Wen, J. H. Schneibel, C. T. Liu & M. W. Chen. Atomic structure of nanoclusters in oxide-dispersion-strengthened steels. Nat. Mater. 10 (2011) 922–926.

[90] C. David, B. Sundaravel, T.R. Ravindran, K.G.M. Nair, B.K. Panigrahi, H.P. Lenka, B. Joseph, D.P. Mahapatra. Observation of an enhanced gettering effect in silicon under germanium molecular ion implantation. Appl. Phys. A, 88 (2007) 397-400.

[91] P.M. Derlet, D. Nguyen-Manh, S.L. Dudarev. Multiscale modeling of crowdion and vacancy defects in body-centered-cubic transition metals. Phys. Rev. B 76 (2007) 054107.

[92] A. Bhattacharya, E. Meslin, J. Henry, A. Barbu, S. Poissonnet, B. Décamps. Effect of chromium on void swelling in ion irradiated high purity Fe–Cr alloys. Acta Mater. 108 (2016) 241-251.

[93] V. Kuksenko, C. Pareige, P. Pareige. Intra granular precipitation and grain boundary segregation under neutron irradiation in a low purity Fe–Cr based alloy. J. Nucl. Mater. 425 (2012) 125-129.

[94] A. Bhattacharya, E. Meslin, J. Henry, C. Pareige, B. Décamps, C. Genevois, D. Brimbal, A. Barbua. Chromium enrichment on the habit plane of dislocation loops in ion-irradiated high-purity Fe–Cr alloys. Acta Mater. 78 (2014) 394-403.

[95] D. Terentyev, F. Bergner, Y.Osetsky. Cr segregation on dislocation loops enhances hardening in ferritic Fe–Cr alloys. Acta Mater. 61 (2013) 1444-1453.

[96] D. Terentyev, I. Martin-Bragado. Evolution of dislocation loops in iron under irradiation: The impact of carbon. Scripta Mater. 97 (2015) 5-8.

[97] H. Paul, J. Sacher, Fitted empirical reference cross sections for K-shell ionization by protons, Atom. Data Nucl. Data 42 (1989) 105-l 56.

[98] T. P. C. Klaver, P. Olsson, and M. W. Finnis, Interstitials in FeCr alloys studied by density functional theory, Phys. Rev. B 76 (2007) 214110.

[99] Erin Hayward and Chu-Chun Fu. Interplay between hydrogen and vacancies in α-Fe. Phys. Rev. B 87 (2013) 174103.

[100] Z. Yao, M. Hernández-Mayoral, M.L. Jenkins and M.A. Kirk, Heavy-ion irradiations of Fe and Fe–Cr model alloys Part 1: Damage evolution in thin-foils at lower doses. Philos. Mag. 88 (2008) 2851-2880.

[101] J. Wallenius, P. Olsson, C. Lagerstedt, N. Sandberg, R. Chakarova, and V. Pontikis. Modeling of chromium precipitation in Fe-Cr alloys. Phys. Rev. B 69 (2004) 094103.

[102] A. L. Nikolaev, Stage I of recovery in 5 MeV electron-irradiated iron and iron-chromium alloys: the effect of small cascades, migration of di-interstitials and mixed dumbbells, J. Phys.: Condens. Mat. 11 (1999) 8633-8644.

[103] Frédéric Soisson, Estelle Meslin, Olivier Tissot. Atomistic modeling of α' precipitation in Fe-Cr alloys under charged particles and neutron irradiations: Effects of ballistic mixing and sink densities. J. Nucl. Mater. 508 (2018) 583-594.

[104] Wei-Ying Chen, Yinbin Miao, Jian Gan, Maria A. Okuniewski, Stuart A. Maloy, James F. Stubbins. Neutron irradiation effects in Fe and Fe-Cr at 300 °C. Acta Mater. 111 (2016) 407-416.

[105] N. Castin, L. Messina, C. Domain, R. C. Pasianot, and P. Olsson. Improved atomistic Monte Carlo models based on ab-initio-trained neural networks: Application to FeCu and FeCr alloys. Phys. Rev. B 95 (2017) 214117.

[106] Xin Xu, Joakim Odqvist, Magnus Hörnqvist Colliander, Stephen King, Mattias Thuvander, Axel Steuwer, Peter Hedström. Effect of cooling rate after solution treatment on subsequent phase separation during aging of Fe-Cr alloys: A small-angle neutron scattering study. Acta Mater. 134 (2017) 221-229.

[107] Kevin G. Field, Samuel A. Briggs, Kumar Sridharan, Yukinori Yamamoto, Richard H. Howard. Dislocation loop formation in model FeCrAl alloys after neutron irradiation below 1 dpa. J. Nucl. Mater. 495 (2017) 20-26.

[108] Caleb P. Massey, Sebastien N. Dryepondt, Philip D. Edmondson, Kurt A. Terrani, Steven J. Zinkle. Influence of mechanical alloying and extrusion conditions on the microstructure and tensile properties of Low-Cr ODS FeCrAl alloys. J. Nucl. Mater. 512 (2018) 227-238.

[109] Samuel A. Briggs, Philip D. Edmondson, Kenneth C. Littrell, Yukinori Yamamoto, Richard H. Howard, Charles R. Daily, Kurt A. Terrani, Kumar Sridharan, Kevin G. Field. A combined APT and SANS investigation of α′ phase precipitation in neutron-irradiated model FeCrAl alloys. Acta Mater. 129 (2017) 217-228.

[110] R. Schäublin, B. Décamps, A. Prokhodtseva, J.F. Löffler. On the origin of primary ½ a_0 <111> and a_0 <100> loops in irradiated Fe(Cr) alloys. Acta Mater. 133 (2017) 427-439.

[111] Kevin G. Field, Samuel A. Briggs, Kumar Sridharan, Richard H. Howard, Yukinori Yamamoto. Mechanical properties of neutron-irradiated model and commercial FeCrAl alloys. J. Nucl. Mater. 489 (2017) 118-128.

[112] Kevin G. Field, Kenneth C. Littrell, Samuel A. Briggs. Precipitation of α′ in neutron irradiated commercial FeCrAl alloys. Scr. Mater. 142 (2018) 41-45.

[113] Jack C. Haley, Samuel A. Briggs, Philip D. Edmondson, Kumar Sridharan, Steve G. Roberts, Sergio Lozano-Perez, Kevin G. Field. Dislocation loop evolution during in-situ ion irradiation of model FeCrAl alloys. Acta Mater. 136 (2017) 390-401.

[114] W.T. Geng, Q. Zhan. Nanometer-thick films produced in H irradiated Fe-Cr alloy. Scr. Mater. 147 (2018) 55-58.

[115] O. Tissot, C. Pareige, E. Meslin, B. Décamps & J. Henry. Influence of injected interstitials on α′ precipitation in Fe–Cr alloys under self-ion irradiation. Mater. Res. Lett. 5 (2017) 117-123.

[116] J. Chen, F. Duval, P. Jung, R. Schäublin, N. Gao, M.F. Barthe. Dislocation loops in ultra-high purity Fe(Cr) alloys after 7.2 MeV proton irradiation. J. Nucl. Mater. 503 (2018) 81-90.

[117] A. Takahashi, T. Suzuki, A. Nomoto, T. Kumagai. Influence of spinodal decomposition structures on the strength of Fe-Cr alloys: A dislocation dynamics study. Acta Mater. 146 (2018) 160-170.

[118] Kleyton J. Camelo, Francisco C. Oliveira Junior, Manoel R. da Silva and Igor F. Vasconcelos. Influence of precipitates on the magnetic properties of Fe–Cr–Mo alloys studied by X-ray diffraction, Mössbauer spectroscopy and vibrating sample magnetometry. J. Mater. Res. 32 (2017) 1316-1323.

[119] Dafit Feriyanto, M.I. Idris, Darwin Sebayang. Effect of Cr to Fe on the Solid Solubility, Lattice Parameter and Strain of $Fe_{80}Cr_{20}$ Alloy Powder. Appl. Mech. Mater. 660 (2014) 280-284.

[120] F. Bergner, A. Ulbricht, C. Heintze. Estimation of the solubility limit of Cr in Fe at 300°C from small-angle neutron scattering in neutron-irradiated Fe–Cr alloys. Scr. Mater. 61 (2009) 1060-1063.

[121] Panagiotis Grammatikopoulos & Kai Nordlund. Molecular dynamics simulation of Cr-precipitate demixing in FeCr alloys. Radiat. Eff. Defect S. 169 (2014) 646-654 .

[122] M. Lambrecht, L. Malerba. Positron annihilation spectroscopy on binary Fe-Cr alloys and ferritic/martensitic steels after neutron irradiation. Acta Mater. 59 (2011) 6547–6555.

[123] Chenyang Lu, Ke Jin, Laurent K. Béland, Feifei Zhang, Taini Yang, Liang Qiao, Yanwen Zhang, Hongbin Bei, Hans M. Christen, Roger E. Stoller & Lumin Wang. Direct Observation of Defect Range and Evolution in Ion-Irradiated Single Crystalline Ni and Ni Binary Alloys. Sci. Rep. 6 (2016) 19994.